

DISSERTATION

On a new form of marginal separation in dense gases

ausgeführt zum Zwecke der Erlangung des akademischen Grades eines
Doktors der technischen Wissenschaften unter der Leitung von

o.Univ.Prof. Dipl.-Ing. Dr.techn. Alfred Kluwick
E322
am Institut für Strömungslehre und Wärmeübertragung

eingereicht an der Technischen Universität Wien
Fakultät für Maschinenbau

von

Dipl.-Ing. Mats Kinell
Matr.-Nr.: 0027114
Oskar-Jascha-Gasse 34
1130 Wien

Wien, im April 2004

Diese Dissertation haben begutachtet:

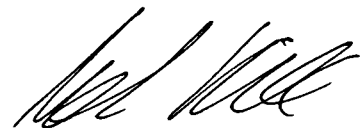

.....

Vorwort

Die vorliegende Arbeit entstand während meiner Tätigkeit als wissenschaftlicher Mitarbeiter am Institut für Strömungslehre und Wärmeübertragung, TU Wien.

Für die gute Zusammenarbeit möchte ich mich bei meinem Doktorvater o. Prof. Dr. Alfred Kluwick, dem Koreferenten ao. Prof. Dr. Herbert Steinrück und allen Institutsmitgliedern bedanken.

Wien, April 2004

A handwritten signature in black ink, consisting of several fluid, connected strokes, likely representing the name Mats Kinell.

Mats Kinell

Preface

New and unconventional features concerning the behaviour of materials are of essential importance in the development of engineering sciences. An example of this are Bethe-Zel'dovich-Thompson (BZT) fluids which have experienced a rapidly growing attention and interest in the last thirty years. As shown by Bethe [3] and Zel'dovich [34] using the van der Waals gas model, there are fluids which have a region in the general neighbourhood of the thermodynamic critical point where the so called fundamental derivative, describing the curvature of an isentrop in the pv -diagram, becomes negative provided that the specific heats are large enough. In contrast, the fundamental derivative for perfect gases is always larger than one. If the curvature of the isentrop takes on negative values the thermodynamic as well as the flow behaviour changes completely. In the seventies Thompson and co-workers [32], [33], [23] started to investigate hydrocarbons and flour carbons which have a complex molecule structure and large values of the specific heats. It was found that this group of gases possess a region where the fundamental derivative becomes negative. More recently, the properties of flour carbons were investigated by Cramer [8]. As shown by Cramer and Best [10], Cramer and Fry [12] and Kluwick [19], the isentropic compression/expansion of a BZT fluid may cause the local Mach number to increase/decrease which is the opposite to the behaviour of regular fluids. Viscous effects of BZT fluids at high Reynolds number were studied by Zieher [35] on the basis of classical hierarchal boundary layer theory (e.g. Batchelor [2]). Other studies dealing with viscous dense gas flows were made by Cramer and Whitlock [14], Cramer and Park [13] and most recently Kluwick et al [21] using a triple deck approach to a viscous inviscous interaction for a transonic flow at high Reynolds number in slender channels. In general, the boundary layer solution of a regular fluid exposed to an adverse pressure gradient terminates with a Goldstein singularity [15] and cannot be continued through the point of vanishing skin friction. If the strength of the Goldstein singularity becomes arbitrary small, however, as some control parameter approaches a critical value, the boundary layer experiences a marginal separation i.e. a small region with reversed flow which re-attaches. This phenomena was studied first for incompressible flows past an airfoil by Ruban [27], [28], Stewartson et al [30]. It was found that there exists a limiting solution of the boundary layer equations which can be extended through a point of vanishing wall shear. This solution is embedded in one parameter family of solutions which describes the transition from completely smooth wall shear distributions to wall shear distributions which terminate in a separation singularity depending on a certain control parameter mentioned above. In [27], [28], [30] the control parameter was the angle of attack and the marginal separation was triggered by the pressure gradient distribution on the airfoil. The accuracy of this asymptotic approach was studied by Braun et

al [5] by comparing it to the results of Navier-Stokes computations with DLR's TAU-code. The quantitative agreement concerning the location and size of the separation bubble was shown to be excellent.

This work is divided in three Chapters. In the first one the problem is stated and the governing equations are derived. The aim of this study is to examine boundary layer dense gas effects and Chapter 2 is, therefore, dedicated to a numerical analysis of the boundary layer equations for supersonic and subsonic flows with adverse as well as favourable pressure gradient. Depending on the distribution of the fundamental derivative, the Mach number may decrease/increase in an accelerating/decelerating supersonic flow and be negative/positive for the boundary layer evolution. For the latter case, if the freestream conditions are suitable chosen, the boundary layer will experience a marginal separation. This phenomena is examined by means of asymptotic theory in Chapter 3. In contrast, however, to the studies done by Ruban, Stewartson et al the free stream density is chosen as control parameter and the marginal separation is not caused by a specific form of the pressure distribution but rather by the non monotonous Mach number distribution.

Abstract

Dense gases with complex molecular structure may behave in an unexpectedly manner, in some cases on the contrary to regular fluids. In the present study, supersonic as well as subsonic boundary layer flows of dense gases are numerically solved. It is shown that a supersonic accelerating/decelerating dense gas may be negative/positive for the boundary layer evolution. In the latter case, special attention is given the phenomena where the wall shear stress almost vanishes in a single point but then recovers and increases. Incompressible high Reynolds number flows past a slender airfoil have the distinguishing property that there exists a critical value of the angle of attack where the wall shear stress on the suction side vanishes in a single point but immediately recovers. This phenomenon is now commonly referred to as marginal separation. In this work it is shown that a laminar boundary layer on a flat plate subjected to a linearly retarded external flow may experience a similar behaviour if the molecular complexity of the medium is sufficiently large. The role of the critical angle of attack is played by the critical value of the free stream density ρ_∞^c on a given isentrop. As in the case of a slender airfoil it is possible to construct an asymptotic theory which allows to calculate small separation bubbles which form if ρ_∞ is smaller than ρ_∞^c .

Contents

Preface	I
Abstract	III
Contents	IV
List of Figures	XI
List of Tables	XI
1 Boundary layer flows	1
1.1 Problem formulation	1
2 Numerical solution of the boundary layer	7
2.1 Transformation of the boundary layer equations	7
2.2 Linearly retarded supersonic boundary layer flow	8
2.3 Linearly accelerating supersonic boundary layer flow	37
2.4 Linearly retarded subsonic boundary layer flow	47
2.5 Linearly accelerating subsonic boundary layer flow	54
3 Asymptotic theory of marginal separation in dense gases	62
3.1 Thermodynamical considerations	64
3.2 Properties of a classical boundary layer near the point of vanishing wall shear stress	65
3.3 Local Interaction process	73
4 Conclusions	83
References	87
Appendix A	88
Appendix B	89
Lebenslauf	93

List of Figures

1	Flow past a flat plate. Here, the external flow velocity decreases linearly with the distance from the tip of the plate.	1
2	pv -diagram for FC-71 ($C_{18}F_{39}N$). The pressure \tilde{p} and specific volume \tilde{v} have been non-dimensionalized with their critical values \tilde{p}_c and \tilde{v}_c . All quantities are calculated with Martin and Hou's equation of state.	5
3	Thermodynamic state at the outer edge of the boundary layer for FC-71. The isentropes with start and end state for the cases C2 and C3 are represented by the dashed lines.	10
4	Thermodynamic state at the outer edge of the boundary layer for PP11. The isentropes with start and end state for the cases C2 and C3 are represented by the dashed lines.	10
5	Thermodynamic state at the outer edge of the boundary layer for N_2 . The isentropes with start and end state for the cases C2 and C3 are represented by the dashed lines.	11
6	Variations of the local Eckert number across the boundary layer at the leading edge of the plate $x = 0$ and at the point of separation x_s : FC-71, case C1.	11
7	Variations of the local Eckert number across the boundary layer at the leading edge of the plate $x = 0$ and at the point of separation x_s : PP11, case C1.	12
8	Variations of the local Eckert number across the boundary layer at the leading edge of the plate $x = 0$ and at the point of separation x_s : N_2 , case C1.	12
9	Velocity distributions at the leading edge of the plate $x = 0$: Blasius similarity solution, FC-71, PP11, N_2 , case C1.	13
10	Temperature variation across the boundary layer at the leading edge of the plate $x = 0$ and at the point of separation x_s : FC-71, case C1.	14
11	Temperature variation across the boundary layer at the leading edge of the plate $x = 0$ and at the point of separation x_s : PP11, case C1.	14
12	Temperature variation across the boundary layer at the leading edge of the plate $x = 0$ and at the point of separation x_s : N_2 , case C1.	15
13	Density variation at the edge of the boundary layer: case C1.	15
14	Density variation across the boundary layer at the leading edge of the plate $x = 0$ and at the point of separation x_s : FC-71, case C1.	16

15	Density variation across the boundary layer at the leading edge of the plate $x = 0$ and at the point of separation x_s : PP11, case C1. . .	16
16	Density variation across the boundary layer at the leading edge of the plate $x = 0$ and at the point of separation x_s : N_2 , case C1. . . .	17
17	Change in entropy across the boundary layer at the leading edge of the plate $x = 0$ and at the point of separation x_s : FC-71, case C1. .	17
18	Change in entropy across the boundary layer at the leading edge of the plate $x = 0$ and at the point of separation x_s : PP11, case C1. .	18
19	Change in entropy across the boundary layer at the leading edge of the plate $x = 0$ and at the point of separation x_s : N_2 , case C1. . .	18
20	Distributions of the friction coefficient: case C1.	19
21	Distributions of the displacement thickness: case C1.	19
22	Velocity distributions at the leading edge of the plate $x = 0$: Blasius similarity solution, FC-71, PP11, N_2 , case C2.	21
23	Temperature variation across the boundary layer at the leading edge of the plate $x = 0$, at the point of recovery x_r and at the point of separation x_s : FC-71, case C2.	22
24	Temperature variation across the boundary layer at the leading edge of the plate $x = 0$ and at the point of separation x_s : PP11, case C2.	22
25	Temperature variation across the boundary layer at the leading edge of the plate $x = 0$ and at the point of separation x_s : N_2 , case C2.	23
26	Density variation at the edge of the boundary layer: case C2. . . .	23
27	Density variation across the boundary layer at the leading edge of the plate $x = 0$, at the point of recovery x_r , and at the point of separation x_s : FC-71, case C2.	24
28	Density variation across the boundary layer at the leading edge of the plate $x = 0$ and at the point of separation x_s : PP11, case C2. . .	24
29	Density variation across the boundary layer at the leading edge of the plate $x = 0$ and at the point of separation x_s : N_2 , case C2. . . .	25
30	Change in entropy across the boundary layer at the leading edge of the plate $x = 0$, at the point of recovery x_r , and at the point of separation x_s : FC-71, case C2.	25
31	Change in entropy across the boundary layer at the leading edge of the plate $x = 0$ and at the point of separation x_s : PP11, case C2. .	26
32	Change in entropy across the boundary layer at the leading edge of the plate $x = 0$ and at the point of separation x_s : N_2 , case C2. . .	26
33	Distributions of the friction coefficient: case C2.	27
34	Distributions of the displacement thickness: case C2.	27

35	Distributions of the fundamental derivative at the boundary layer edge: case C2.	28
36	Mach number distribution at the boundary layer edge: case C2. . .	28
37	pv -diagram for FC-71. Upstream states within the shaded area lead to wall shear stress distributions with a pronounced minimum while states outside this domain exhibit a Goldstein separation singularity in linearly retarded flows with $M_\infty = 2.0$, $\zeta = -1$. . .	29
38	Friction coefficient for FC-71 at $\tilde{T}_\infty = 1.001\tilde{T}_c$, $\tilde{v}_\infty = 5.5\tilde{v}_c$, $M_\infty = 2.0$, i.e. above the curve of marginal separation.	29
39	Velocity distributions at the leading edge of the plate $x = 0$: Blasius similarity solution, FC-71, N ₂ , case C3.	30
40	Temperature variation across the boundary layer at the leading edge of the plate $x = 0$ and at the point of separation x_s : FC-71, case C3.	31
41	Temperature variation across the boundary layer at the leading edge of the plate $x = 0$ and at the point of separation x_s : PP11, case C3.	31
42	Temperature variation across the boundary layer at the leading edge of the plate $x = 0$ and at the point of separation x_s : N ₂ , case C3.	32
43	Density variation at the edge of the boundary layer: case C3. . . .	32
44	Density variation across the boundary layer at the leading edge of the plate $x = 0$ and at the point of separation x_s : FC-71, case C3. .	33
45	Density variation across the boundary layer at the leading edge of the plate $x = 0$ and at the point of separation x_s : PP11, case C3. .	33
46	Density variation across the boundary layer at the leading edge of the plate $x = 0$ and at the point of separation x_s : N ₂ , case C3. . . .	34
47	Variations of the isobaric heat capacity across the boundary layer at the leading edge of the plate $x = 0$: N ₂ , case C3.	34
48	Change in entropy across the boundary layer at the leading edge of the plate $x = 0$ and at the point of separation x_s : FC-71, case C3. .	35
49	Change in entropy across the boundary layer at the leading edge of the plate $x = 0$ and at the point of separation x_s : PP11, case C3. .	35
50	Change in entropy across the boundary layer at the leading edge of the plate $x = 0$ and at the point of separation x_s : N ₂ , case C3. .	36
51	Distributions of the friction coefficient: case C3.	36
52	Distributions of the displacement thickness: case C3.	37
53	Velocity distributions at the leading edge of the plate $x = 0$: Blasius similarity solution FC-71, PP11, N ₂ , $M_\infty = 2.0$, $\tilde{v}_\infty = 1.05\tilde{v}_c$, $\tilde{T}_\infty = 1.001\tilde{T}_c$	39

54	Temperature variation across the boundary layer at the leading edge of the plate $x = 0$ and at $x = 0.1$: FC-71, $M_\infty = 2.0$, $\tilde{v}_\infty = 1.05\tilde{v}_c$, $\tilde{T}_\infty = 1.001\tilde{T}_c$	39
55	Temperature variation across the boundary layer at the leading edge of the plate $x = 0$ and at $x = 0.1$: PP11, $M_\infty = 2.0$, $\tilde{v}_\infty = 1.05\tilde{v}_c$, $\tilde{T}_\infty = 1.001\tilde{T}_c$	40
56	Temperature variation across the boundary layer at the leading edge of the plate $x = 0$ and at $x = 0.1$: N ₂ , $M_\infty = 2.0$, $\tilde{v}_\infty = 1.05\tilde{v}_c$, $\tilde{T}_\infty = 1.001\tilde{T}_c$	40
57	Density variation across the boundary layer at the leading edge of the plate $x = 0$ and at $x = 0.1$: FC-71, $M_\infty = 2.0$, $\tilde{v}_\infty = 1.05\tilde{v}_c$, $\tilde{T}_\infty = 1.001\tilde{T}_c$	41
58	Density variation across the boundary layer at the leading edge of the plate $x = 0$ and at $x = 0.1$: PP11, $M_\infty = 2.0$, $\tilde{v}_\infty = 1.05\tilde{v}_c$, $\tilde{T}_\infty = 1.001\tilde{T}_c$	41
59	Density variation across the boundary layer at the leading edge of the plate $x = 0$ and at $x = 0.1$: N ₂ , $M_\infty = 2.0$, $\tilde{v}_\infty = 1.05\tilde{v}_c$, $\tilde{T}_\infty = 1.001\tilde{T}_c$	42
60	Entropy variation across the boundary layer at the leading edge of the plate $x = 0$ and at $x = 0.1$: FC-71, $M_\infty = 2.0$, $\tilde{v}_\infty = 1.05\tilde{v}_c$, $\tilde{T}_\infty = 1.001\tilde{T}_c$	42
61	Entropy variation across the boundary layer at the leading edge of the plate $x = 0$ and at $x = 0.1$: PP11, $M_\infty = 2.0$, $\tilde{v}_\infty = 1.05\tilde{v}_c$, $\tilde{T}_\infty = 1.001\tilde{T}_c$	43
62	Entropy variation across the boundary layer at $x = 0$ and at the leading edge of the plate $x = 0.1$: N ₂ , $M_\infty = 2.0$, $\tilde{v}_\infty = 1.05\tilde{v}_c$, $\tilde{T}_\infty = 1.001\tilde{T}_c$	43
63	Distributions of the friction coefficient: $M_\infty = 2.0$, $v_\infty = 1.05v_c$, $T_\infty = 1.001T_c$	44
64	Mach number distribution at the boundary layer edge: $M_\infty = 2.0$, $v_\infty = 1.05v_c$, $T_\infty = 1.001T_c$	44
65	Distributions of the friction coefficient: $M_\infty = 1.3$, $\tilde{v}_\infty = 0.71\tilde{v}_c$, $\tilde{T}_\infty = 1.03\tilde{T}_c$	45
66	Distributions of the displacement thickness: $M_\infty = 1.3$, $\tilde{v}_\infty = 0.71\tilde{v}_c$, $\tilde{T}_\infty = 1.03\tilde{T}_c$	45
67	Mach number distribution at the boundary layer edge: $M_\infty = 1.3$, $\tilde{v}_\infty = 0.71\tilde{v}_c$, $\tilde{T}_\infty = 1.03\tilde{T}_c$	46
68	Distributions of the fundamental derivative at the boundary layer edge: $M_\infty = 1.3$, $\tilde{v}_\infty = 0.71\tilde{v}_c$, $\tilde{T}_\infty = 1.03\tilde{T}_c$	46

69	Velocity distributions at the leading edge of the plate $x = 0$: Blasius similarity solution, FC-71, PP11, N_2 , $M_\infty = 0.2$, $\tilde{v}_\infty = 5.0\tilde{v}_c$, $\tilde{T}_\infty = 1.001\tilde{T}_c$	47
70	Temperature variation across the boundary layer at the leading edge of the plate $x = 0$ and at the point of separation x_s : FC-71, $M_\infty = 0.2$, $\tilde{v}_\infty = 5.0\tilde{v}_c$, $\tilde{T}_\infty = 1.001\tilde{T}_c$	48
71	Temperature variation across the boundary layer at the leading edge of the plate $x = 0$ and at the point of separation x_s : PP11, $M_\infty = 0.2$, $\tilde{v}_\infty = 5.0\tilde{v}_c$, $\tilde{T}_\infty = 1.001\tilde{T}_c$	48
72	Temperature variation across the boundary layer at the leading edge of the plate $x = 0$ and at the point of separation x_s : N_2 , $M_\infty = 0.2$, $\tilde{v}_\infty = 5.0\tilde{v}_c$, $\tilde{T}_\infty = 1.001\tilde{T}_c$	49
73	Density variation at the edge of the boundary layer: $M_\infty = 0.2$, $\tilde{v}_\infty = 5.0\tilde{v}_c$, $\tilde{T}_\infty = 1.001\tilde{T}_c$	49
74	Density variation across the boundary layer at the leading edge of the plate $x = 0$ and at the point of separation x_s : FC-71, $M_\infty = 0.2$, $\tilde{v}_\infty = 5.0\tilde{v}_c$, $\tilde{T}_\infty = 1.001\tilde{T}_c$	50
75	Density variation across the boundary layer at the leading edge of the plate $x = 0$ and at the point of separation x_s : PP11, $M_\infty = 0.2$, $\tilde{v}_\infty = 5.0\tilde{v}_c$, $\tilde{T}_\infty = 1.001\tilde{T}_c$	50
76	Density variation across the boundary layer at the leading edge of the plate $x = 0$ and at the point of separation x_s : N_2 , $M_\infty = 0.2$, $\tilde{v}_\infty = 5.0\tilde{v}_c$, $\tilde{T}_\infty = 1.001\tilde{T}_c$	51
77	Entropy variation across the boundary layer at the leading edge of the plate $x = 0$ and at the point of separation x_s : FC-71, $M_\infty = 0.2$, $\tilde{v}_\infty = 5.0\tilde{v}_c$, $\tilde{T}_\infty = 1.001\tilde{T}_c$	51
78	Entropy variation across the boundary layer at the leading edge of the plate $x = 0$ and at the point of separation x_s : PP11, $M_\infty = 0.2$, $\tilde{v}_\infty = 5.0\tilde{v}_c$, $\tilde{T}_\infty = 1.001\tilde{T}_c$	52
79	Entropy variation across the boundary layer at the leading edge of the plate $x = 0$ and at the point of separation x_s : N_2 , $M_\infty = 0.2$, $\tilde{v}_\infty = 5.0\tilde{v}_c$, $\tilde{T}_\infty = 1.001\tilde{T}_c$	52
80	Distributions of the friction coefficient: $M_\infty = 0.2$, $\tilde{v}_\infty = 5.0\tilde{v}_c$, $\tilde{T}_\infty = 1.001\tilde{T}_c$	53
81	Distributions of the displacement thickness: $M_\infty = 0.2$, $\tilde{v}_\infty = 5.0\tilde{v}_c$, $\tilde{T}_\infty = 1.001\tilde{T}_c$	53
82	Mach number distribution at the boundary layer edge: $M_\infty = 0.2$, $\tilde{v}_\infty = 5.0\tilde{v}_c$, $\tilde{T}_\infty = 1.001\tilde{T}_c$	54
83	Velocity distributions at the leading edge of the plate $x = 0$: Blasius similarity solution, FC-71, PP11, N_2 , $M_\infty = 0.2$, $\tilde{v}_\infty = 5.0\tilde{v}_c$, $\tilde{T}_\infty = 1.001\tilde{T}_c$	55

84	Temperature variation across the boundary layer at the leading edge of the plate $x = 0$ and at the end of the plate $x = 1$: FC-71, $M_\infty = 0.2$, $\tilde{v}_\infty = 5.0\tilde{v}_c$, $\tilde{T}_\infty = 1.001\tilde{T}_c$	55
85	Temperature variation across the boundary layer at the leading edge of the plate $x = 0$ and at the end of the plate $x = 1$: PP11, $M_\infty = 0.2$, $\tilde{v}_\infty = 5.0\tilde{v}_c$, $\tilde{T}_\infty = 1.001\tilde{T}_c$	56
86	Temperature variation across the boundary layer at the leading edge of the plate $x = 0$ and at the end of the plate $x = 1$: N ₂ , $M_\infty = 0.2$, $\tilde{v}_\infty = 5.0\tilde{v}_c$, $\tilde{T}_\infty = 1.001\tilde{T}_c$	56
87	Density variation at the edge of the boundary layer: $M_\infty = 0.2$, $\tilde{v}_\infty = 5.0\tilde{v}_c$, $\tilde{T}_\infty = 1.001\tilde{T}_c$	57
88	Density variation across the boundary layer at the leading edge of the plate $x = 0$ and at the end of the plate $x = 1$: FC-71, $M_\infty = 0.2$, $\tilde{v}_\infty = 5.0\tilde{v}_c$, $\tilde{T}_\infty = 1.001\tilde{T}_c$	57
89	Density variation across the boundary layer at the leading edge of the plate $x = 0$ and at the end of the plate $x = 1$: PP11, $M_\infty = 0.2$, $\tilde{v}_\infty = 5.0\tilde{v}_c$, $\tilde{T}_\infty = 1.001\tilde{T}_c$	58
90	Density variation across the boundary layer at the leading edge of the plate $x = 0$ and at the end of the plate $x = 1$: N ₂ , $M_\infty = 0.2$, $\tilde{v}_\infty = 5.0\tilde{v}_c$, $\tilde{T}_\infty = 1.001\tilde{T}_c$	58
91	Entropy variation across the boundary layer at the leading edge of the plate $x = 0$ and at the end of the plate $x = 1$: FC-71, $M_\infty = 0.2$, $\tilde{v}_\infty = 5.0\tilde{v}_c$, $\tilde{T}_\infty = 1.001\tilde{T}_c$	59
92	Entropy variation across the boundary layer at the leading edge of the plate $x = 0$ and at the end of the plate $x = 1$: PP11, $M_\infty = 0.2$, $\tilde{v}_\infty = 5.0\tilde{v}_c$, $\tilde{T}_\infty = 1.001\tilde{T}_c$	59
93	Entropy variation across the boundary layer at the leading edge of the plate $x = 0$ and at the end of the plate $x = 1$: N ₂ , $M_\infty = 0.2$, $\tilde{v}_\infty = 5.0\tilde{v}_c$, $\tilde{T}_\infty = 1.001\tilde{T}_c$	60
94	Distributions of the friction coefficient: $M_\infty = 0.2$, $\tilde{v}_\infty = 5.0\tilde{v}_c$, $\tilde{T}_\infty = 1.001\tilde{T}_c$	60
95	Distributions of the displacement thickness: $M_\infty = 0.2$, $\tilde{v}_\infty = 5.0\tilde{v}_c$, $\tilde{T}_\infty = 1.001\tilde{T}_c$	61
96	Mach number distribution at the boundary layer edge: $M_\infty = 0.2$, $\tilde{v}_\infty = 5.0\tilde{v}_c$, $\tilde{T}_\infty = 1.001\tilde{T}_c$	61
97	Marginal separation for the BZT-fluid FC-71 at $\rho_{\infty r} = 0.1996$ $T_{\infty r} = 1.001$ and $M_\infty = 2.0$. The region where the friction coefficient recovers is the region of interest in this section.	62
98	Numerical calculation of the boundary layer. Friction coefficient distribution for FC-71 at $T_{\infty r} = 1.001$ and $M_\infty = 2.0$	63

99	Numerical solution of the boundary layer equations for FC-71, $Ec = 0$, $T_{\infty r} = 1.001$, $\rho_{\infty r} = 0.17$ and $M_{\infty} = 2.0$	65
100	Asymptotic structure of the boundary layer close to the point of zero wall shear.	66
101	The triple deck structure in the interaction region.	75
102	Numerical solution of $\hat{A}(\hat{X})$ for various values of the controlling parameter $\lambda \propto Re^{2/5} k_1$	80
103	Comparison between marginal separation theory and classical boundary layer theory (dashed).	81
104	The fundamental curve showing non-uniqueness of flow.	82
105	Predictions of the shear viscosity for FC-71 using the method from Chung et al. All quantities are non-dimensionalized with their values at the thermodynamic critical point.	89
106	Predictions of the shear viscosity for PP11 using the method from Chung et al. All quantities are non-dimensionalized with their values at the thermodynamic critical point.	90
107	Predictions of the shear viscosity for N_2 using the method from Chung et al. All quantities are non-dimensionalized with their values at the thermodynamic critical point.	90
108	Predictions of the thermal conductivity for FC-71 using the method from Chung et al. All quantities are non-dimensionalized with their values at the thermodynamic critical point.	91
109	Predictions of the thermal conductivity for PP11 using the method from Chung et al. All quantities are non-dimensionalized with their values at the thermodynamic critical point.	91
110	Predictions of the thermal conductivity for N_2 using the method from Chung et al. All quantities are non-dimensionalized with their values at the thermodynamic critical point.	92

List of Tables

1	Free stream velocity \tilde{u}_{∞} and Eckert number α_{∞}	9
2	Free stream velocity and Eckert number: $M_{\infty} = 2.0$, $\tilde{v}_{\infty} = 1.05\tilde{v}_c$, $\tilde{T}_{\infty} = 1.001\tilde{T}_c$	37
3	Free stream velocity and Eckert number: $M_{\infty} = 1.3$, $\tilde{v}_{\infty} = 0.71\tilde{v}_c$, $\tilde{T}_{\infty} = 1.03\tilde{T}_c$	38
4	$c_{v\infty}^c$ for representative negative Γ fluids. $\Gamma_{min}(T_c)$ denotes the minimum value of Γ on the critical isotherm [8].	64
5	Input parameters for shear viscosity, thermal conductivity and pressure.	88

1 Boundary layer flows

1.1 Problem formulation

We consider the laminar and stationary flow of a viscous and compressible fluid in the thermodynamic single-phase region past a thin aligned flat plate of length \tilde{L} , Fig 1. In particular, we want to examine supersonic flows with linear retarded external velocity (Howarth-problem [18]) for Bethe-Zel'dovich-Thompson fluids close to the critical point. However, supersonic accelerated as well as retarded and accelerated subsonic flows will be treated also. BZT-fluids are heavy gases with complex molecular structures and are characterised by large values of the isochoric heat capacity, \tilde{c}_v [8]. By limiting the work to Newtonian fluids without

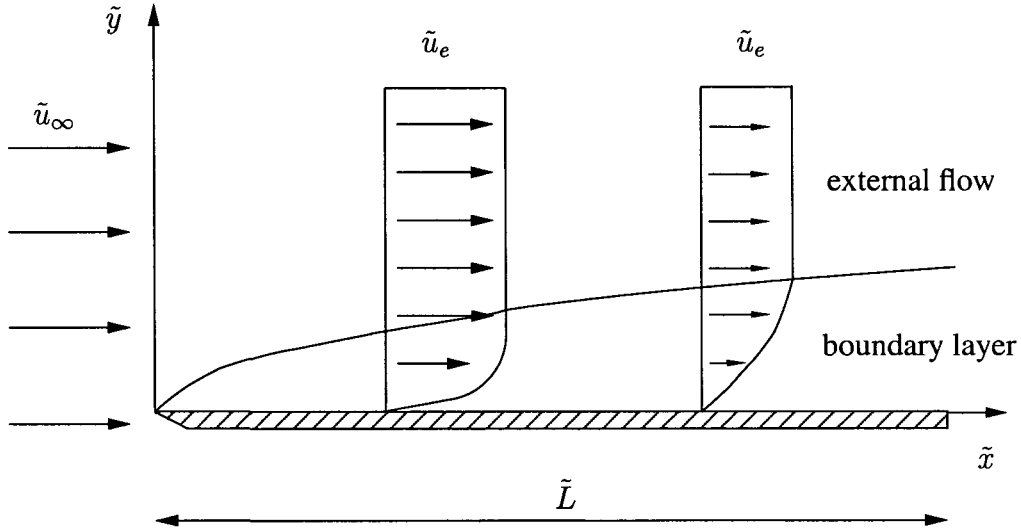


Figure 1: Flow past a flat plate. Here, the external flow velocity decreases linearly with the distance from the tip of the plate.

body forces, the flow is described by the continuity equation and Navier-Stokes equation supplemented with the energy equation

$$\nabla \cdot (\tilde{\rho} \tilde{\mathbf{u}}) = 0, \quad (1.1)$$

$$\tilde{\rho} \frac{D\tilde{u}_i}{D\tilde{t}} = -\frac{\partial \tilde{p}}{\partial \tilde{x}_i} + \frac{\partial}{\partial \tilde{x}_j} \left(\tilde{\mu} \left(\frac{\partial \tilde{u}_i}{\partial \tilde{x}_j} + \frac{\partial \tilde{u}_j}{\partial \tilde{x}_i} \right) + \tilde{\lambda} (\nabla \cdot \tilde{\mathbf{u}}) \delta_{ij} \right), \quad (1.2)$$

$$\tilde{\rho} \tilde{c}_p \frac{D\tilde{T}}{D\tilde{t}} = \nabla \cdot (\tilde{k} \nabla \tilde{T}) + \tilde{\beta} \tilde{T} \frac{D\tilde{p}}{D\tilde{t}} + \tilde{\Phi}. \quad (1.3)$$

Here, δ_{ij} , ∇ , $D/D\tilde{t}$ represent the Kronecker delta tensor, the vector operator and the material derivative

$$\nabla \equiv \mathbf{a}^i \frac{\partial}{\partial \tilde{x}_i},$$

$$\frac{D}{D\tilde{t}} \equiv \tilde{u}_i \frac{\partial}{\partial \tilde{x}_i},$$

where \mathbf{a}^i are the unit vectors. Further, $\tilde{\mathbf{u}}$, \tilde{u}_i , \tilde{x}_i , $\tilde{\rho}$, \tilde{T} , \tilde{p} , $\tilde{\mu}$, $\tilde{\lambda}$, $\tilde{\beta}$, \tilde{k} and \tilde{c}_p denote the velocity vector, velocity components, Cartesian coordinates, the density, temperature, pressure, shear viscosity, bulk viscosity, coefficient of thermal expansion, thermal conductivity and specific heat at constant pressure, respectively. In the energy equation (1.3) the specific enthalpy has been expressed as function of pressure and temperature

$$d\tilde{h} = \tilde{c}_p d\tilde{T} + (1 - \tilde{\beta}\tilde{T}) \frac{d\tilde{p}}{\tilde{\rho}}, \quad \tilde{\beta} = -\frac{1}{\tilde{\rho}} \left. \frac{\partial \tilde{\rho}}{\partial \tilde{T}} \right|_p. \quad (1.4)$$

and the last term in (1.3), $\tilde{\Phi}$, is the dissipation function

$$\tilde{\Phi} = \left(\tilde{\mu} \left(\frac{\partial \tilde{u}_i}{\partial \tilde{x}_j} + \frac{\partial \tilde{u}_j}{\partial \tilde{x}_i} \right) + \tilde{\lambda} (\nabla \cdot \tilde{\mathbf{u}}) \delta_{ij} \right)^2. \quad (1.5)$$

(1.1), (1.2), (1.3) are non-dimensionalized using the properties of the oncoming flow and the length \tilde{L} of the plate as reference values

$$x = \frac{\tilde{x}}{\tilde{L}}, \quad y = \frac{\tilde{y}}{\tilde{L}}, \quad T = \frac{\tilde{T}}{\tilde{T}_\infty}, \quad \rho = \frac{\tilde{\rho}}{\tilde{\rho}_\infty}, \quad p = \frac{\tilde{p}}{\tilde{\rho}_\infty \tilde{u}_\infty^2}, \quad \mu = \frac{\tilde{\mu}}{\tilde{\mu}_\infty},$$

$$\lambda = \frac{\tilde{\lambda}}{\tilde{\lambda}_\infty}, \quad \beta = \frac{\tilde{\beta}}{\tilde{\beta}_\infty}, \quad c_p = \frac{\tilde{c}_p}{\tilde{c}_{p\infty}}, \quad k = \frac{\tilde{k}}{\tilde{k}_\infty}, \quad u = \frac{\tilde{u}}{\tilde{u}_\infty}, \quad v = \frac{\tilde{v}}{\tilde{u}_\infty}. \quad (1.6)$$

Here (x, y) , (u, v) denote Cartesian coordinates parallel and normal to the plate surface and the corresponding velocity components. Quantities without the superscript \sim are non-dimensional. The subscripts ∞ and e characterise values of the oncoming flow and at the edge of the boundary layer, respectively. We then obtain

$$\frac{\partial}{\partial x}(\rho u) + \frac{\partial}{\partial y}(\rho v) = 0, \quad (1.7)$$

$$\begin{aligned} \rho u \frac{\partial u}{\partial x} + \rho v \frac{\partial u}{\partial y} &= -\frac{\partial p}{\partial x} + \frac{1}{Re} \frac{\partial}{\partial x} \left((2\mu + \lambda) \frac{\partial u}{\partial x} + \lambda \frac{\partial v}{\partial y} \right) \\ &+ \frac{1}{Re} \frac{\partial}{\partial y} \left(\mu \frac{\partial u}{\partial y} + \mu \frac{\partial v}{\partial x} \right), \end{aligned} \quad (1.8)$$

$$\begin{aligned} \rho u \frac{\partial v}{\partial x} + \rho v \frac{\partial v}{\partial y} &= -\frac{\partial p}{\partial y} + \frac{1}{Re} \frac{\partial}{\partial y} \left((2\mu + \lambda) \frac{\partial v}{\partial y} + \lambda \frac{\partial u}{\partial x} \right) \\ &+ \frac{1}{Re} \frac{\partial}{\partial x} \left(\mu \frac{\partial u}{\partial y} + \mu \frac{\partial v}{\partial x} \right), \end{aligned} \quad (1.9)$$

$$\begin{aligned} c_p \rho \left(u \frac{\partial T}{\partial x} + v \frac{\partial T}{\partial y} \right) - Ec \tilde{\beta}_\infty \tilde{T}_\infty \beta T \left(u \frac{\partial p}{\partial x} - v \frac{\partial p}{\partial y} \right) \\ = \frac{1}{Pr Re} \frac{\partial}{\partial x} \left(k \frac{\partial T}{\partial x} \right) + 2 \frac{Ec}{Re} \left(\lambda \frac{\partial u}{\partial x} \frac{\partial v}{\partial y} + \mu \frac{\partial v}{\partial x} \frac{\partial u}{\partial y} \right) \\ + \frac{1}{Pr Re} \frac{\partial}{\partial y} \left(k \frac{\partial T}{\partial y} \right) + \frac{Ec}{Re} \mu \left(\left(\frac{\partial v}{\partial x} \right)^2 + \left(\frac{\partial u}{\partial y} \right)^2 \right) \\ + \frac{Ec}{Re} (2\mu + \lambda) \left(\left(\frac{\partial u}{\partial x} \right)^2 + \left(\frac{\partial v}{\partial y} \right)^2 \right), \end{aligned} \quad (1.10)$$

where

$$Re = \frac{\tilde{u}_\infty \tilde{\rho}_\infty \tilde{L}}{\tilde{\mu}_\infty}, \quad Pr = \frac{\tilde{c}_{p\infty} \tilde{\mu}_\infty}{\tilde{k}_\infty}, \quad Ec = \frac{\tilde{u}_\infty^2}{\tilde{c}_{p\infty} \tilde{T}_\infty} \quad (1.11)$$

denote the Reynolds number, Prandtl number and Eckert number, respectively. In the following we shall assume that the Reynolds number is large so that viscous effects are confined to a thin boundary layer near the solid wall where the no-slip condition has to be satisfied. By scaling y and v in the usual manner

$$Y = y\sqrt{Re}, \quad V = v\sqrt{Re} \quad (1.12)$$

the non-dimensional boundary layer equations are then obtained in the limit $Re \rightarrow \infty$.

$$\frac{\partial}{\partial x}(\rho u) + \frac{\partial}{\partial Y}(\rho V) = 0, \quad (1.13)$$

$$\rho u \frac{\partial u}{\partial x} + \rho V \frac{\partial u}{\partial Y} = -\frac{dp}{dx} + \frac{\partial}{\partial Y} \left(\mu \frac{\partial u}{\partial Y} \right) \quad (1.14)$$

$$\frac{\partial p}{\partial Y} = 0 \quad (1.15)$$

$$\begin{aligned} \rho c_p \left(u \frac{\partial T}{\partial x} + V \frac{\partial T}{\partial Y} \right) &= \beta \tilde{\beta}_\infty T \tilde{T}_\infty Ec u \frac{dp}{dx} + \frac{1}{Pr} \frac{\partial}{\partial Y} \left(k \frac{\partial T}{\partial Y} \right) \\ &+ \mu Ec \left(\frac{\partial u}{\partial Y} \right)^2 \end{aligned} \quad (1.16)$$

The boundary layer equations (1.13), (1.14), (1.15), (1.16) are subjected to the boundary conditions

$$\begin{aligned}
Y = 0 & : u = V = 0, \quad \frac{\partial T}{\partial Y} = 0, \\
Y \rightarrow \infty & : u \rightarrow u_e, \quad T \rightarrow T_e, \\
& s_e(\rho_e, T_e) = \text{const}, \\
& \frac{dp_e}{dx} = -\rho_e u_e \frac{du_e}{dx}, \\
& u_e = 1 + \zeta x, \quad \zeta \pm 1.
\end{aligned} \tag{1.17}$$

On the plate, $Y = 0$, we have the no-slip condition and the plate is taken to be adiabatic. On the outer edge of the boundary layer, $Y \rightarrow \infty$, the velocity u_e and the temperature T_e have to coincide with the values in the external irrotational, isentropical flow. Here, s denotes the specific entropy nondimensionalized with the freestream value of the isochoric heat capacity $\tilde{c}_{v\infty}$. Furthermore, the pressure p_e and velocity there satisfy the Bernoulli equation and as in the classical Howarth problem [18] also studied by Hartree [17], u_e is taken to vary linearly with distance x measured from the tip of the plate and the constant ζ represents the velocity gradient which is normalised to ± 1 by choosing \tilde{L} appropriately. For $\zeta = -1$ and $\zeta = 1$, the flow outside the boundary layer is decelerated and accelerated, respectively.

To close the problem the boundary layer equations and the boundary conditions have to be supplemented with thermal and caloric equations of state and relationships describing the variation of the thermal conductivity and the shear viscosity with temperature and density. As equation of state, the one suggested by Martin and Hou [25] was chosen

$$\begin{aligned}
\tilde{p}(\tilde{v}, \tilde{T}) = & \frac{R\tilde{T}}{\tilde{v} - b} + \frac{a_2 + b_2\tilde{T} + c_2e^{-5.475\tilde{T}/\tilde{T}_c}}{(\tilde{v} - b)^2} + \frac{a_3 + b_3\tilde{T} + c_3e^{-5.475\tilde{T}/\tilde{T}_c}}{(\tilde{v} - b)^3} \\
& + \frac{a_4}{(\tilde{v} - b)^4} + \frac{b_5\tilde{T} + c_5e^{-5.475\tilde{T}/\tilde{T}_c}}{(\tilde{v} - b)^5}.
\end{aligned} \tag{1.18}$$

Here, R is the universal gas constant, \tilde{v} the specific volume and \tilde{T}_c denotes the value of temperature at the thermodynamic critical point. Similar to the well known Van der Waals equation of state, the constant b , entering in the denominator, depends on the molecular size and is a measure of the excluded volume. The remaining constants a_i , b_i and c_i are depending upon the molecular weight, the values of pressure, temperature, and specific volume at the thermodynamic critical point and upon the normal boiling temperature. Among the thermal equations of state, capable of capturing dense gas effects, Martin and Hou has a strong

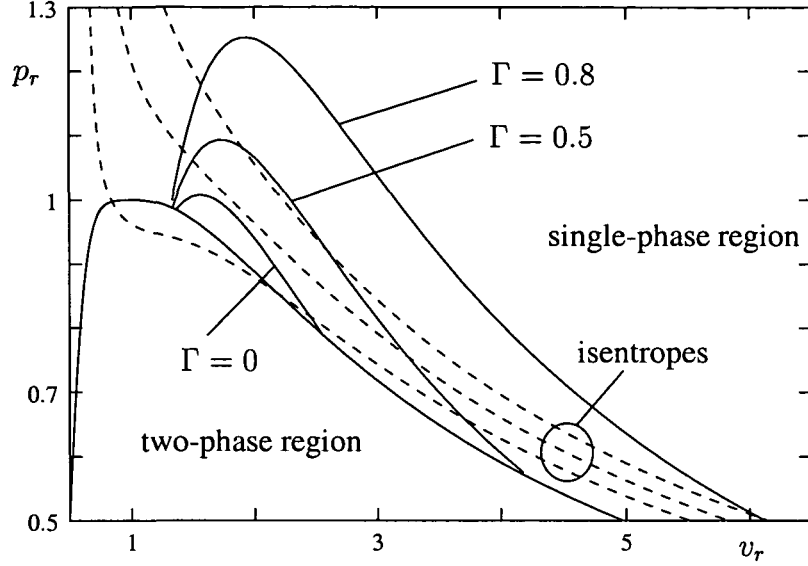


Figure 2: pv -diagram for FC-71 ($C_{18}F_{39}N$). The pressure \tilde{p} and specific volume \tilde{v} have been non-dimensionalized with their critical values \tilde{p}_c and \tilde{v}_c . All quantities are calculated with Martin and Hou's equation of state.

analytical basis and, therefore, requires a minimum of input data. Furthermore, it was found in [33] and [8] that Martin and Hou's equation of state is conservative with respect to predictions of negative nonlinearity, $\Gamma < 0$. Γ is referred to as the fundamental derivative and is associated with the curvature of isentropes in the pv -diagram

$$\Gamma = \frac{\tilde{v}^3}{2\tilde{a}^2} \left. \frac{\partial^2 \tilde{p}}{\partial \tilde{v}^2} \right|_s. \quad (1.19)$$

An example of the behaviour of Γ is displayed in Fig. 2 for the dense gas FC-71 which in opposite to ideal gases experiences a region of $\Gamma < 1$ in the general neighbourhood of the thermodynamic critical point.

We complete the description of the thermodynamical properties with the isobaric heat capacity. Standard thermodynamical relationships yield

$$\tilde{c}_p(\tilde{T}, \tilde{v}) = \tilde{c}_v(\tilde{T}, \tilde{v}) + \tilde{T}\tilde{v}\tilde{\beta} \left. \frac{\partial \tilde{p}}{\partial \tilde{T}} \right|_v, \quad (1.20)$$

where \tilde{c}_v denotes the isochoric heat capacity

$$\tilde{c}_v(\tilde{T}, \tilde{v}) = \tilde{c}_{v\infty}(\tilde{T}) - \tilde{T} \int_{\tilde{v}}^{\infty} \frac{\partial^2 \tilde{p}(\tilde{T}, \tilde{v})}{\partial \tilde{T}^2} d\tilde{v}. \quad (1.21)$$

Here, $\tilde{c}_{v\infty}(\tilde{T}) = \tilde{c}_v(\tilde{T}, \infty)$ represents the ideal gas isochoric heat capacity which is calculated using the group contribution method [26]

$$\tilde{c}_{v\infty}(\tilde{T}) = \tilde{c}_{v\infty}^c \left(\frac{\tilde{T}}{\tilde{T}_c} \right)^n, \quad (1.22)$$

where $\tilde{c}_{v\infty}^c$ is the ideal-gas isochoric heat capacity evaluated at the critical point and n is a material constant.

Finally, the shear viscosity $\tilde{\mu}$ and the thermal conductivity \tilde{k} are calculated using the methods presented by Chung, Lee and Starling in [7] and by Chung, Ajlan, Lee and Starling in [6]. The required input parameters are the molecular weight \tilde{M} , values of the specific volume and the temperature at the critical point, the accentric factor ω , the non-dimensional dipolmoment μ_r and the correction factor κ . Now, the objective of the present study is to examine boundary layer effects in dense gases. For this purpose two dense gases were chosen: PP11 ($C_{14}F_{24}$) and FC-71 ($C_{18}F_{39}N$). By examining two different dense gases it will be possible to recognise which properties are of crucial importance to the flow behaviour. Both PP11 and FC-71 belong to the group of substances termed BZT-fluids, in recognition to Bethe [3], Zel'dovich [34] and Thompson [32]. Further, as comparison to the behaviour of regular fluids the same calculations were also done for Nitrogen, N_2 . The parameters needed to calculate the shear viscosity, the thermal conductivity, the pressure (1.18) and the isochoric heat capacity (1.21) are listed in Appendix A and the resulting predictions for shear viscosity and thermal conductivity are displayed in Appendix B.

2 Numerical solution of the boundary layer

2.1 Transformation of the boundary layer equations

For numerical purposes it is convenient to write the boundary layer equations (1.13), (1.14), (1.16) in dimensional form

$$\frac{\partial}{\partial \tilde{x}}(\tilde{\rho}\tilde{u}) + \frac{\partial}{\partial \tilde{Y}}(\tilde{\rho}\tilde{V}) = 0, \quad (2.1)$$

$$\tilde{\rho}\tilde{u}\frac{\partial \tilde{u}}{\partial \tilde{x}} + \tilde{\rho}\tilde{V}\frac{\partial \tilde{u}}{\partial \tilde{Y}} = -\frac{d\tilde{p}}{d\tilde{x}} + \frac{\partial}{\partial \tilde{Y}}\left(\tilde{\mu}\frac{\partial \tilde{u}}{\partial \tilde{Y}}\right) \quad (2.2)$$

$$\tilde{\rho}\tilde{c}_p\left(\tilde{u}\frac{\partial \tilde{T}}{\partial \tilde{x}} + \tilde{V}\frac{\partial \tilde{T}}{\partial \tilde{Y}}\right) = \tilde{\beta}\tilde{T}\tilde{u}\frac{d\tilde{p}}{d\tilde{x}} + \frac{\partial}{\partial \tilde{Y}}\left(\tilde{k}\frac{\partial \tilde{T}}{\partial \tilde{Y}}\right) + \tilde{\mu}\left(\frac{\partial \tilde{u}}{\partial \tilde{Y}}\right)^2 \quad (2.3)$$

and to apply the Levy-Lees transformation [24]

$$\xi(\tilde{x}) = \tilde{K}\tilde{\rho}_\infty\tilde{\mu}_\infty\int_0^{\tilde{x}}\tilde{u}_e(x')dx', \quad (2.4)$$

$$\eta(\tilde{x}, \tilde{y}) = \tilde{u}_e(\tilde{x})\sqrt{\frac{\tilde{K}}{2\xi}}\int_0^{\tilde{y}}\tilde{\rho}(\tilde{x}, y')dy', \quad (2.5)$$

where the constant \tilde{K} denotes

$$\tilde{K} = (\tilde{\rho}_\infty\tilde{\mu}_\infty\tilde{u}_\infty\tilde{L})^{-1}.$$

We then obtain

$$f + 2\xi\frac{\partial f}{\partial \xi} + \frac{\partial g}{\partial \eta} = 0 \quad (2.6)$$

$$2\xi f\frac{\partial f}{\partial \xi}g\frac{\partial f}{\partial \eta} + m(f^2 - n) - \frac{\partial}{\partial \eta}\left(\ell\frac{\partial f}{\partial \eta}\right) = 0 \quad (2.7)$$

$$2\xi f\left(\frac{\partial \theta}{\partial \xi} + d\theta\right) + g\frac{\partial \theta}{\partial \eta} - \frac{1}{\tilde{c}_p}\frac{\partial}{\partial \eta}\left(\tilde{b}\frac{\partial \theta}{\partial \eta}\right) - \alpha\ell\left(\frac{\partial f}{\partial \eta}\right)^2 = 0 \quad (2.8)$$

The non dimensional velocity components f , g and the non-dimensional temperature θ are defined as

$$f = \frac{\tilde{u}}{\tilde{u}_e}, \quad (2.9)$$

$$g = \frac{2\xi}{\tilde{K}\tilde{\rho}_\infty\tilde{\mu}_\infty\tilde{u}_e} \left(f \frac{\partial \eta}{\partial \tilde{x}} + \tilde{\rho}\tilde{v} \sqrt{\frac{\tilde{K}}{2\xi}} \right), \quad (2.10)$$

$$\theta = \frac{\tilde{T}}{\tilde{T}_e}. \quad (2.11)$$

In the momentum equation (2.7) the parameters m , n and ℓ represent the velocity gradient, the density ratio and the Chapman-Rubens parameter, respectively

$$m = \frac{2\xi}{\tilde{u}_e} \frac{d\tilde{u}_e}{d\xi}, \quad n = \frac{\tilde{\rho}}{\tilde{\rho}_e}, \quad \ell = \frac{\tilde{\rho}\tilde{\mu}}{\tilde{\rho}_\infty\tilde{\mu}_\infty}. \quad (2.12)$$

Further, the quantities d , b and the local Eckert number α occurring in the energy equation are given by

$$\tilde{b} = \frac{\ell\tilde{c}_p}{Pr}, \quad d = \frac{1}{\tilde{T}_e} \frac{d\tilde{T}_e}{d\xi} + \tilde{\beta} \frac{\tilde{\rho}_e\tilde{u}_e}{\tilde{\rho}\tilde{c}_p} \frac{d\tilde{u}_e}{d\xi}, \quad \alpha = \frac{\tilde{u}_e^2}{\tilde{c}_p\tilde{T}_e} \quad (2.13)$$

The boundary conditions (1.17) associated to the equations (2.6), (2.7), (2.8) are

$$\eta = 0 : f = g = 0, \quad \frac{\partial \theta}{\partial \eta} = 0. \quad (2.14)$$

$$\eta \rightarrow \infty : f \rightarrow 1, \quad \theta \rightarrow 1, \quad \tilde{u}_e(\xi) = \tilde{u}_\infty \sqrt{1 - 2\zeta\xi}. \quad (2.15)$$

The boundary layer equations (2.6), (2.7), (2.8) were implemented using the well known modified box scheme (MBS). The calculations were initiated at $\xi = 0$ where the continuity equation (2.6) and the equation of motion (2.7) can be solved independently of the energy equation (2.8) and we obtain a Blasius-type problem. Having the solution for $f(0, \eta)$, $g(0, \eta)$ and $\theta(0, \eta)$ we march forward in the flow direction until the the end of the plate is reached or until the calculations fail to converge due to the formation of a separation singularity. The cases we want to examine are linearly retarded and linearly accelerating supersonic and subsonic flows for the regular fluid Nitrogen and the two BZT fluids PP11 and FC-71.

2.2 Linearly retarded supersonic boundary layer flow

Three different sets of free stream conditions denoted by C1, C2 and C3 where chosen to explore the flow behaviour of N₂, FC71 and PP11 in the general neighbourhood of the thermodynamic critical point. The free stream temperature \tilde{T}_∞ ,

the velocity gradient ζ and the free stream Mach number M_∞ were kept constant at $1.001\tilde{T}_c$, 1.0 and 2.0 in all three cases while the values v_∞ of the specific volume imposed in the conditions C1, C2 and C3 were $v_\infty = 100v_c$, $v_\infty = 5.009v_c$ and $v_\infty = 0.9v_c$, respectively. This is visualised in the pv -diagrams Fig. 3, Fig. 4 and Fig. 5 where the thermodynamic state of the oncoming flow and at the point of separation is marked. Further, it should be noted that the speeds of sound for

	N ₂	PP11	FC-71
C1: \tilde{u}_∞ [m/s]	$4.5 \cdot 10^2$	$1.8 \cdot 10^2$	$1.5 \cdot 10^2$
C1: α_∞	1.5	0.040	0.027
C2: \tilde{u}_∞ [m/s]	$4.0 \cdot 10^2$	$1.4 \cdot 10^2$	$1.1 \cdot 10^2$
C2: α_∞	0.72	0.023	0.015
C3: \tilde{u}_∞ [m/s]	$3.1 \cdot 10^2$	45	40
C3: α_∞	$2.9 \cdot 10^{-3}$	$1.8 \cdot 10^{-4}$	$2.1 \cdot 10^{-4}$

Table 1: Free stream velocity \tilde{u}_∞ and Eckert number α_∞ .

the BZT fluids FC71 and PP11 are significantly smaller than the speed of sound in N₂, [11]. This in turn results in much smaller free stream velocities for a given value of M_∞ . Since the relative importance of the dissipation term in the energy equation (2.8) is determined by the value of the local Eckert number α which is proportional to \tilde{u}_e^2 we, therefore, expect considerably larger temperature variations across the boundary layer for N₂ than for FC71 and PP11 as will be confirmed numerically. Table 1 shows values of the free stream velocity \tilde{u}_∞ and the free stream local Eckert number, i.e. the Eckert number, which characterises the order of magnitude of α throughout the whole flow field Fig. 6, Fig. 7, Fig. 8.

The non-dimensional transverse coordinate appearing in the just mentioned figures and later on is derived from the relation (2.5)

$$\tilde{y} \sqrt{\frac{\tilde{u}_\infty}{\tilde{\nu}_\infty \tilde{x}}} = \frac{\tilde{u}_\infty \tilde{\rho}_\infty}{\tilde{u}_e} \sqrt{2 \frac{\xi \tilde{L}}{\tilde{x}}} \int_0^\eta \tilde{\rho}^{-1} d\eta \quad (2.16)$$

where the integral has to be evaluated numerically and

$$\sqrt{2 \frac{\xi \tilde{L}}{\tilde{x}}} = \sqrt{2}, \quad \text{as } \xi \rightarrow 0 \quad (2.17)$$

which is obtained from the expression (2.4).

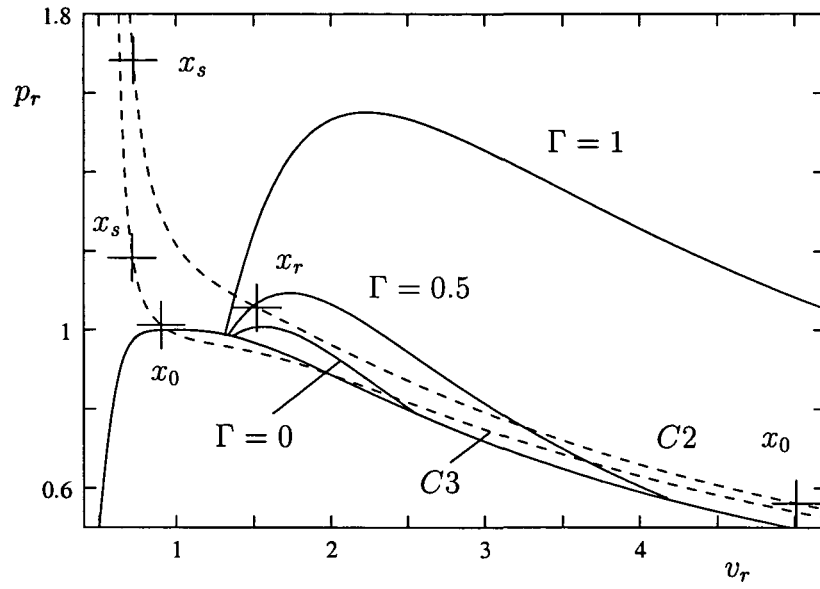


Figure 3: Thermodynamic state at the outer edge of the boundary layer for FC-71. The isentropes with start and end state for the cases C2 and C3 are represented by the dashed lines.

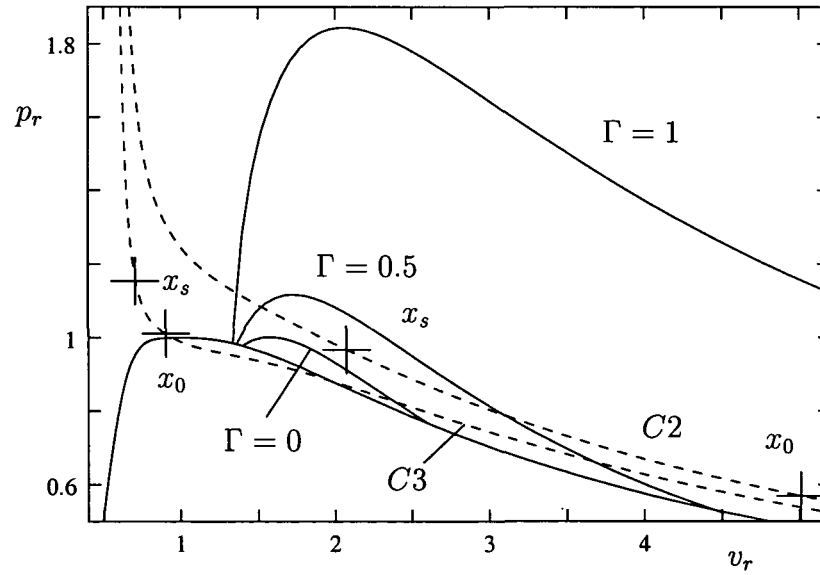


Figure 4: Thermodynamic state at the outer edge of the boundary layer for PP11. The isentropes with start and end state for the cases C2 and C3 are represented by the dashed lines.

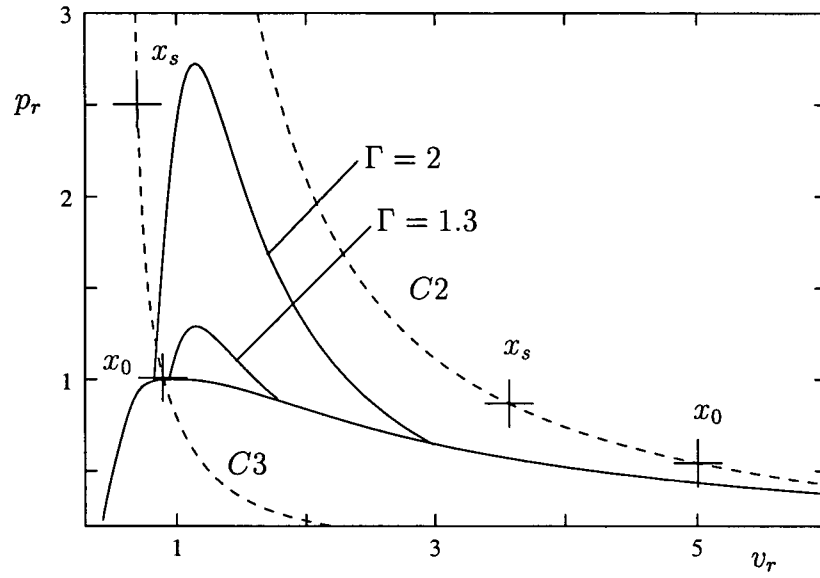


Figure 5: Thermodynamic state at the outer edge of the boundary layer for N_2 . The isentropes with start and end state for the cases C2 and C3 are represented by the dashed lines.

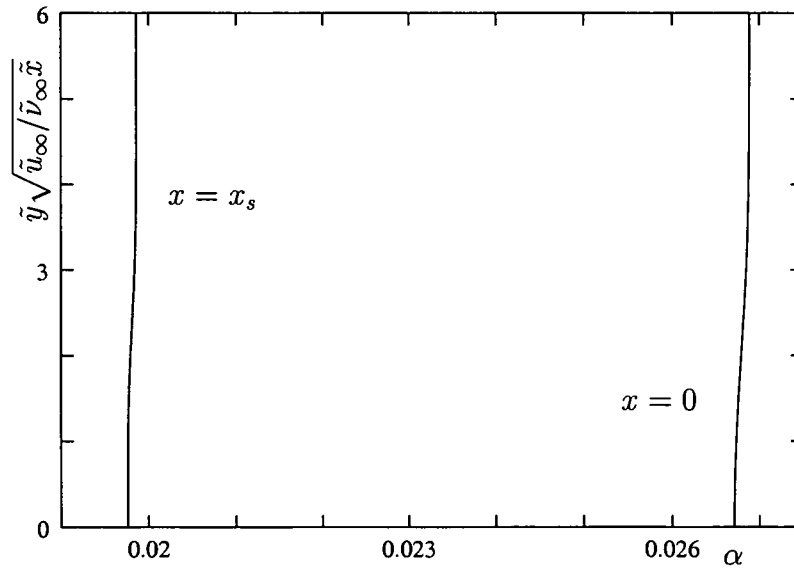


Figure 6: Variations of the local Eckert number across the boundary layer at the leading edge of the plate $x = 0$ and at the point of separation x_s : FC-71, case C1.

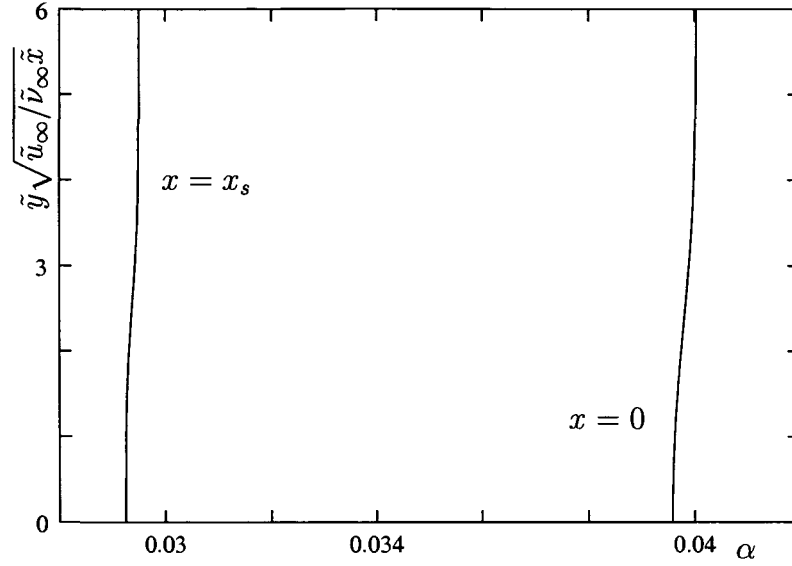


Figure 7: Variations of the local Eckert number across the boundary layer at the leading edge of the plate $x = 0$ and at the point of separation x_s : PP11, case C1.

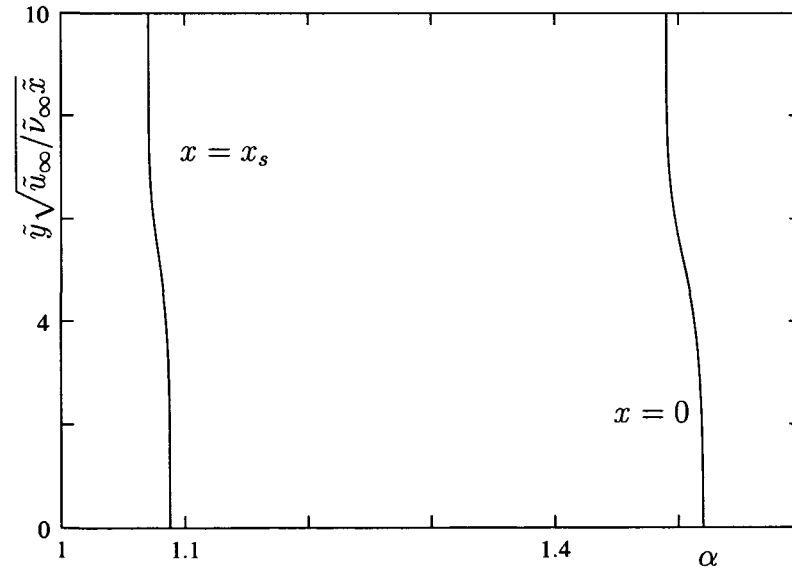


Figure 8: Variations of the local Eckert number across the boundary layer at the leading edge of the plate $x = 0$ and at the point of separation x_s : N_2 , case C1.

Starting out with the case C1, Figure 9 describes the velocity distributions across the boundary layer at the leading edge of the plate $x = 0$. There is no difference to be seen between FC-71, PP11 and the Blasius similarity solution

whereas Nitrogen has a smaller velocity gradient across the boundary layer. Fig. 10, Fig. 11 and Fig. 12 display the temperature variation across the boundary layer. The temperature is almost constant for the BZT fluids in comparison to N_2 and because of the fact that pressure gradient is zero across the boundary layer we also obtain small changes in density for FC-71 and PP11 (Fig. 14, Fig. 15, Fig. 16) while the changes in density at the edge of the boundary layer is of the order 1, Fig. 13. The change of entropy (Fig. 17, Fig. 18, Fig. 19) follows the same pattern -small changes for FC-71, small but little larger ones for PP11 and substantially larger ones for Nitrogen. The friction coefficient c_f defined as

$$c_f = \frac{2\tilde{\mu}_w}{\tilde{\rho}_\infty \tilde{u}_\infty^2} \left. \frac{\partial \tilde{u}}{\partial \tilde{y}} \right|_w, \quad (2.18)$$

is plotted in Figure 20. The larger influence of dissipation in Nitrogen, due to the larger value of the Eckert number (Table 1), causes N_2 to reach the point of separation faster than the two dense gases. This effect is also to be seen in Figure 21 where the displacement thickness

$$\tilde{\delta}_1 = \int_0^{\tilde{y} \rightarrow \infty} \left(1 - \frac{\tilde{\rho} \tilde{u}}{\tilde{\rho}_e \tilde{u}_e} \right) d\tilde{y}, \quad (2.19)$$

has been plotted for PP11, FC-71 and N_2 together with the Blasius solution.

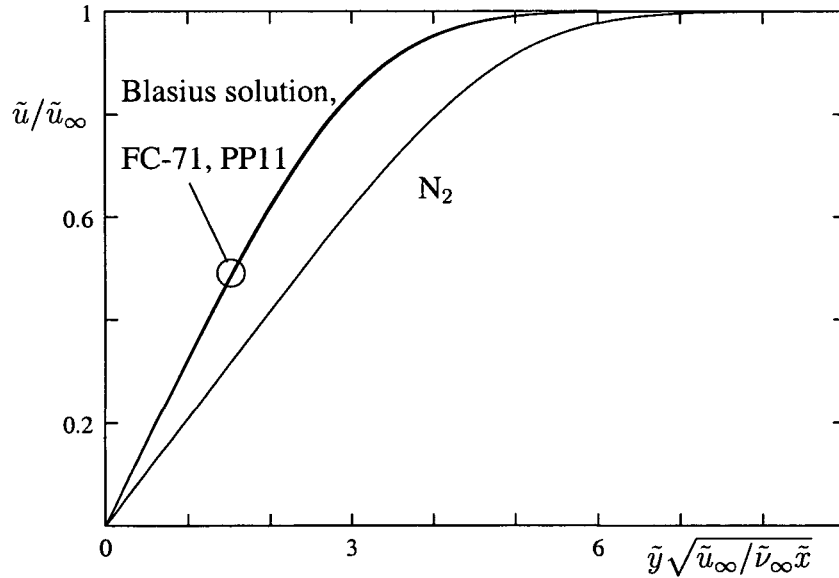


Figure 9: Velocity distributions at the leading edge of the plate $x = 0$: Blasius similarity solution, FC-71, PP11, N_2 , case C1.

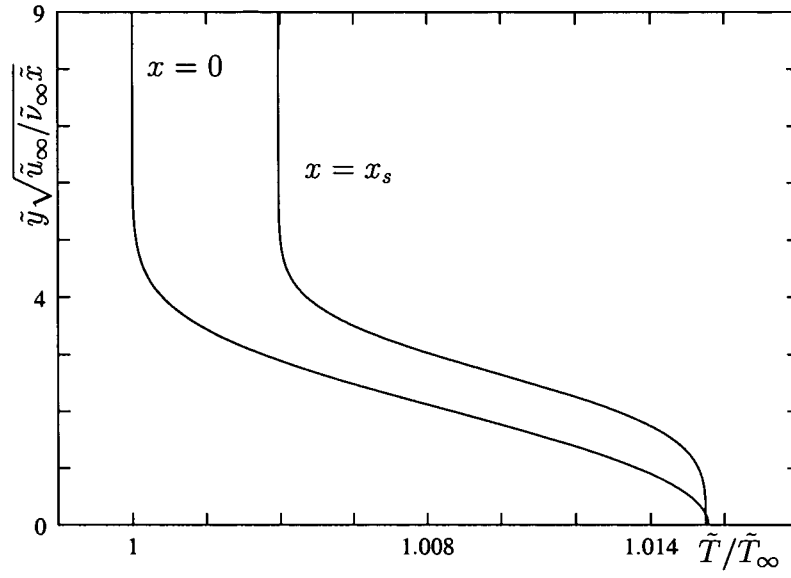


Figure 10: Temperature variation across the boundary layer at the leading edge of the plate $x = 0$ and at the point of separation x_s : FC-71, case C1.

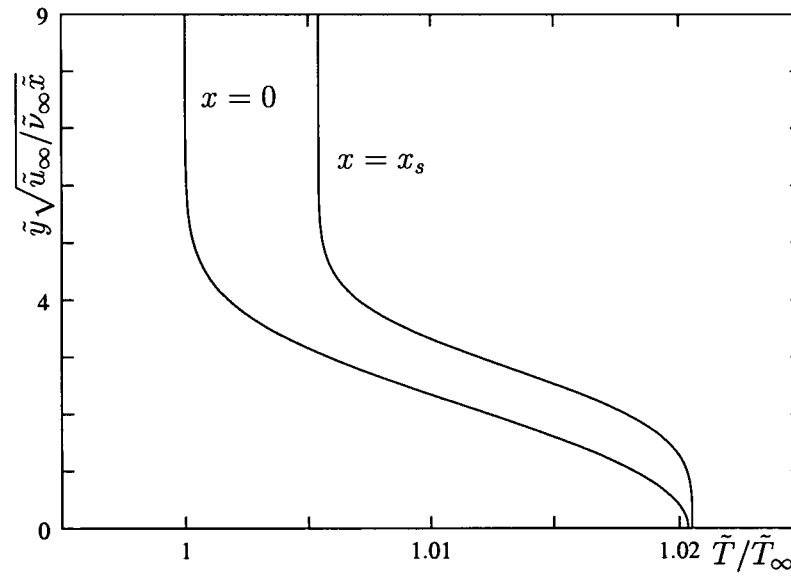


Figure 11: Temperature variation across the boundary layer at the leading edge of the plate $x = 0$ and at the point of separation x_s : PP11, case C1.

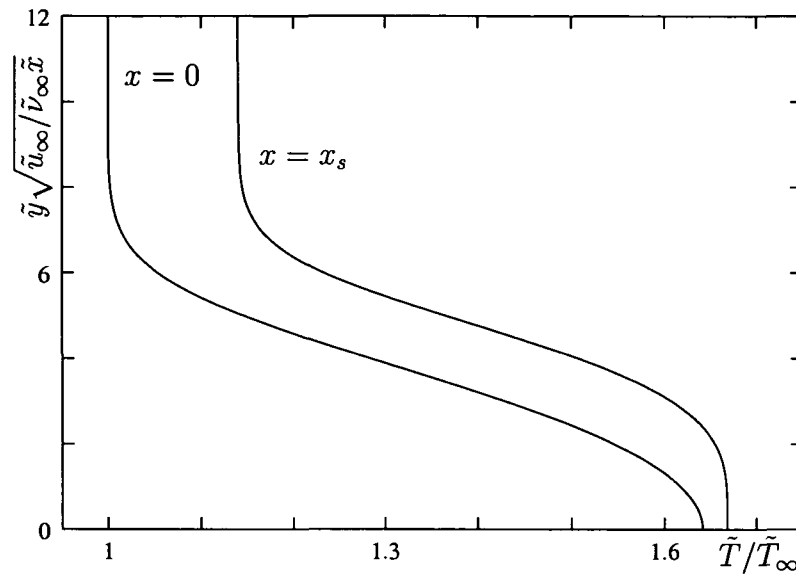


Figure 12: Temperature variation across the boundary layer at the leading edge of the plate $x = 0$ and at the point of separation x_s : N_2 , case C1.

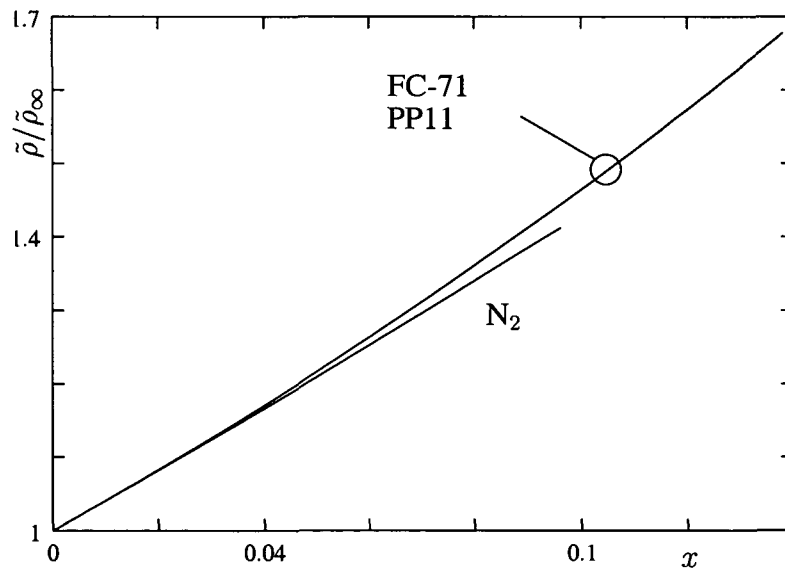


Figure 13: Density variation at the edge of the boundary layer: case C1.

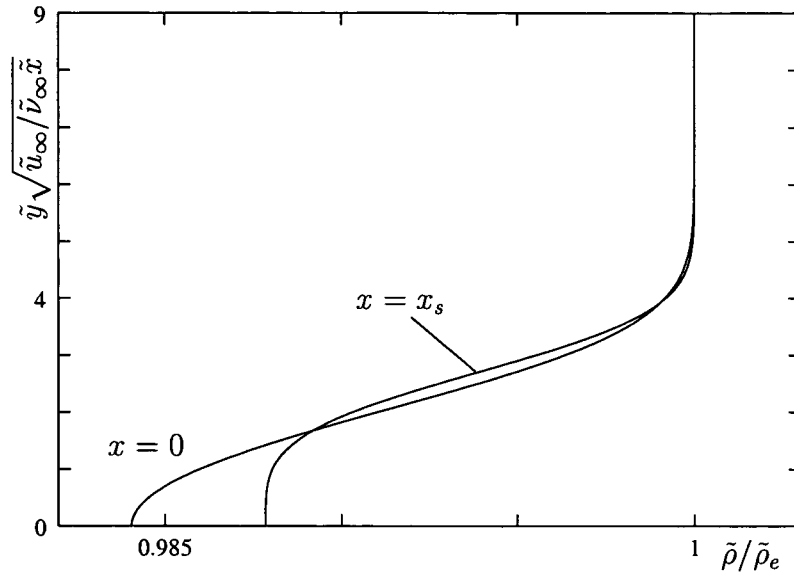


Figure 14: Density variation across the boundary layer at the leading edge of the plate $x = 0$ and at the point of separation x_s : FC-71, case C1.

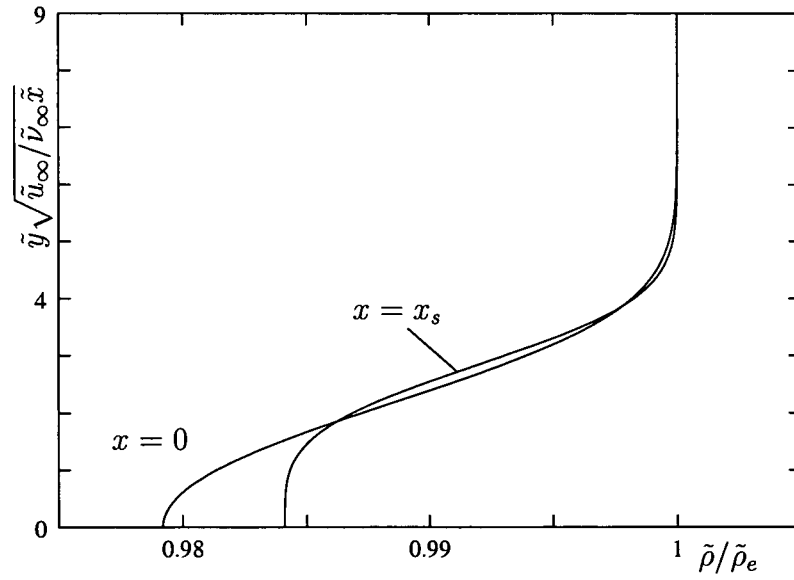


Figure 15: Density variation across the boundary layer at the leading edge of the plate $x = 0$ and at the point of separation x_s : PP11, case C1.

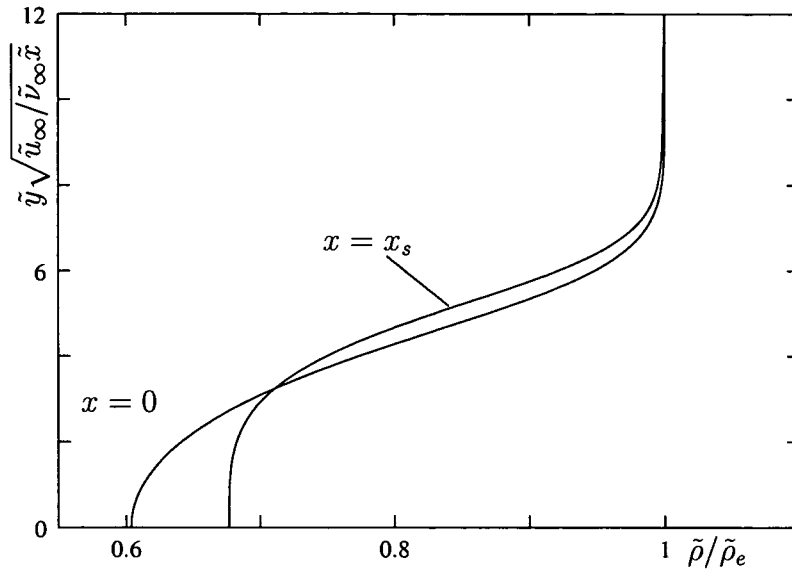


Figure 16: Density variation across the boundary layer at the leading edge of the plate $x = 0$ and at the point of separation x_s : N_2 , case C1.

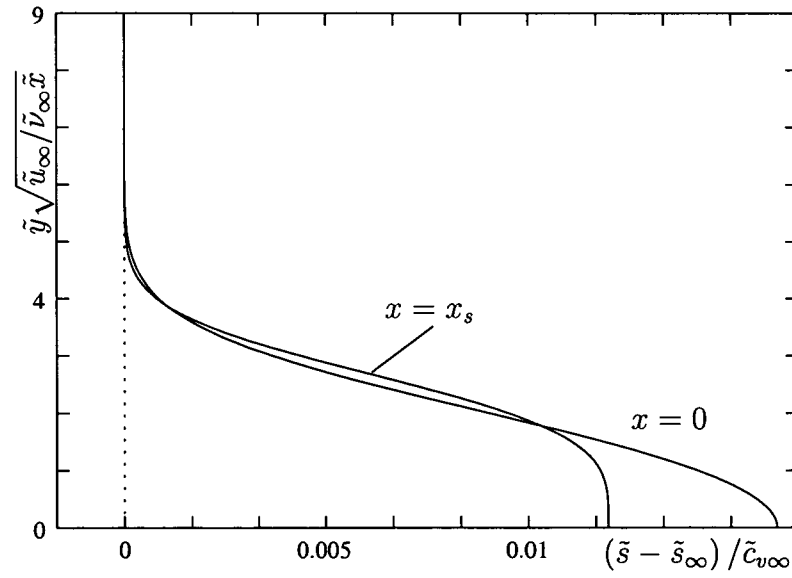


Figure 17: Change in entropy across the boundary layer at the leading edge of the plate $x = 0$ and at the point of separation x_s : FC-71, case C1.

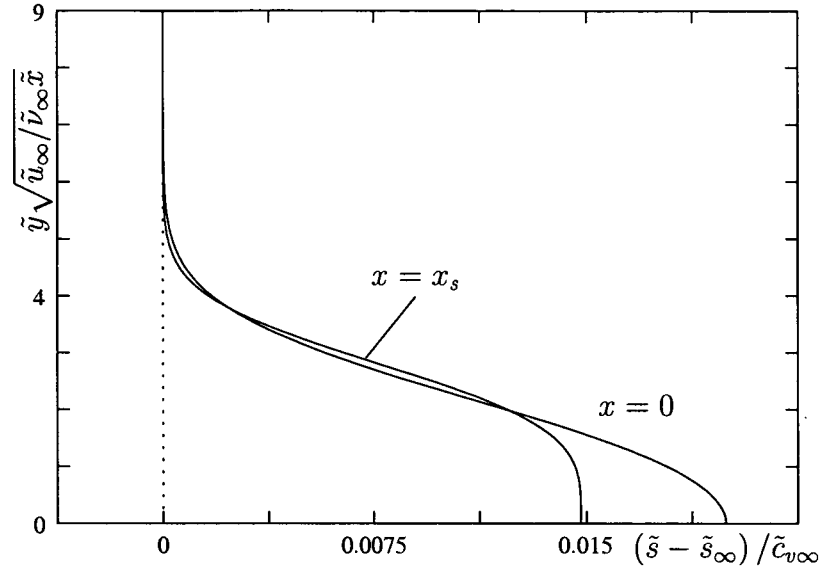


Figure 18: Change in entropy across the boundary layer at the leading edge of the plate $x = 0$ and at the point of separation x_s : PP11, case C1.

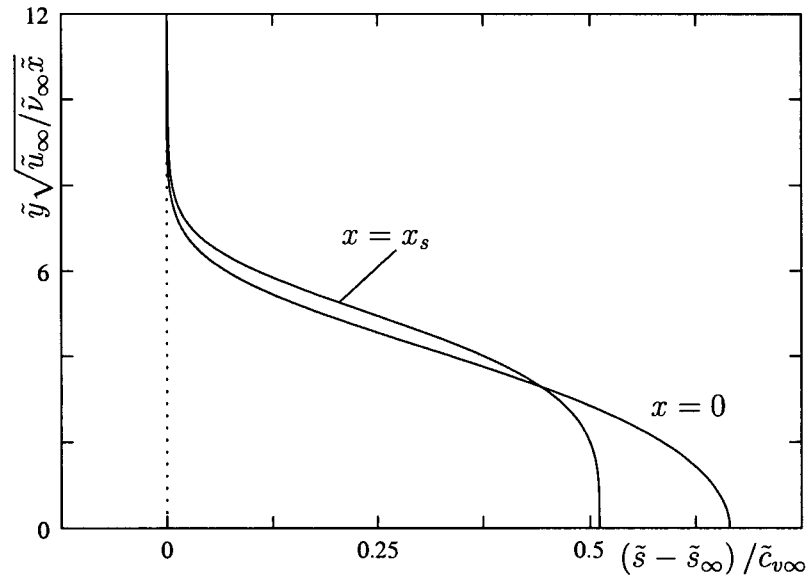


Figure 19: Change in entropy across the boundary layer at the leading edge of the plate $x = 0$ and at the point of separation x_s : N_2 , case C1.

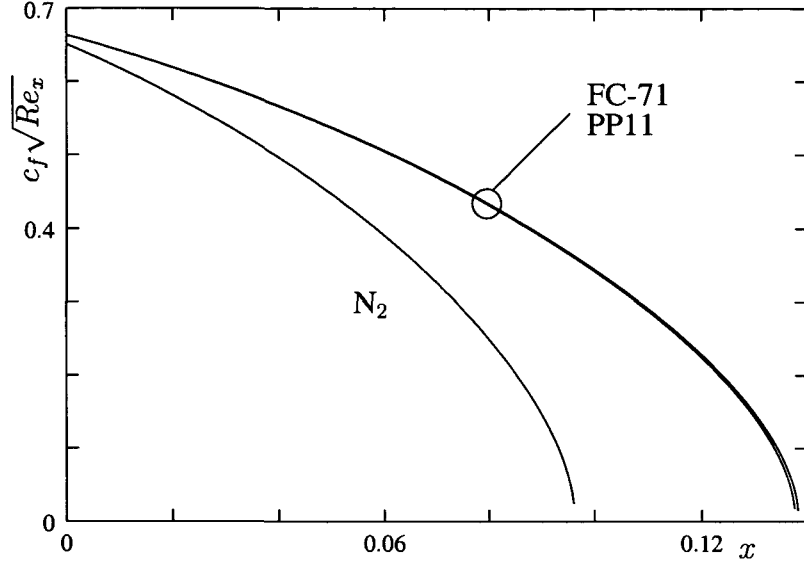


Figure 20: Distributions of the friction coefficient: case C1.

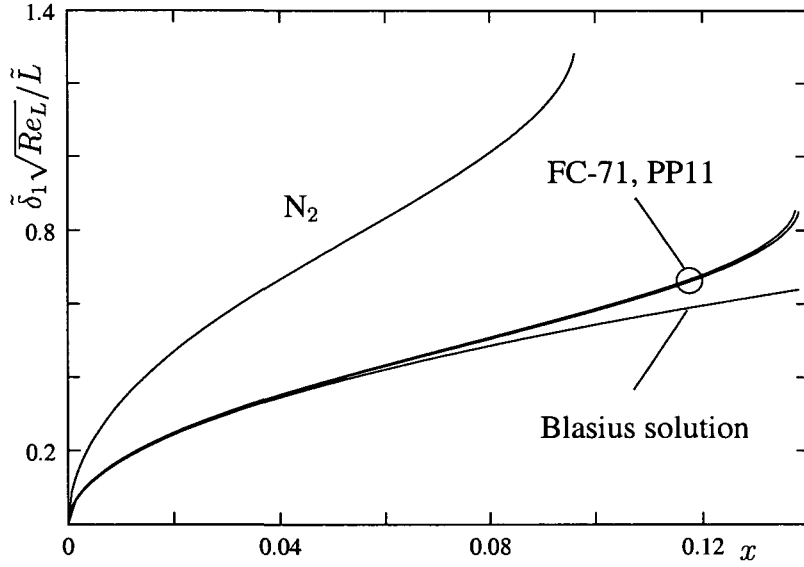


Figure 21: Distributions of the displacement thickness: case C1.

We now turn to next case, C2. The value of free stream velocity u_∞ is about four times larger for N_2 than for FC-71 and PP11, Table 1. The free stream value of the Eckert number α_∞ is of the order one and 10^{-2} for Nitrogen and the BZT fluids, respectively. This means that the dissipation is significantly smaller for the dense gases than for N_2 . Consequently, the distributions of velocity at the leading

edge (Fig. 22) for FC-71 and PP11 again closely resemble to the Blasius similarity solution whereas the velocity gradient for Nitrogen is smaller. The temperature variations across the boundary layer are of the order Eckert number for N_2 and the BZT-fluids, Fig. 23, Fig. 24, Fig. 25. The changes in density at the boundary layer edge are for all three substances of the order one, Fig. 26, and so are the variations across the boundary layer for N_2 , Fig. 29, whereas the changes are small for both FC-71, Fig. 27 and PP11, Fig. 28. The entropy depending on temperature and density behaves in a similar manner where FC-71 experiences the smallest variations, Fig. 30, PP11 small but somewhat larger, Fig. 31, and N_2 exhibits changes of the order one, Fig. 32. For N_2 and PP11, the adverse pressure gradient associated with the retarded external flow causes the formation of a Goldstein singularity where the calculations terminate, Fig. 33. For the BZT-fluid FC-71, however, the friction factor decreases initially but this tendency comes to a halt and the wall shear stress starts to increase despite the fact that the pressure gradient is still positive.

Evaluation of the continuity equation (1.1) outside the boundary layer

$$\frac{\partial \tilde{v}}{\partial \tilde{y}} = (M_e^2 - 1) \frac{\partial \tilde{u}_e}{\partial \tilde{x}}, \quad (2.20)$$

predicts that the normal velocity component \tilde{v} in a decelerating supersonic flow decreases with increasing distance to the wall and this effect becomes more pronounced as the Mach number increases. Owing to the fact that the density changes across the boundary layer are small for PP11 and FC71 this is true also for most of the supersonic outer part of the boundary layer. For sufficiently large values of $M_e(x)$ one, therefore, expects that the displacement body $\delta_1(x)$ (Fig. 34) may shrink rather than expand and this is confirmed by the numerical calculations which show that $M_e(x)$ initially increases with x (Fig. 36). The associated momentum influx into the boundary layer is then able to overcome the onset of separation and causes the wall shear stress to rise sharply, Figure 33. Eventually, however, the Mach number starts to drop, which in turn quenches this effect. This unusual behaviour, an increasing Mach number in a decelerating supersonic flow, which is the mechanism for the type of marginal separation appearing here, can occur only if the condition

$$1 - \Gamma - M^{-2} > 0, \quad (2.21)$$

is satisfied, [9]. This obviously requires $\Gamma < 1$ which is possible for BZT-fluids where Γ can assume even negative values as can be seen in the pressure-specific volume diagram, Fig. 3. In contrast Γ is a strictly positive quantity larger than one for the regular fluid Nitrogen and the formation of a Goldstein singularity is inevitable. The distribution of the fundamental derivative for case C2 is shown in

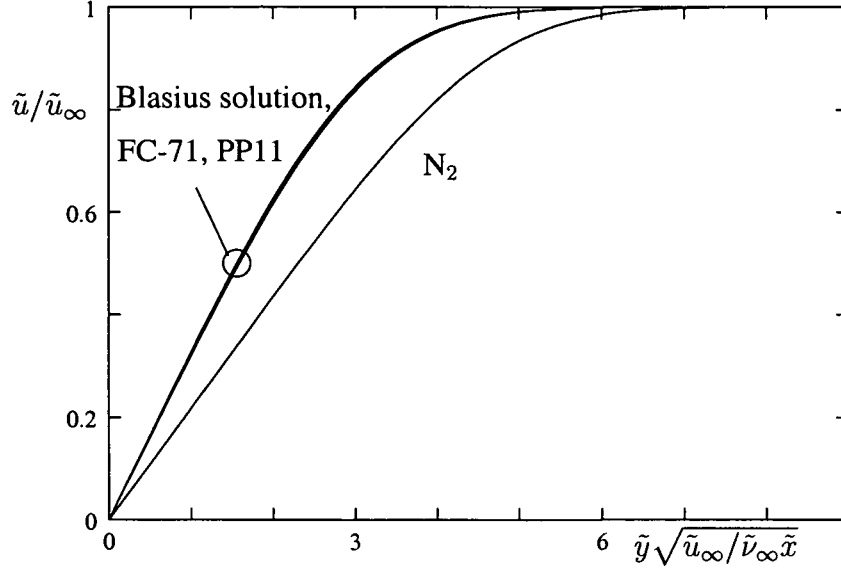


Figure 22: Velocity distributions at the leading edge of the plate $x = 0$: Blasius similarity solution, FC-71, PP11, N_2 , case C2.

Fig. 35. The new type of marginal separation occurring here which is triggered by a non-classical mechanism i.e. the non-monotonous Mach number variation during isentropic compression of a dense gas, is possible for a wide range of different oncoming thermodynamic states for the dense gas FC-71 as displayed in Fig. 37. Above the saturation curve in the general neighbourhood of the critical point, there is a shaded surface. A free stream state within this area exposed to a linearly retarded external velocity ($\zeta = -1$) yields a local minimum of wall shear stress. As the so-called curve of marginal separation is approached this effect becomes more pronounced and the wall shear eventually vanishes in one single point i.e. the flow exhibits a marginal separation singularity having the property that the solution can be continued further downstream. If the free stream temperature is increased further, a Goldstein separation singularity develops upstream of the point of zero skin friction, Fig. 38. For freestream values of specific volume smaller than $2.0v_c$ it was not possible to find a distinctly defined curve of marginal separation due to numerical difficulties.

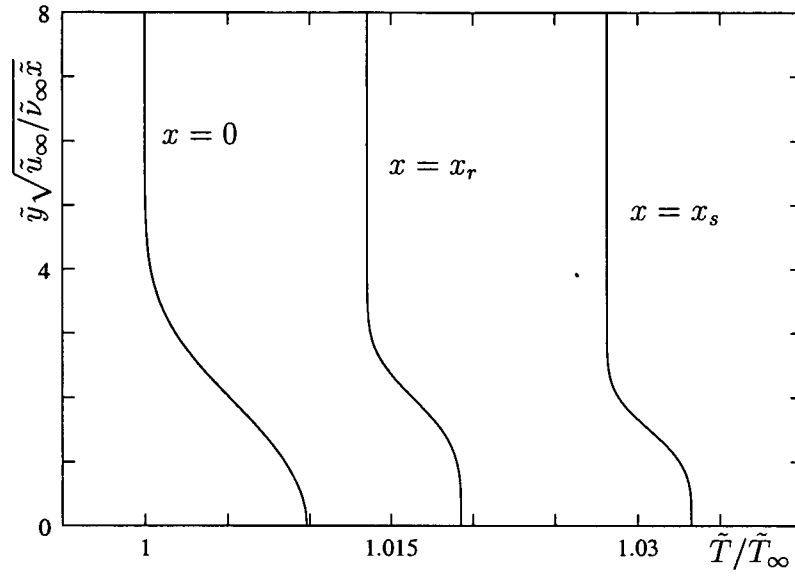


Figure 23: Temperature variation across the boundary layer at the leading edge of the plate $x = 0$, at the point of recovery x_r and at the point of separation x_s : FC-71, case C2.

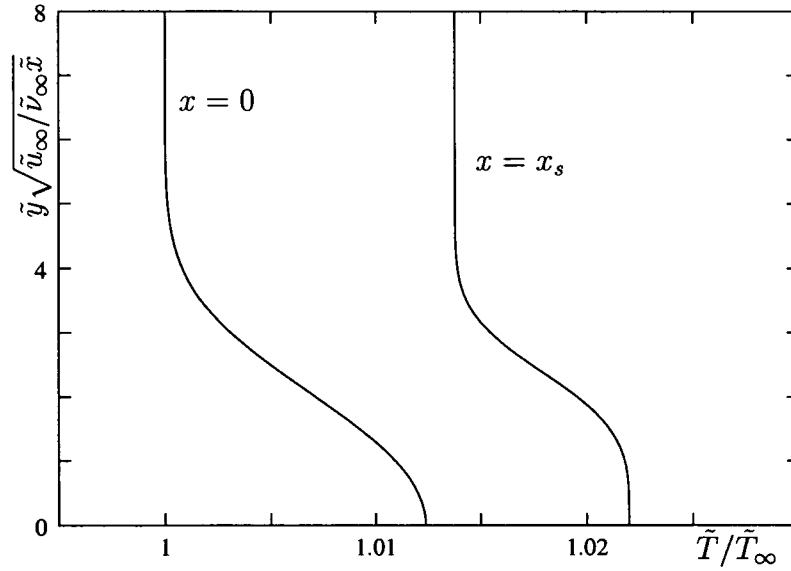


Figure 24: Temperature variation across the boundary layer at the leading edge of the plate $x = 0$ and at the point of separation x_s : PP11, case C2.

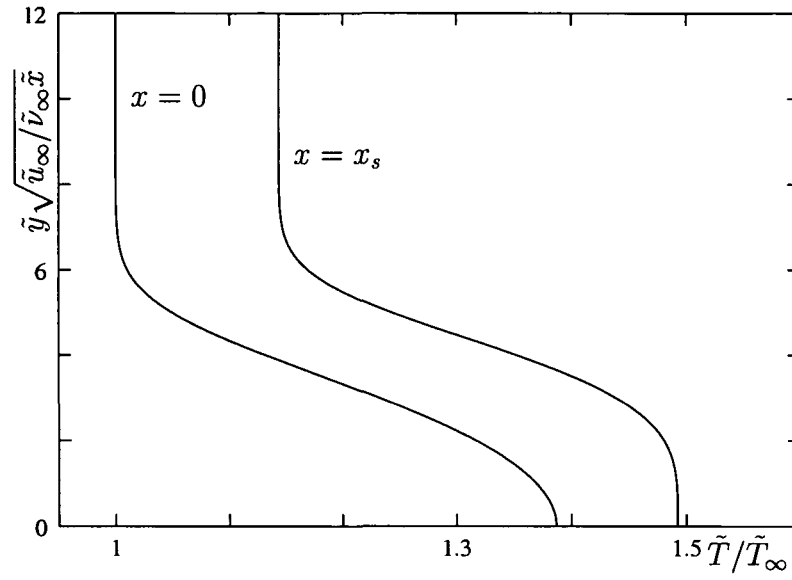


Figure 25: Temperature variation across the boundary layer at the leading edge of the plate $x = 0$ and at the point of separation x_s : N_2 , case C2.

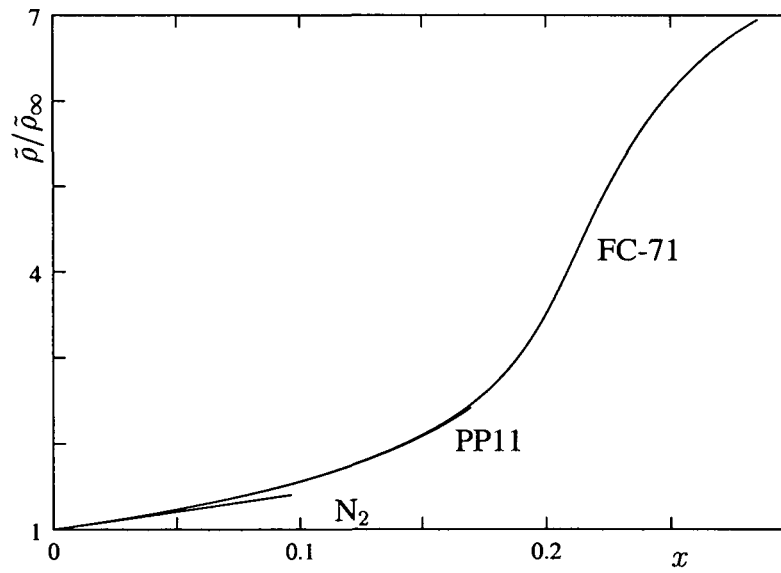


Figure 26: Density variation at the edge of the boundary layer: case C2.

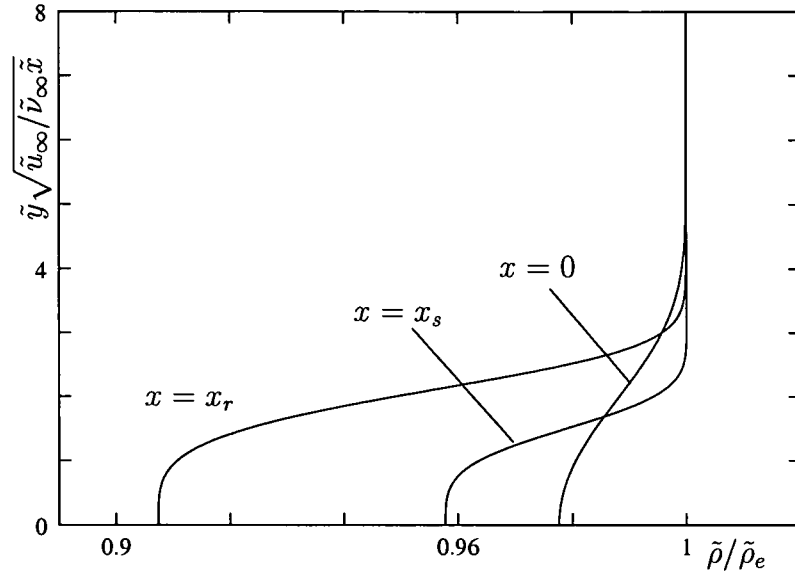


Figure 27: Density variation across the boundary layer at the leading edge of the plate $x = 0$, at the point of recovery x_r , and at the point of separation x_s : FC-71, case C2.

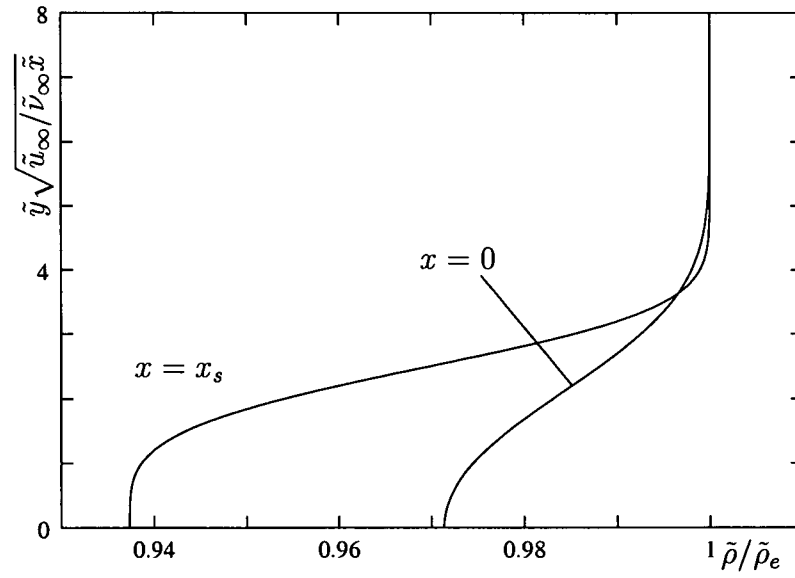


Figure 28: Density variation across the boundary layer at the leading edge of the plate $x = 0$ and at the point of separation x_s : PP11, case C2.

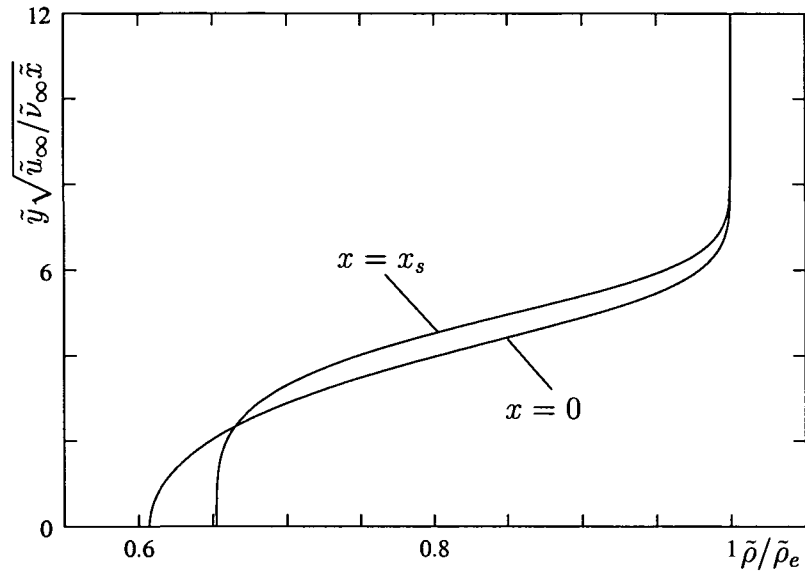


Figure 29: Density variation across the boundary layer at the leading edge of the plate $x = 0$ and at the point of separation x_s : N_2 , case C2.

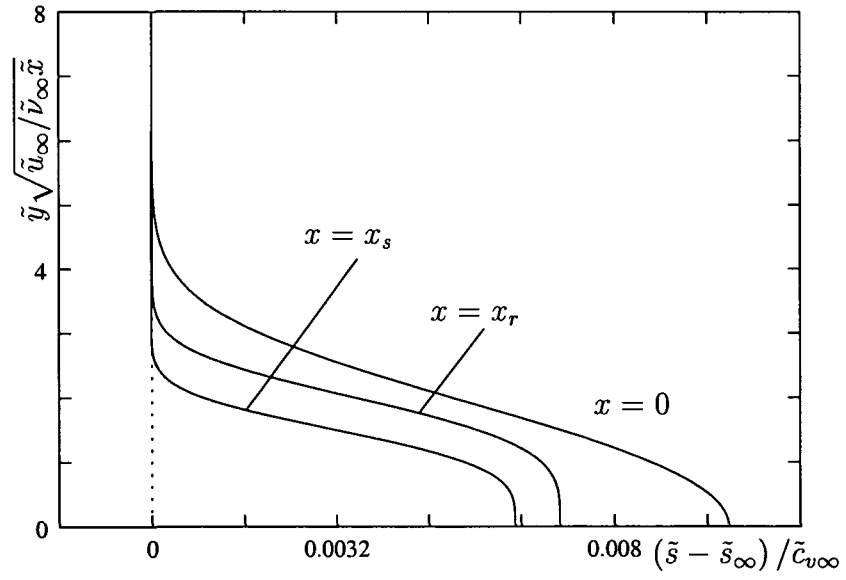


Figure 30: Change in entropy across the boundary layer at the leading edge of the plate $x = 0$, at the point of recovery x_r , and at the point of separation x_s : FC-71, case C2.

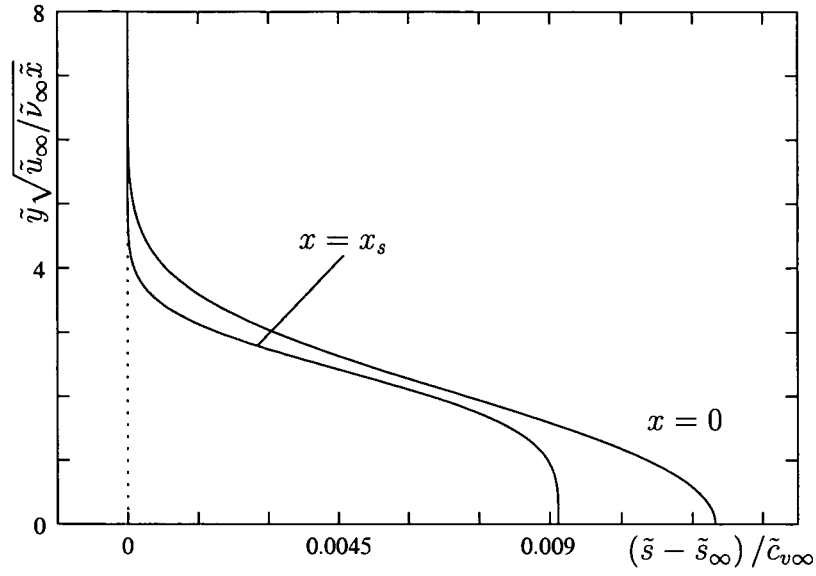


Figure 31: Change in entropy across the boundary layer at the leading edge of the plate $x = 0$ and at the point of separation x_s : PP11, case C2.

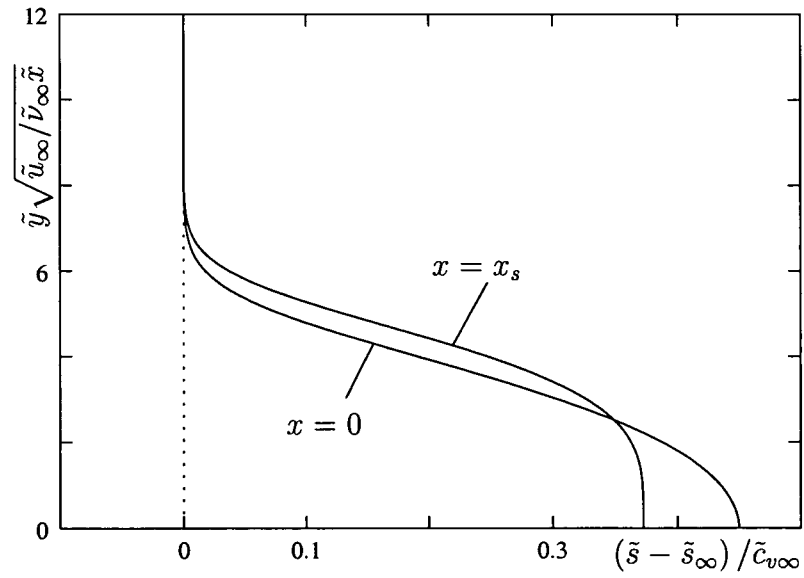


Figure 32: Change in entropy across the boundary layer at the leading edge of the plate $x = 0$ and at the point of separation x_s : N_2 , case C2.

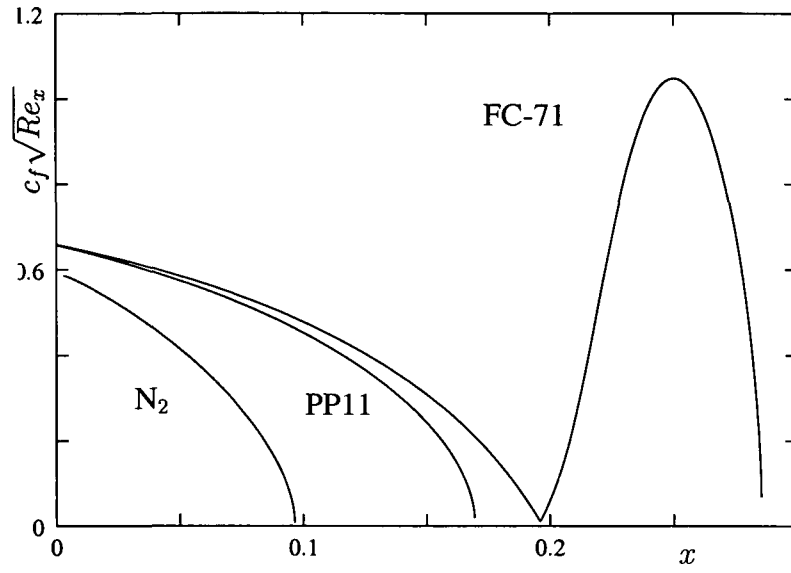


Figure 33: Distributions of the friction coefficient: case C2.

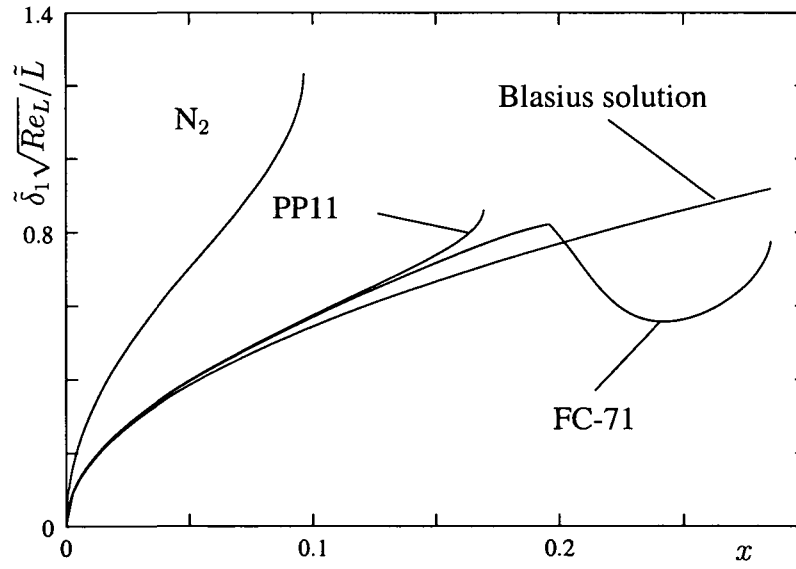


Figure 34: Distributions of the displacement thickness: case C2.

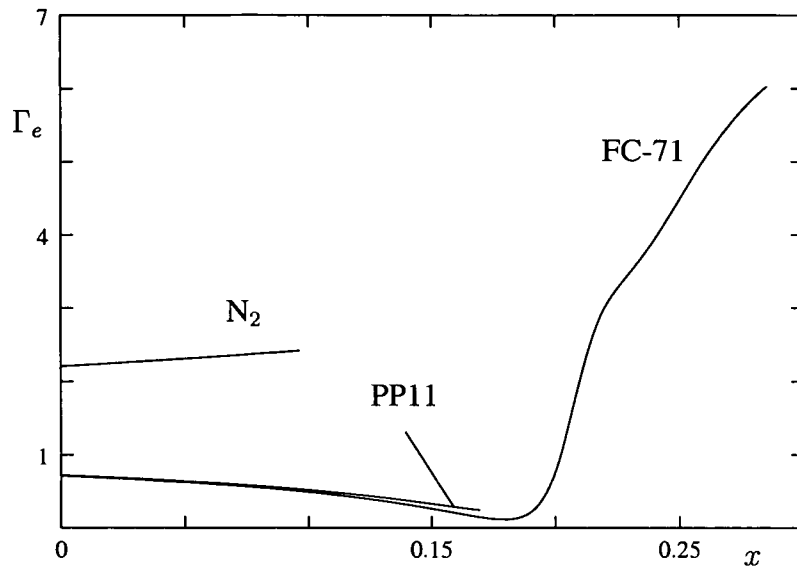


Figure 35: Distributions of the fundamental derivative at the boundary layer edge: case C2.

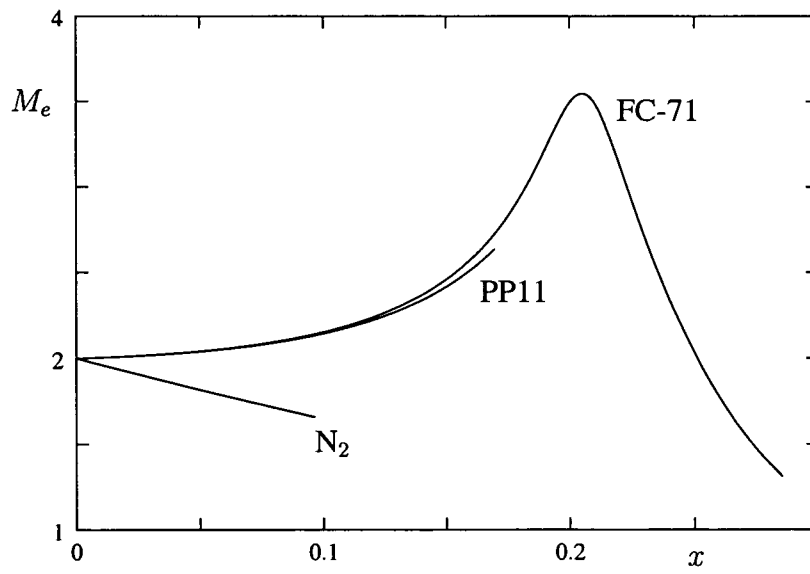


Figure 36: Mach number distribution at the boundary layer edge: case C2.

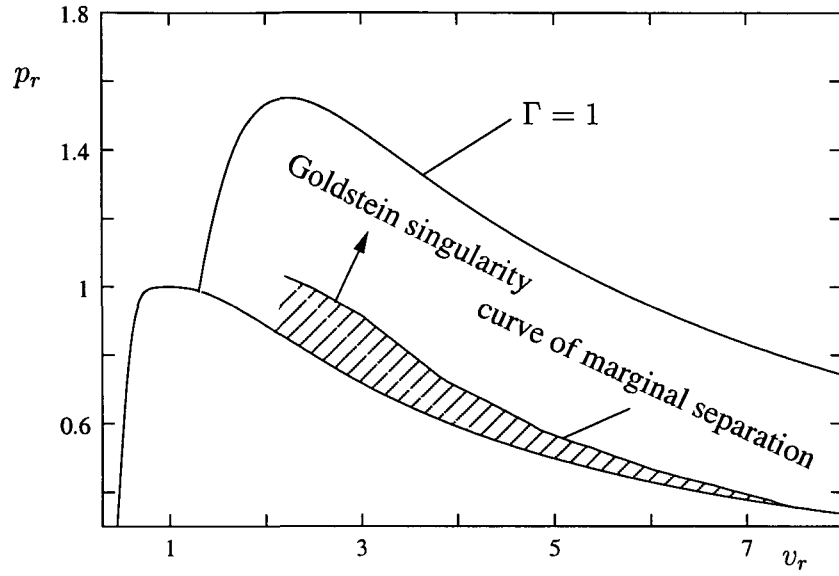


Figure 37: pv -diagram for FC-71. Upstream states within the shaded area lead to wall shear stress distributions with a pronounced minimum while states outside this domain exhibit a Goldstein separation singularity in linearly retarded flows with $M_\infty = 2.0$, $\zeta = -1$.

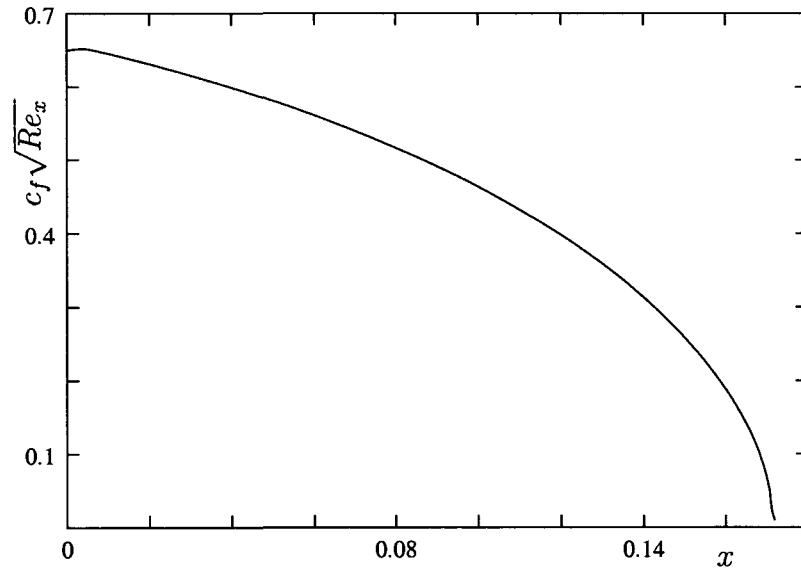


Figure 38: Friction coefficient for FC-71 at $\tilde{T}_\infty = 1.001\tilde{T}_c$, $\tilde{v}_\infty = 5.5\tilde{v}_c$, $M_\infty = 2.0$, i.e. above the curve of marginal separation.

As far as the third case C3 is concerned the behaviour of the flour carbons

FC-71 and PP11 is similar to that observed for initial states C1, i.e. the velocity profiles at the leading edge closely resemble the Blasius similarity solution, Fig. 39. Also, as before in case C1 we obtain small changes in density (Fig.44, Fig.45) and temperature across the boundary layer, Fig.40, Fig.41. For the regular fluid Nitrogen the temperature variations (Fig.42) are comparable with those found in cases C1 and C2 while we have larger variations in density than before, Fig.46. Furthermore, at the tip of the plate both the temperature and density distributions exhibit an unsmooth transition from the viscous to the inviscid part of the boundary layer. This is caused by a singularity of the isobaric heat capacity c_p in the thermodynamic critical point which is past close by due to the large variation in density, Fig. 47. At the boundary layer edge the changes in density are of the order one for all three substances, Fig. 43. The distributions of entropy across the boundary layer are large for N_2 , Fig. 50, and small for the BZT-fluids, Fig. 48, Fig. 49. The friction factor (Fig. 51) is also affected by the small value of density on the wall for Nitrogen and is about half as large as the value of the Blasius similarity solution. Further, the displacement thickness for FC-71, PP11 and N_2 grows faster than the Blasius similarity solution, Fig. 52.

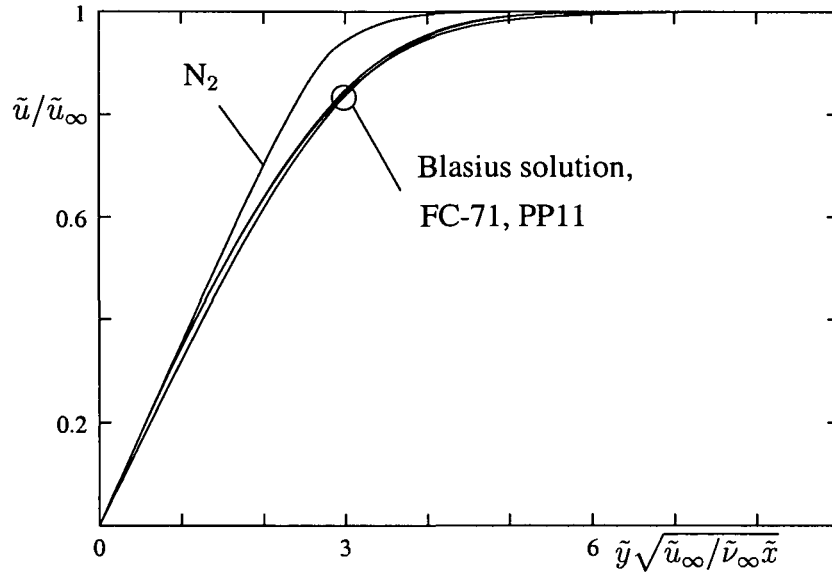


Figure 39: Velocity distributions at the leading edge of the plate $x = 0$: Blasius similarity solution, FC-71, PP11, N_2 , case C3.

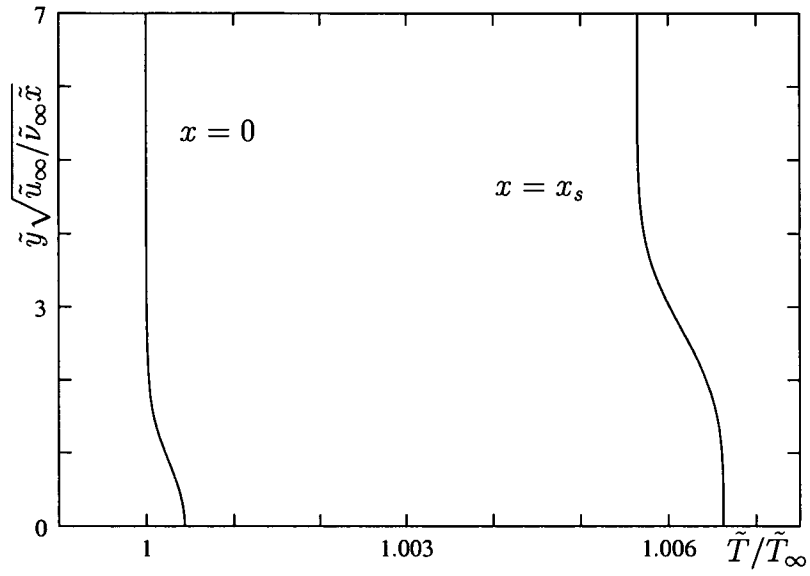


Figure 40: Temperature variation across the boundary layer at the leading edge of the plate $x = 0$ and at the point of separation x_s : FC-71, case C3.

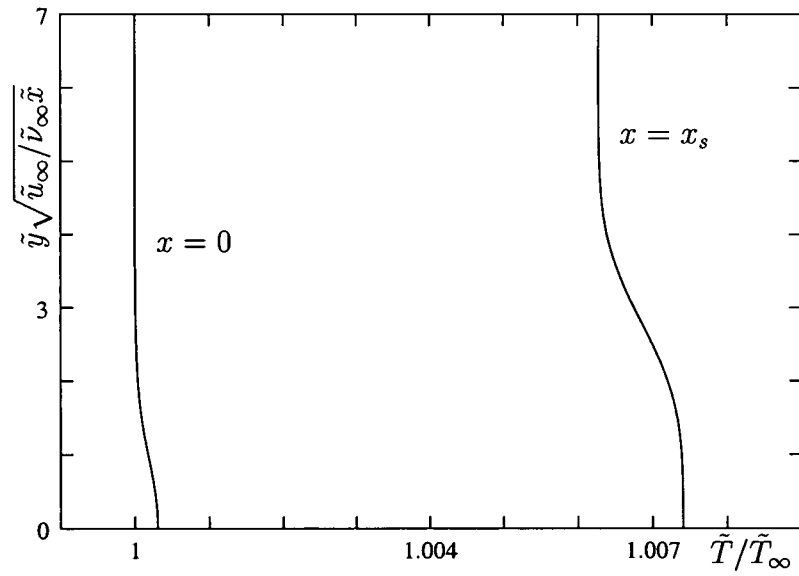


Figure 41: Temperature variation across the boundary layer at the leading edge of the plate $x = 0$ and at the point of separation x_s : PP11, case C3.

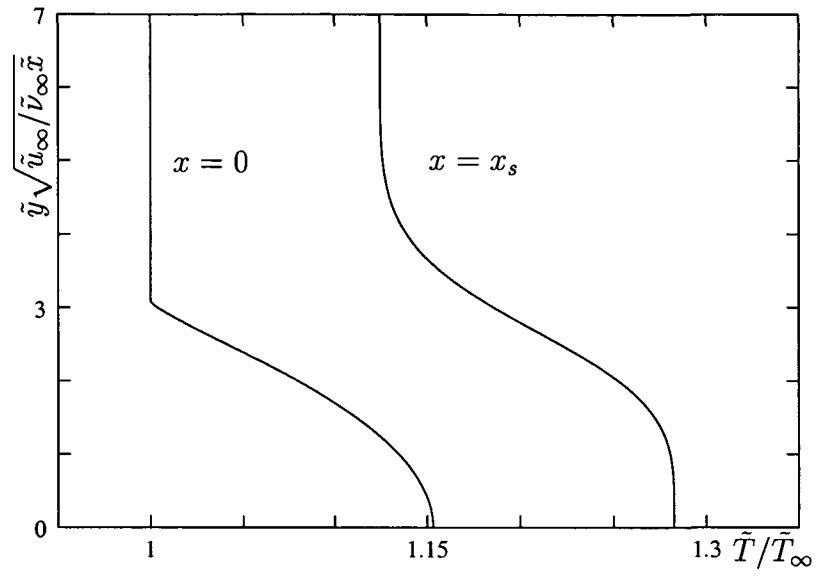


Figure 42: Temperature variation across the boundary layer at the leading edge of the plate $x = 0$ and at the point of separation x_s : N_2 , case C3.

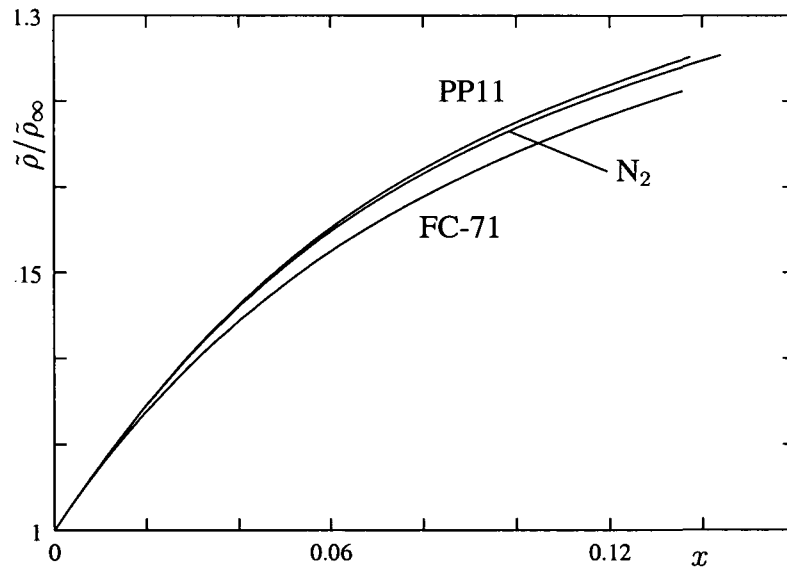


Figure 43: Density variation at the edge of the boundary layer: case C3.

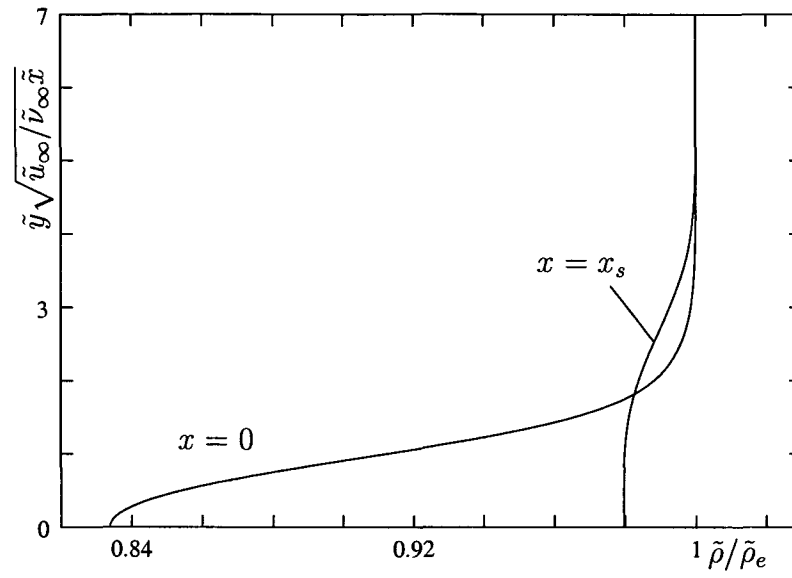


Figure 44: Density variation across the boundary layer at the leading edge of the plate $x = 0$ and at the point of separation x_s : FC-71, case C3.

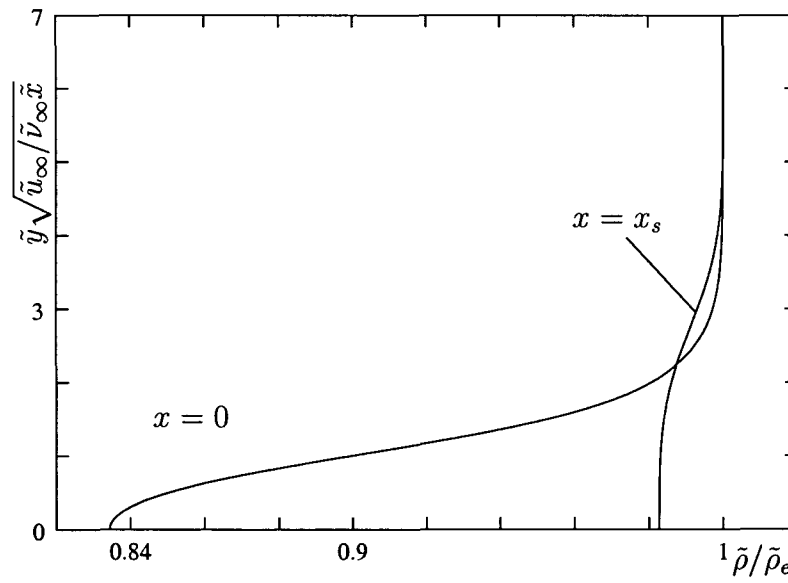


Figure 45: Density variation across the boundary layer at the leading edge of the plate $x = 0$ and at the point of separation x_s : PP11, case C3.

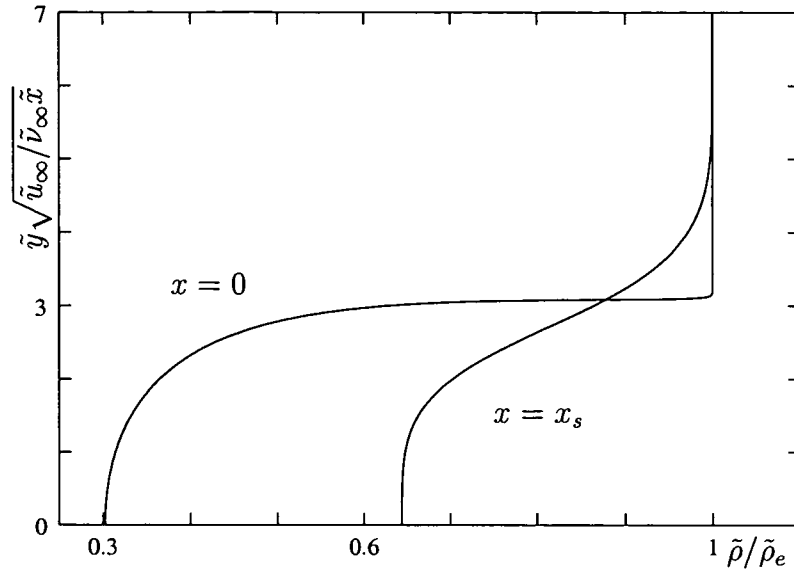


Figure 46: Density variation across the boundary layer at the leading edge of the plate $x = 0$ and at the point of separation x_s : N_2 , case C3.

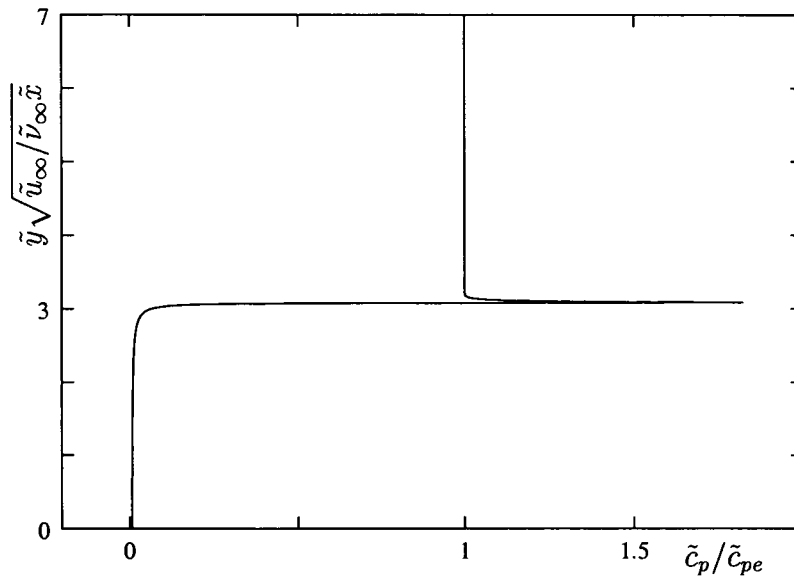


Figure 47: Variations of the isobaric heat capacity across the boundary layer at the leading edge of the plate $x = 0$: N_2 , case C3.

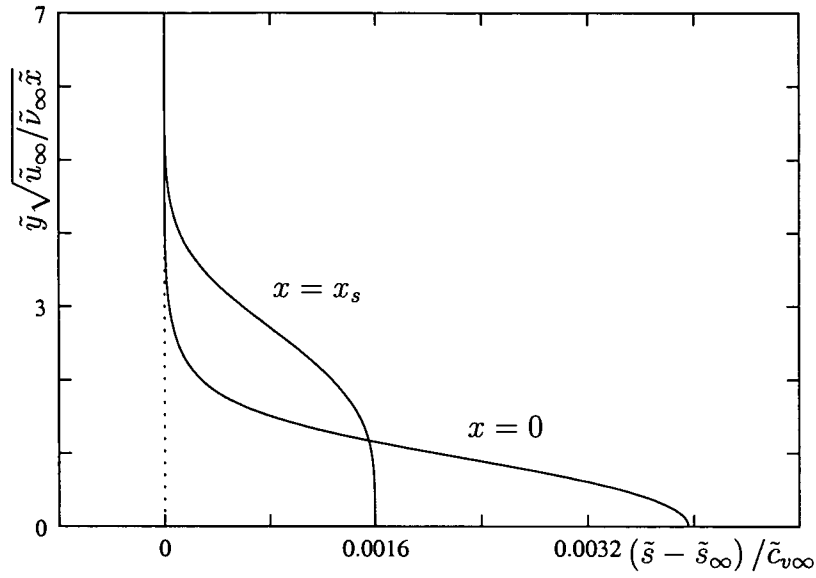


Figure 48: Change in entropy across the boundary layer at the leading edge of the plate $x = 0$ and at the point of separation x_s : FC-71, case C3.

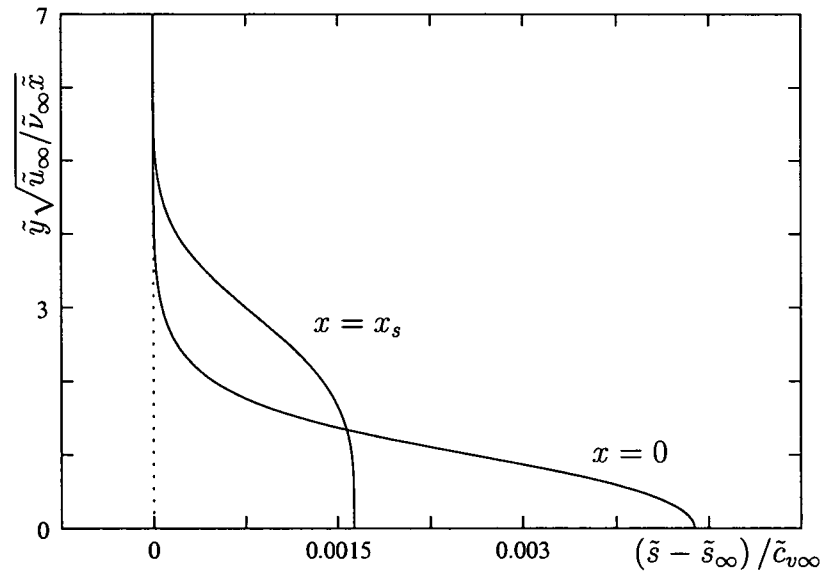


Figure 49: Change in entropy across the boundary layer at the leading edge of the plate $x = 0$ and at the point of separation x_s : PP11, case C3.

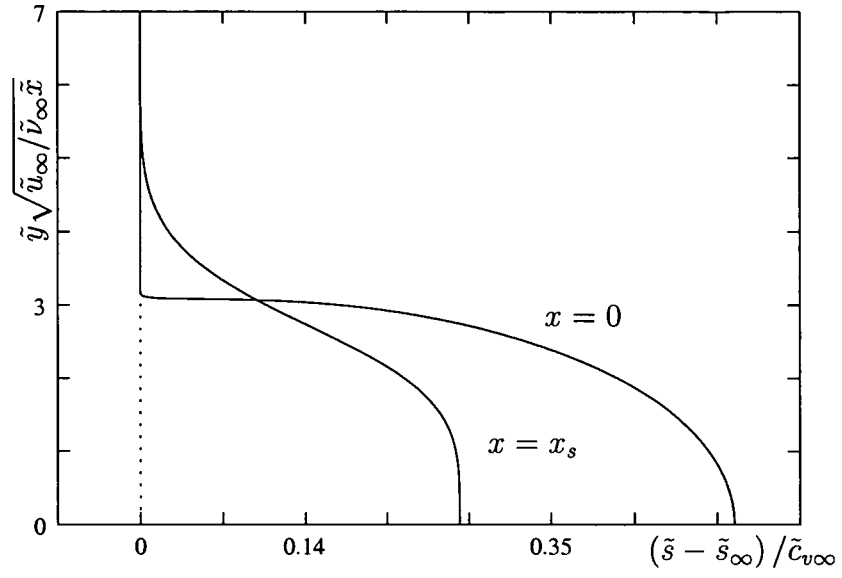


Figure 50: Change in entropy across the boundary layer at the leading edge of the plate $x = 0$ and at the point of separation x_s : N_2 , case C3.

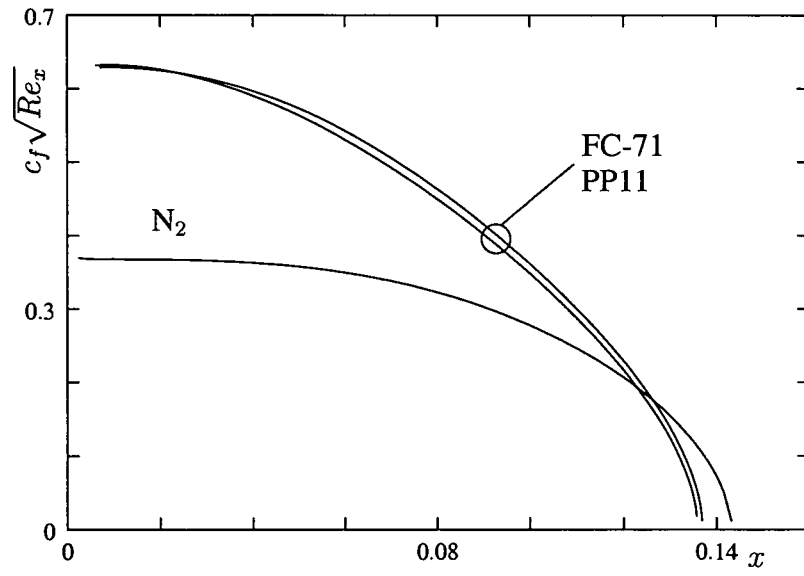


Figure 51: Distributions of the friction coefficient: case C3.

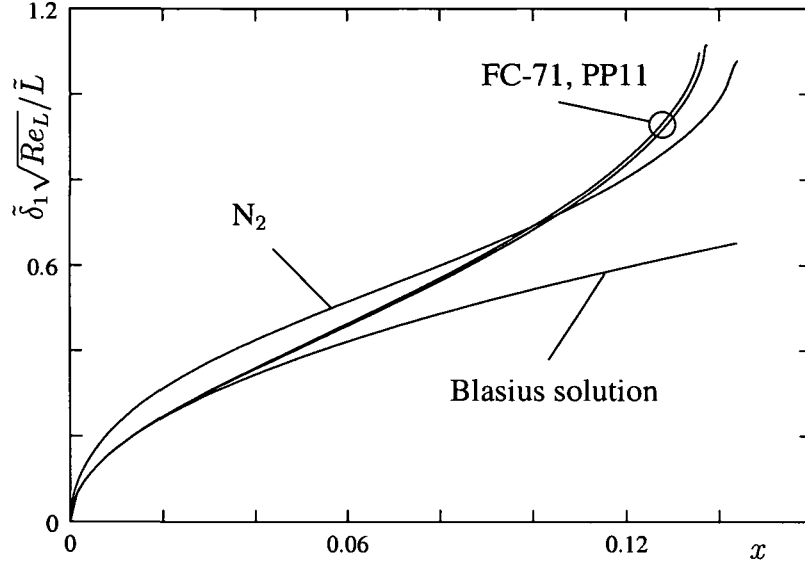


Figure 52: Distributions of the displacement thickness: case C3.

2.3 Linearly accelerating supersonic boundary layer flow

In this section we are considering linearly accelerating supersonic flows where the external velocity is given by

$$u_e = 1 + \zeta x, \quad \zeta = 1.$$

We compare the behaviour of PP11, FC-71 and N_2 at the free stream Mach number $M_\infty = 2.0$, specific volume $\tilde{v}_\infty = 1.05\tilde{v}_c$, temperature $\tilde{T}_\infty = 1.001\tilde{T}_c$ until

	N_2	PP11	FC-71
\tilde{u}_∞ [m/s]	320	52	46
α_∞	0.015	0.0012	0.0013

Table 2: Free stream velocity and Eckert number: $M_\infty = 2.0$, $\tilde{v}_\infty = 1.05\tilde{v}_c$, $\tilde{T}_\infty = 1.001\tilde{T}_c$

the point $x = 0.1$ is reached after which no nonclassical behaviour was observed. The relative importance of the dissipation determined by the local Eckert number α in the energy equation (2.8) is smaller for the dense gases than for Nitrogen and the speed of sound is for FC-71 and PP11 smaller which causes a higher free stream velocity for N_2 , Table 2. At the tip of the plate the velocity distributions of the dense gases are similar to the Blasius similarity solution whereas Nitrogen has

a smaller velocity gradient, Fig. 53. As also seen in the previous section where linearly retarded supersonic boundary layer flows were studied, the changes in temperature are small for the BZT-fluids, Fig. 54, Fig. 55 and so are the density variations across the boundary layer whereas the changes in density on the boundary layer are of the order one, Fig. 57, Fig. 58. Nitrogen shows larger variations across the boundary layer in temperature Fig. 56, in density Fig. 59, as well as in entropy Fig. 62, for which FC-71 and PP11 experience small changes, Fig. 60, Fig. 61. As expected, the accelerating external flow causes the friction coefficient c_f for Nitrogen to increase with x , Fig. 63. For PP11, c_f increases slowly and FC-71 experiences even a decrease initially, despite the favourable pressure gradient imposed by the positive velocity gradient at the boundary layer edge. The Mach number variation on the boundary layer M_e , Fig. 64, also behaves in an unexpectedly manner for the BZT-fluids -after an increase at the beginning M_e eventually starts to decrease whereas the Mach number for the regular fluid Nitrogen increases continuous with x . This effect, a decreasing friction factor and

	N ₂	PP11	FC-71
\tilde{u}_∞ [m/s]	309	80	81
α_∞	0.14	0.0057	0.0062

Table 3: Free stream velocity and Eckert number: $M_\infty = 1.3$, $\tilde{v}_\infty = 0.71\tilde{v}_c$, $\tilde{T}_\infty = 1.03\tilde{T}_c$

non-monotonous Mach number variation, becomes more pronounced if the free stream values are chosen identical to the values at the point of separation in case C2 for FC-71, i.e. $M_\infty = 1.3$, $\tilde{v}_\infty = 0.71\tilde{v}_c$, $\tilde{T}_\infty = 1.03\tilde{T}_c$. The wall shear stress variations of the dense gas FC-71 displayed in Fig. 65 decrease significantly until $x = 0.15$ is reached where the calculations were stopped. The other BZT-fluid PP11 exhibits a similar but less distinguished behaviour while the skin friction for Nitrogen increases continuously. The displacement thickness distributions (Fig. 66) for the dense gases resemble those for the Blasius similarity solution whereas N₂ experiences a faster increase due to the larger influence of dissipation, Table 3. This unusual behaviour is triggered, as discussed in the previous section, by the Mach number variation (2.20), Fig. 67 which only can take place if the value of the fundamental derivate becomes smaller than one (2.21), Fig. 68. So, the isentropic expansion of dense gases must apparently not be followed by a continuous increase in skin friction but can, if the free stream thermodynamic state is chosen suitable, experience a decrease in wall shear stress caused by the non-monotonous Mach number distribution at the boundary layer edge.

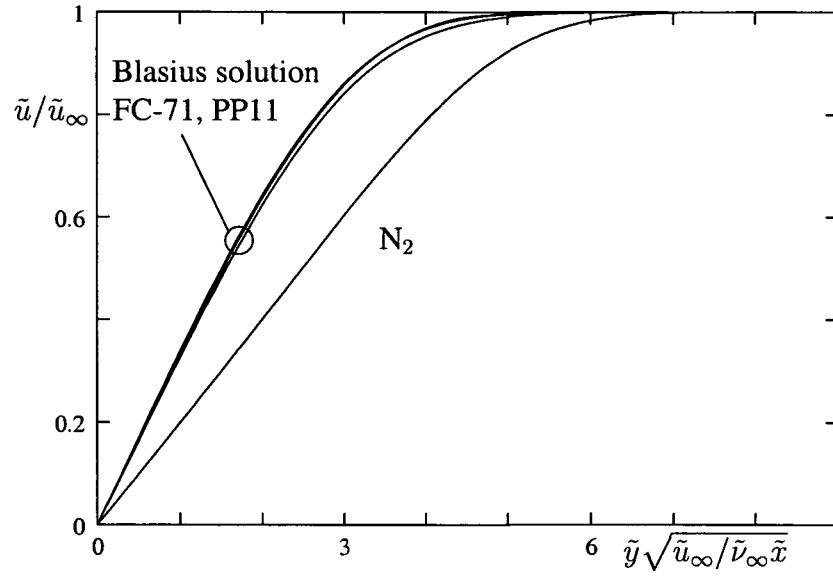


Figure 53: Velocity distributions at the leading edge of the plate $x = 0$: Blasius similarity solution FC-71, PP11, N_2 , $M_\infty = 2.0$, $\tilde{v}_\infty = 1.05\tilde{v}_c$, $\tilde{T}_\infty = 1.001\tilde{T}_c$.

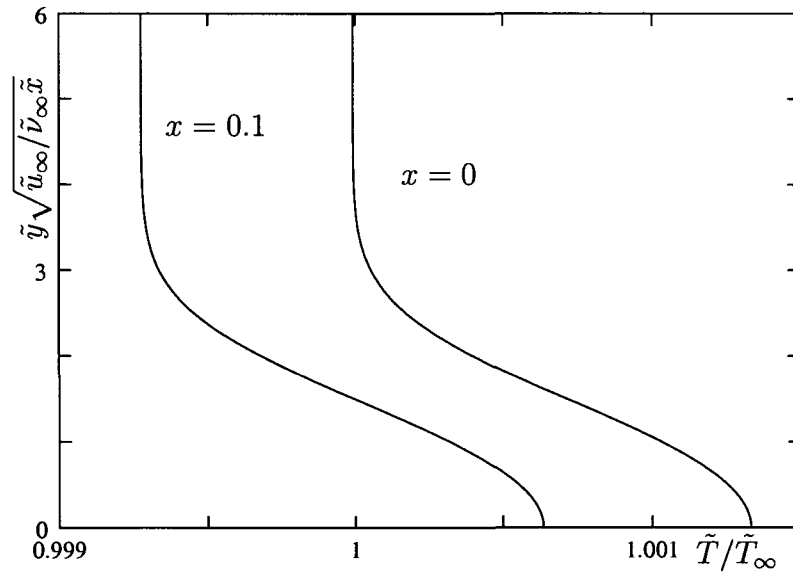


Figure 54: Temperature variation across the boundary layer at the leading edge of the plate $x = 0$ and at $x = 0.1$: FC-71, $M_\infty = 2.0$, $\tilde{v}_\infty = 1.05\tilde{v}_c$, $\tilde{T}_\infty = 1.001\tilde{T}_c$.

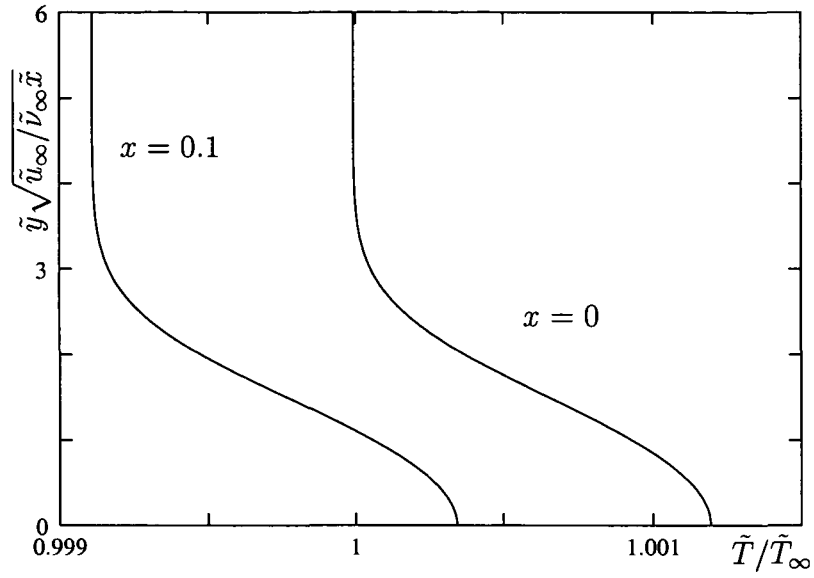


Figure 55: Temperature variation across the boundary layer at the leading edge of the plate $x = 0$ and at $x = 0.1$: PP11, $M_\infty = 2.0$, $\tilde{v}_\infty = 1.05\tilde{v}_c$, $\tilde{T}_\infty = 1.001\tilde{T}_c$.

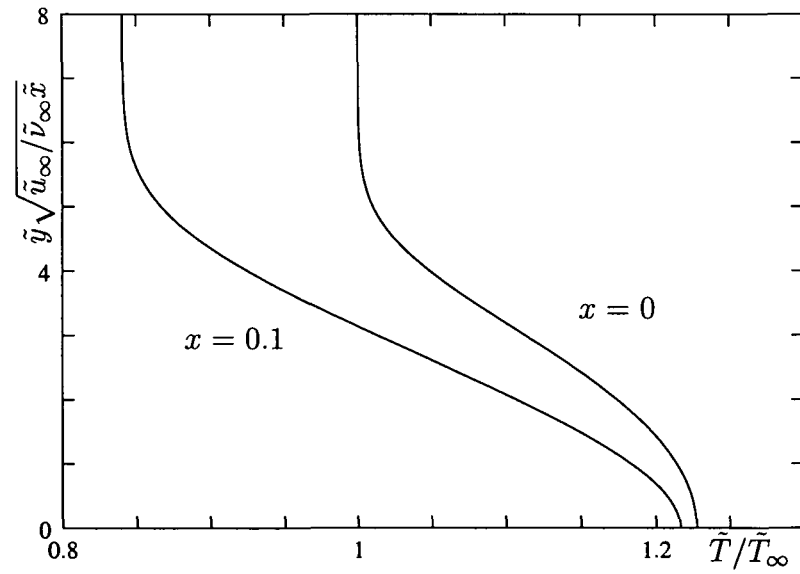


Figure 56: Temperature variation across the boundary layer at the leading edge of the plate $x = 0$ and at $x = 0.1$: N_2 , $M_\infty = 2.0$, $\tilde{v}_\infty = 1.05\tilde{v}_c$, $\tilde{T}_\infty = 1.001\tilde{T}_c$.

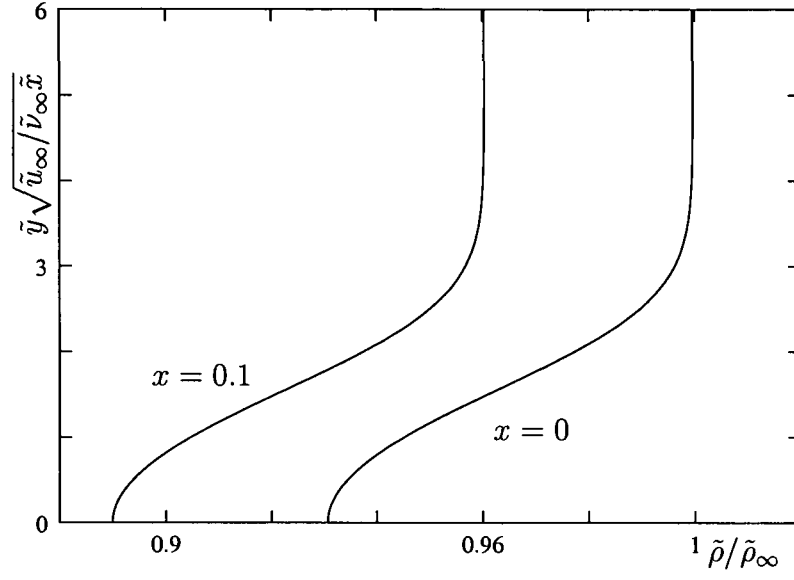


Figure 57: Density variation across the boundary layer at the leading edge of the plate $x = 0$ and at $x = 0.1$: FC-71, $M_\infty = 2.0$, $\tilde{\nu}_\infty = 1.05\tilde{\nu}_c$, $\tilde{T}_\infty = 1.001\tilde{T}_c$.

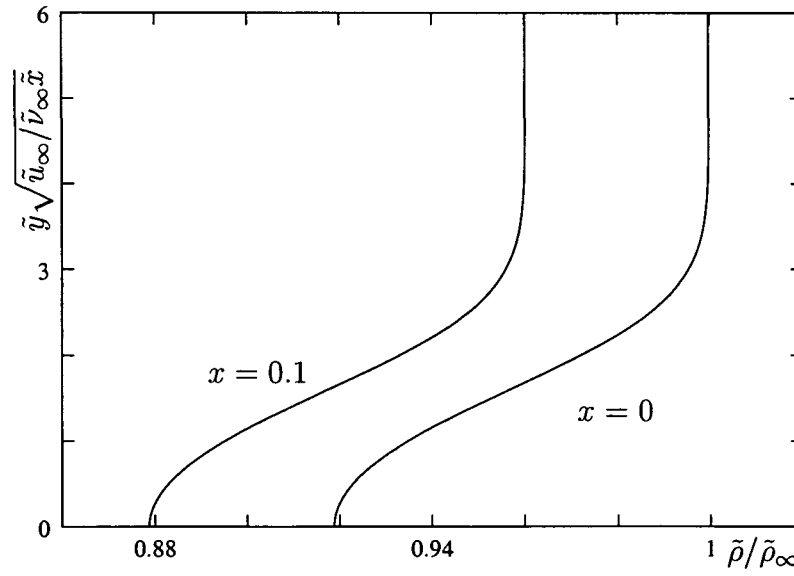


Figure 58: Density variation across the boundary layer at the leading edge of the plate $x = 0$ and at $x = 0.1$: PP11, $M_\infty = 2.0$, $\tilde{\nu}_\infty = 1.05\tilde{\nu}_c$, $\tilde{T}_\infty = 1.001\tilde{T}_c$.

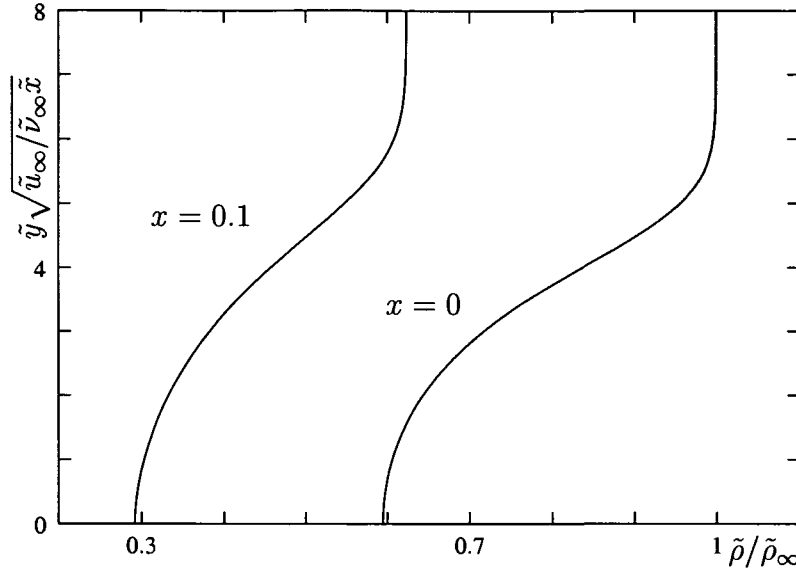


Figure 59: Density variation across the boundary layer at the leading edge of the plate $x = 0$ and at $x = 0.1$: N_2 , $M_\infty = 2.0$, $\tilde{v}_\infty = 1.05\tilde{v}_c$, $\tilde{T}_\infty = 1.001\tilde{T}_c$.

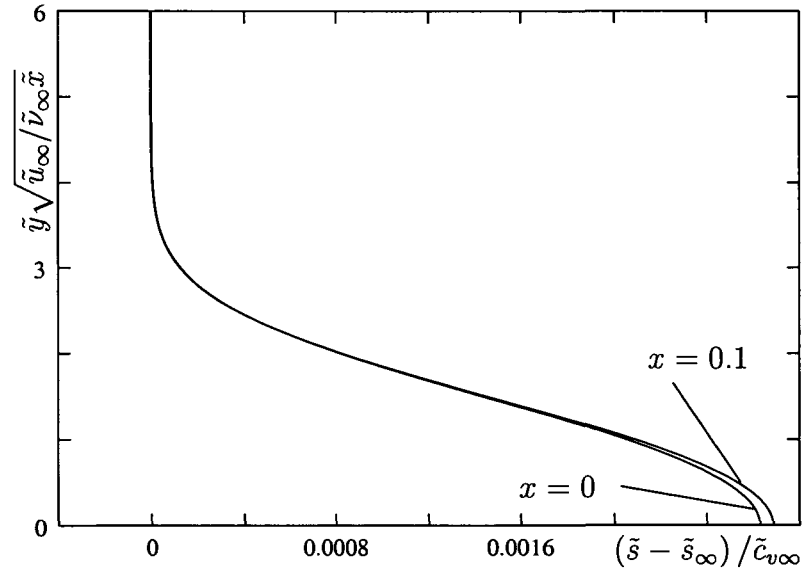


Figure 60: Entropy variation across the boundary layer at the leading edge of the plate $x = 0$ and at $x = 0.1$: FC-71, $M_\infty = 2.0$, $\tilde{v}_\infty = 1.05\tilde{v}_c$, $\tilde{T}_\infty = 1.001\tilde{T}_c$.

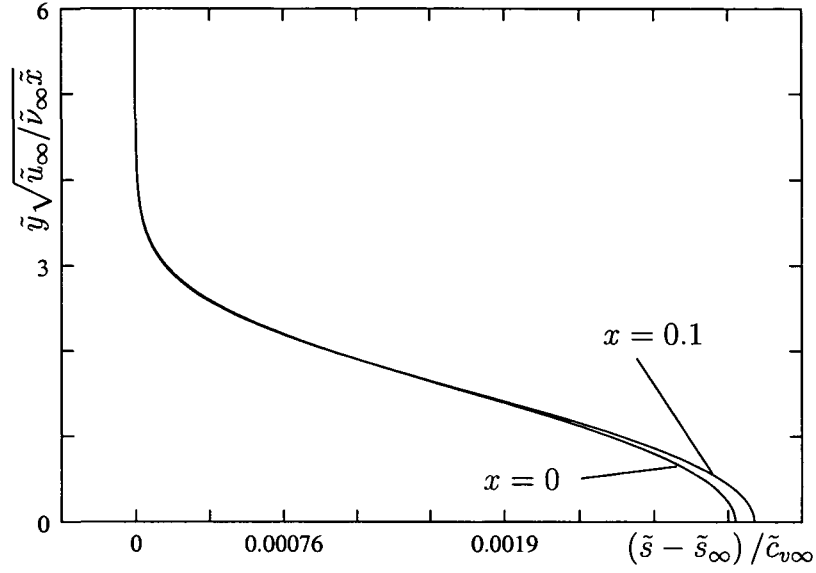


Figure 61: Entropy variation across the boundary layer at the leading edge of the plate $x = 0$ and at $x = 0.1$: PP11, $M_\infty = 2.0$, $\tilde{v}_\infty = 1.05\tilde{v}_c$, $\tilde{T}_\infty = 1.001\tilde{T}_c$.

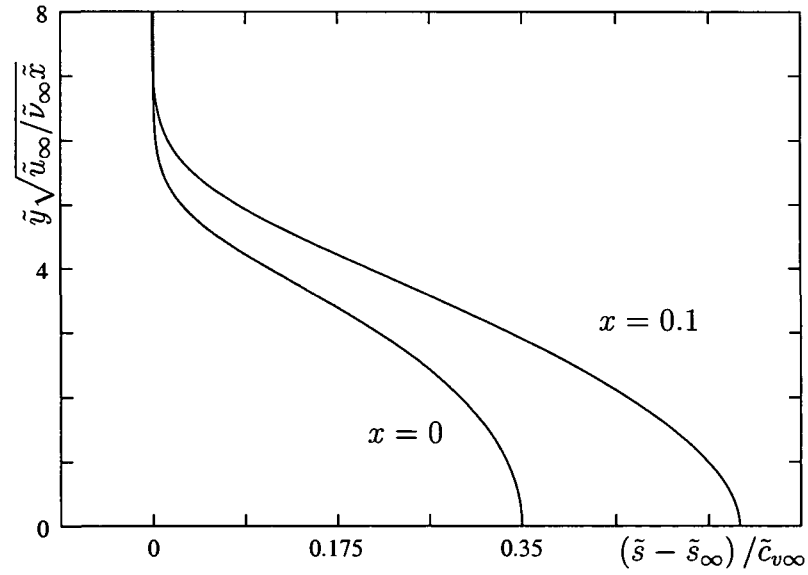


Figure 62: Entropy variation across the boundary layer at $x = 0$ and at the leading edge of the plate $x = 0.1$: N_2 , $M_\infty = 2.0$, $\tilde{v}_\infty = 1.05\tilde{v}_c$, $\tilde{T}_\infty = 1.001\tilde{T}_c$.

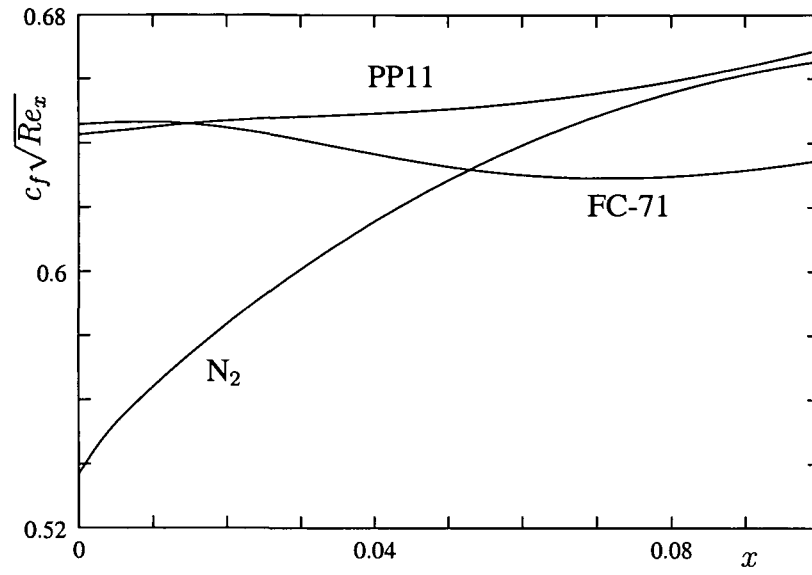


Figure 63: Distributions of the friction coefficient: $M_\infty = 2.0$, $v_\infty = 1.05v_c$, $T_\infty = 1.001T_c$.

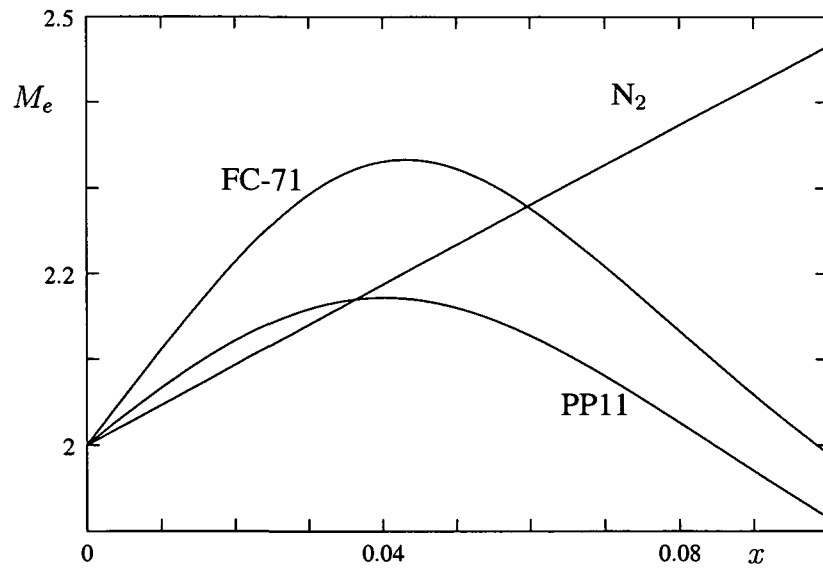


Figure 64: Mach number distribution at the boundary layer edge: $M_\infty = 2.0$, $v_\infty = 1.05v_c$, $T_\infty = 1.001T_c$.

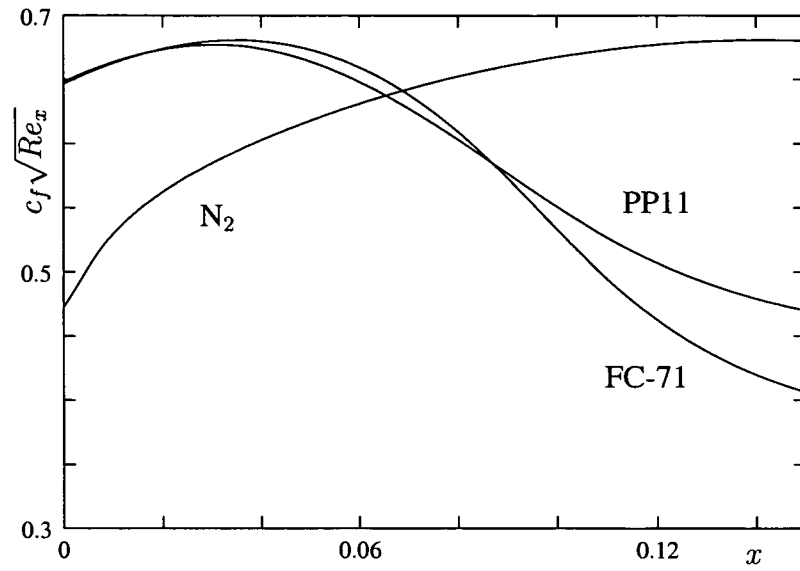


Figure 65: Distributions of the friction coefficient: $M_\infty = 1.3$, $\tilde{v}_\infty = 0.71\tilde{v}_c$, $\tilde{T}_\infty = 1.03\tilde{T}_c$.

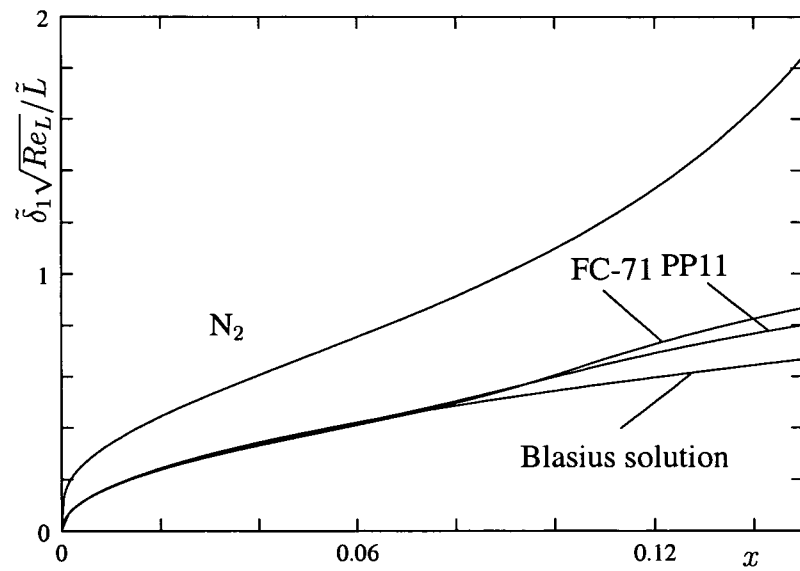


Figure 66: Distributions of the displacement thickness: $M_\infty = 1.3$, $\tilde{v}_\infty = 0.71\tilde{v}_c$, $\tilde{T}_\infty = 1.03\tilde{T}_c$.

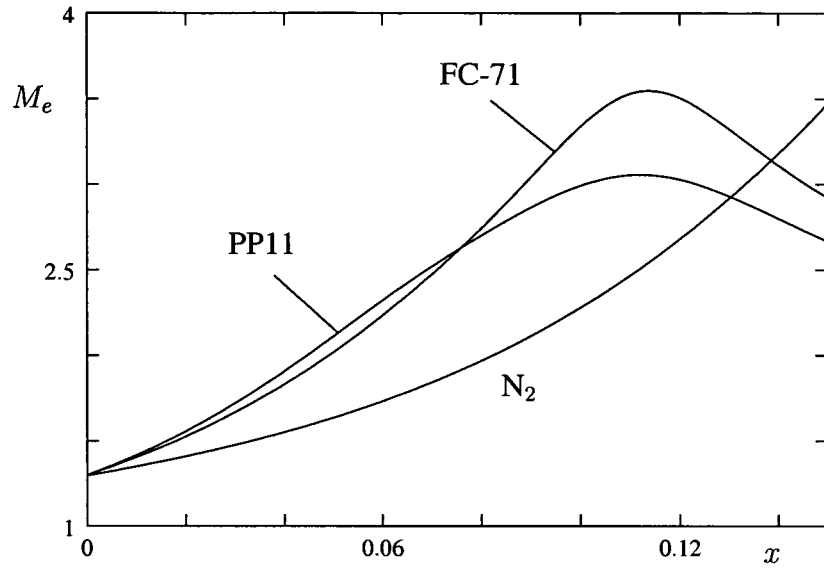


Figure 67: Mach number distribution at the boundary layer edge: $M_\infty = 1.3$, $\tilde{v}_\infty = 0.71\tilde{v}_c$, $\tilde{T}_\infty = 1.03\tilde{T}_c$.

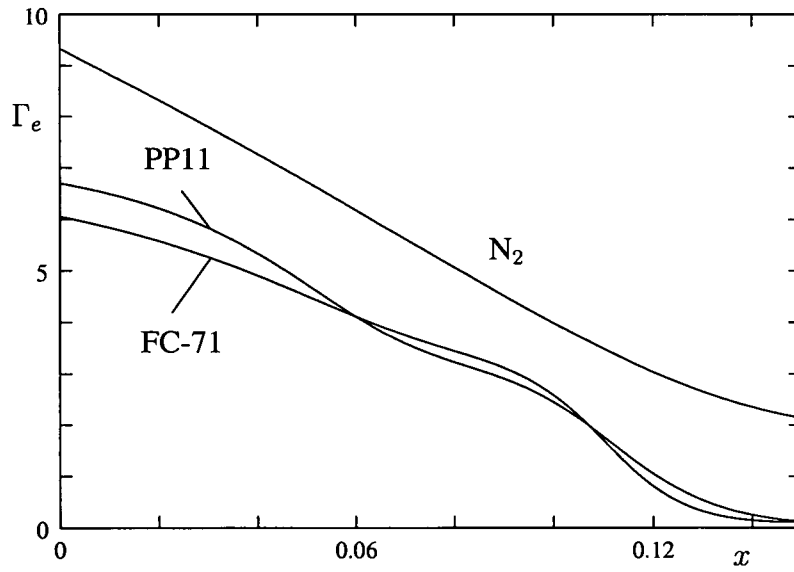


Figure 68: Distributions of the fundamental derivative at the boundary layer edge: $M_\infty = 1.3$, $\tilde{v}_\infty = 0.71\tilde{v}_c$, $\tilde{T}_\infty = 1.03\tilde{T}_c$.

2.4 Linearly retarded subsonic boundary layer flow

In the calculations of linearly retarded subsonic boundary layer flow the free stream Mach number M_∞ was chosen to be 0.2, the temperature $\tilde{T}_\infty = 1.001\tilde{T}_c$ as before, the velocity gradient $\zeta = -1$ and the specific volume \tilde{v}_∞ was varied. It was found, however, that the behaviour of the flow did not change substantially with the thermodynamic state. Therefore, only the results for the case $\tilde{v}_\infty = 5.0\tilde{v}_c$, are shown here. The velocity profiles at the leading edge for Nitrogen and the BZT fluids are almost identical to the Blasius similarity solution, Figure 69. The temperature (Fig. 70, Fig. 71, Fig. 72), density (Fig. 73 Fig. 74, Fig. 75, Fig. 76) and entropy (Fig. 77, Fig. 78, Fig. 79) variations across the boundary are small for all three substances in comparison to those occurring in the supersonic flows. As far as the friction coefficient (Fig. 80), displacement thickness (Fig. 81) and Mach number (Fig. 82) distributions are concerned there is hardly a difference to be seen between FC-71, PP11, N_2 and, as expected, all solutions of the boundary layer equations terminate in a Goldstein singularity.

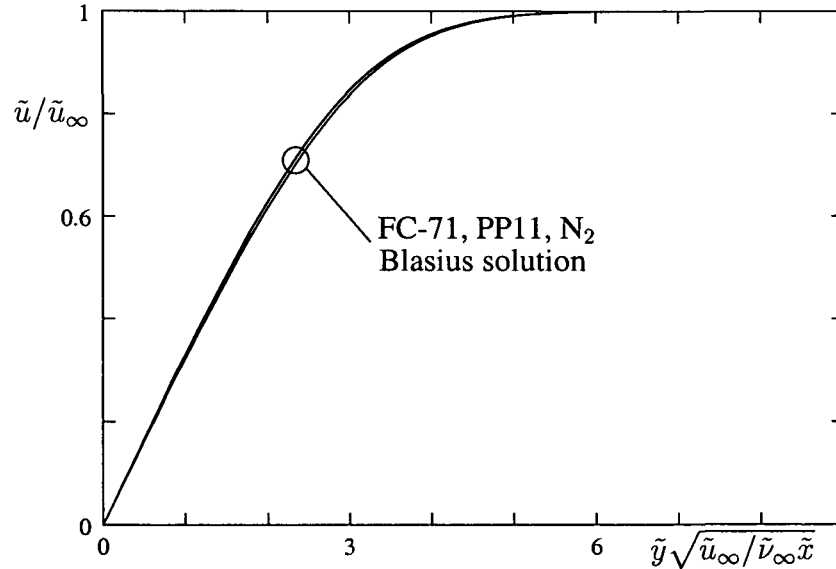


Figure 69: Velocity distributions at the leading edge of the plate $x = 0$: Blasius similarity solution, FC-71, PP11, N_2 , $M_\infty = 0.2$, $\tilde{v}_\infty = 5.0\tilde{v}_c$, $\tilde{T}_\infty = 1.001\tilde{T}_c$.

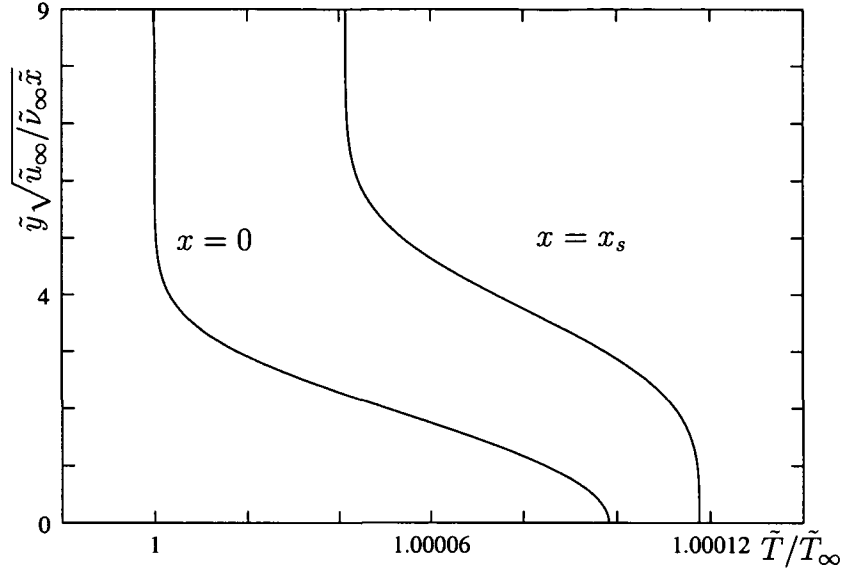


Figure 70: Temperature variation across the boundary layer at the leading edge of the plate $x = 0$ and at the point of separation x_s : FC-71, $M_\infty = 0.2$, $\tilde{v}_\infty = 5.0\tilde{v}_c$, $\tilde{T}_\infty = 1.001\tilde{T}_c$.

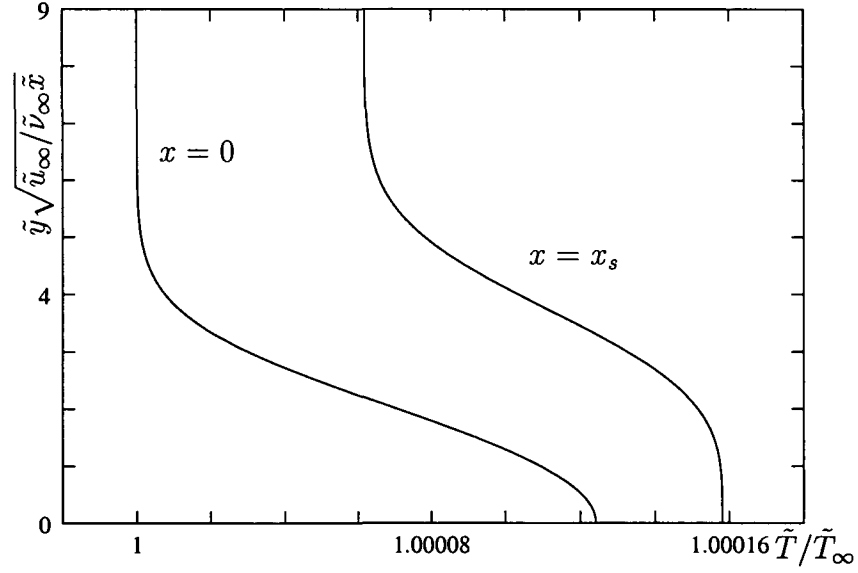


Figure 71: Temperature variation across the boundary layer at the leading edge of the plate $x = 0$ and at the point of separation x_s : PP11, $M_\infty = 0.2$, $\tilde{v}_\infty = 5.0\tilde{v}_c$, $\tilde{T}_\infty = 1.001\tilde{T}_c$.

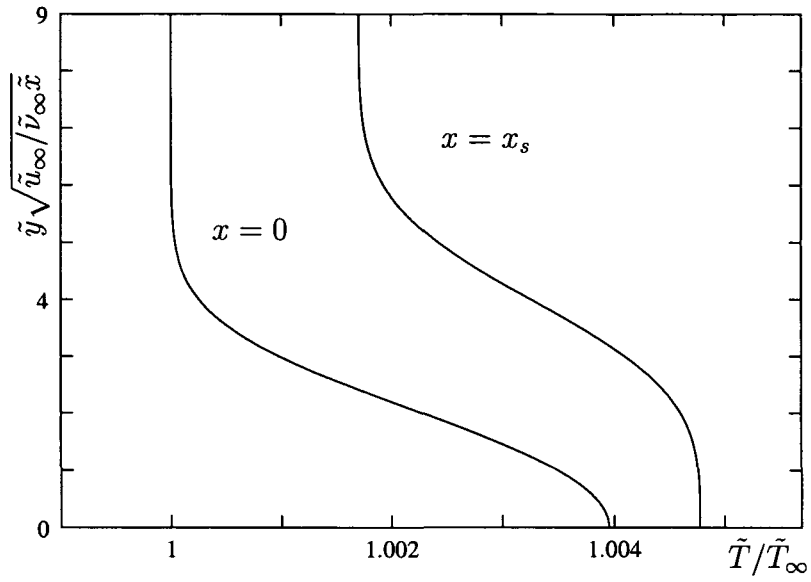


Figure 72: Temperature variation across the boundary layer at the leading edge of the plate $x = 0$ and at the point of separation x_s : N_2 , $M_\infty = 0.2$, $\tilde{\nu}_\infty = 5.0\tilde{\nu}_c$, $\tilde{T}_\infty = 1.001\tilde{T}_c$.

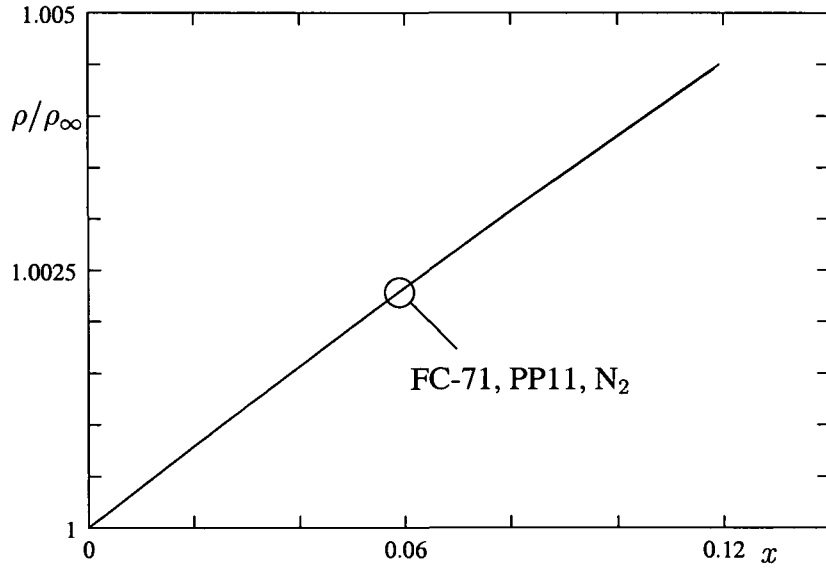


Figure 73: Density variation at the edge of the boundary layer: $M_\infty = 0.2$, $\tilde{\nu}_\infty = 5.0\tilde{\nu}_c$, $\tilde{T}_\infty = 1.001\tilde{T}_c$.

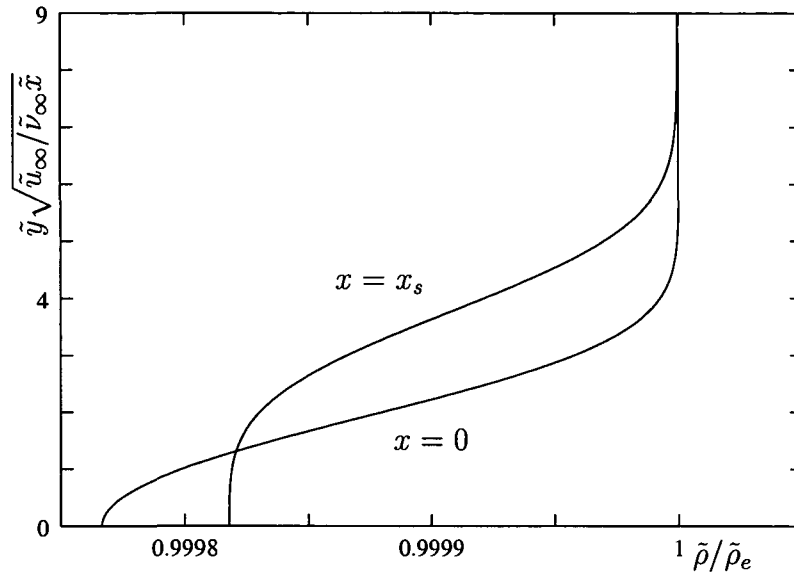


Figure 74: Density variation across the boundary layer at the leading edge of the plate $x = 0$ and at the point of separation x_s : FC-71, $M_\infty = 0.2$, $\tilde{v}_\infty = 5.0\tilde{v}_c$, $\tilde{T}_\infty = 1.001\tilde{T}_c$.

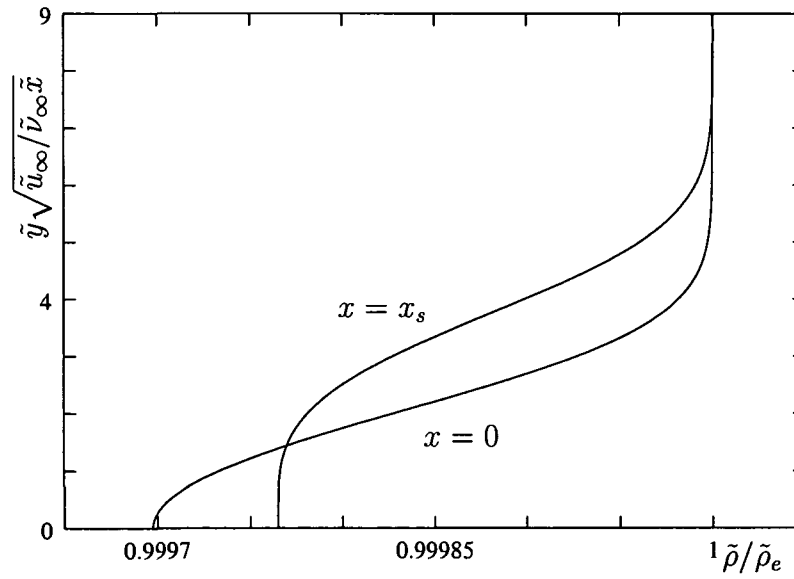


Figure 75: Density variation across the boundary layer at the leading edge of the plate $x = 0$ and at the point of separation x_s : PP11, $M_\infty = 0.2$, $\tilde{v}_\infty = 5.0\tilde{v}_c$, $\tilde{T}_\infty = 1.001\tilde{T}_c$.

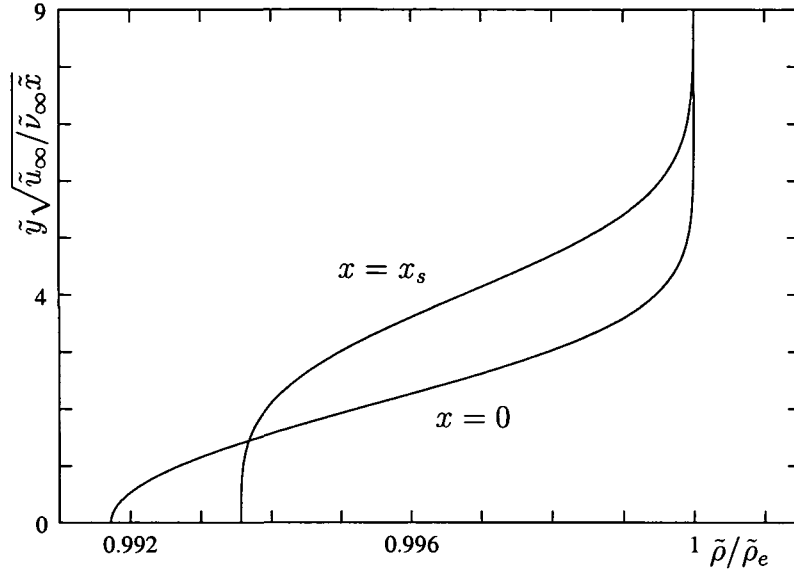


Figure 76: Density variation across the boundary layer at the leading edge of the plate $x = 0$ and at the point of separation x_s : N_2 , $M_\infty = 0.2$, $\tilde{\nu}_\infty = 5.0\tilde{\nu}_c$, $\tilde{T}_\infty = 1.001\tilde{T}_c$.

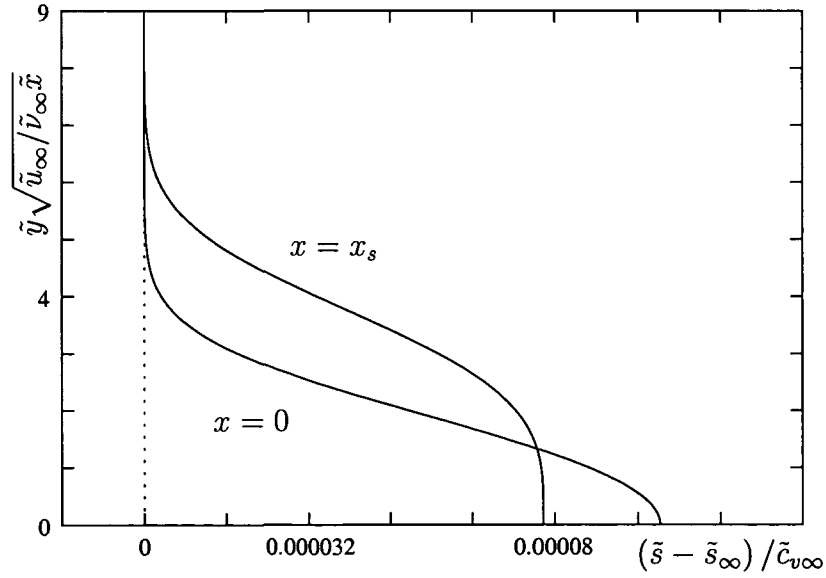


Figure 77: Entropy variation across the boundary layer at the leading edge of the plate $x = 0$ and at the point of separation x_s : FC-71, $M_\infty = 0.2$, $\tilde{\nu}_\infty = 5.0\tilde{\nu}_c$, $\tilde{T}_\infty = 1.001\tilde{T}_c$.

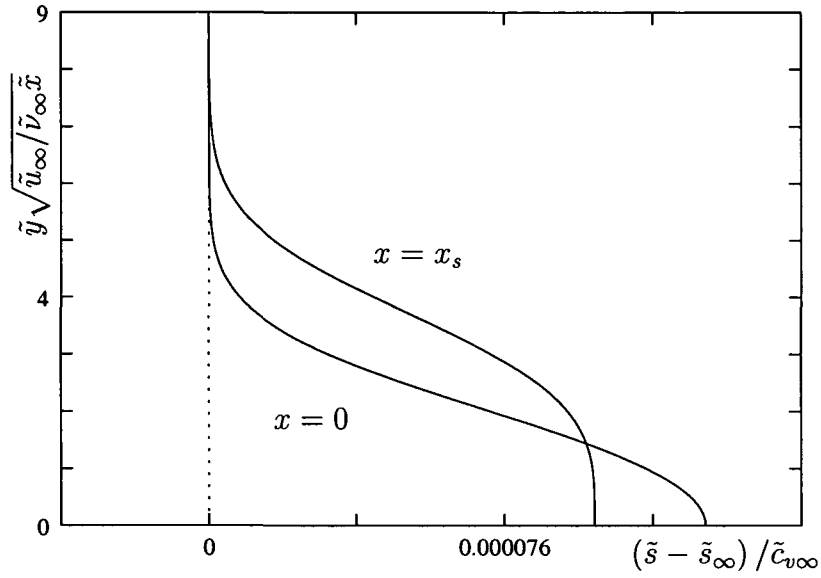


Figure 78: Entropy variation across the boundary layer at the leading edge of the plate $x = 0$ and at the point of separation x_s : PP11, $M_\infty = 0.2$, $\tilde{v}_\infty = 5.0\tilde{v}_c$, $\tilde{T}_\infty = 1.001\tilde{T}_c$.

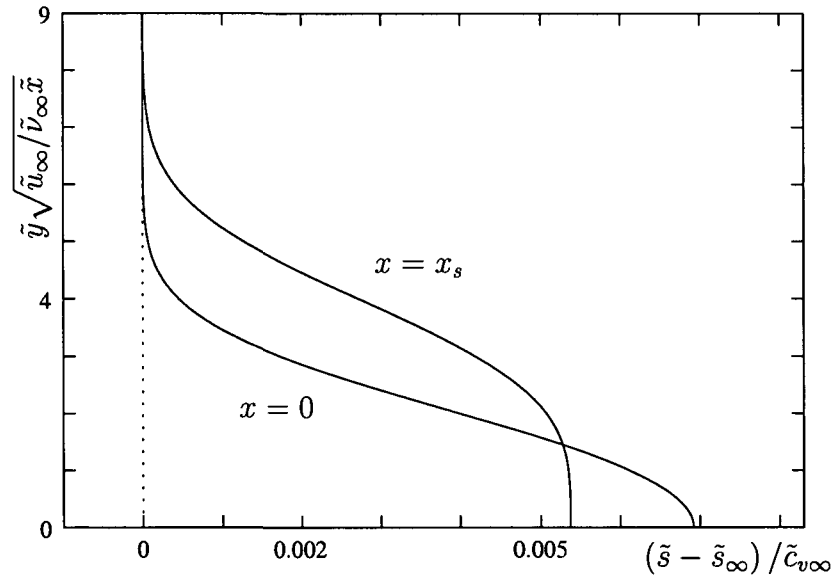


Figure 79: Entropy variation across the boundary layer at the leading edge of the plate $x = 0$ and at the point of separation x_s : N_2 , $M_\infty = 0.2$, $\tilde{v}_\infty = 5.0\tilde{v}_c$, $\tilde{T}_\infty = 1.001\tilde{T}_c$.

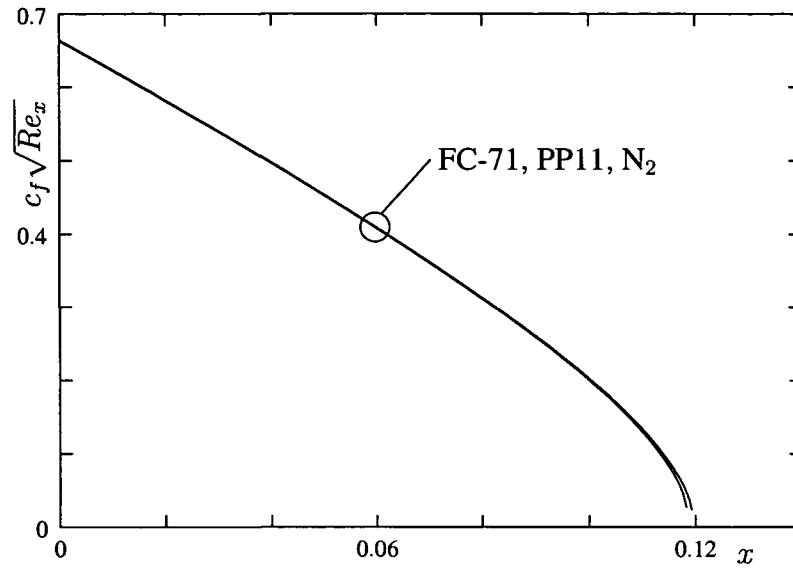


Figure 80: Distributions of the friction coefficient: $M_\infty = 0.2$, $\tilde{v}_\infty = 5.0\tilde{v}_c$, $\tilde{T}_\infty = 1.001\tilde{T}_c$.

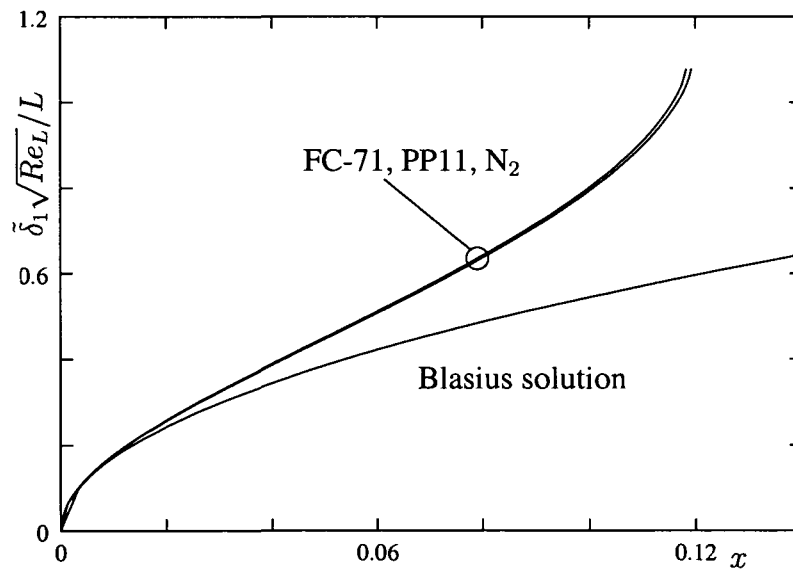


Figure 81: Distributions of the displacement thickness: $M_\infty = 0.2$, $\tilde{v}_\infty = 5.0\tilde{v}_c$, $\tilde{T}_\infty = 1.001\tilde{T}_c$.

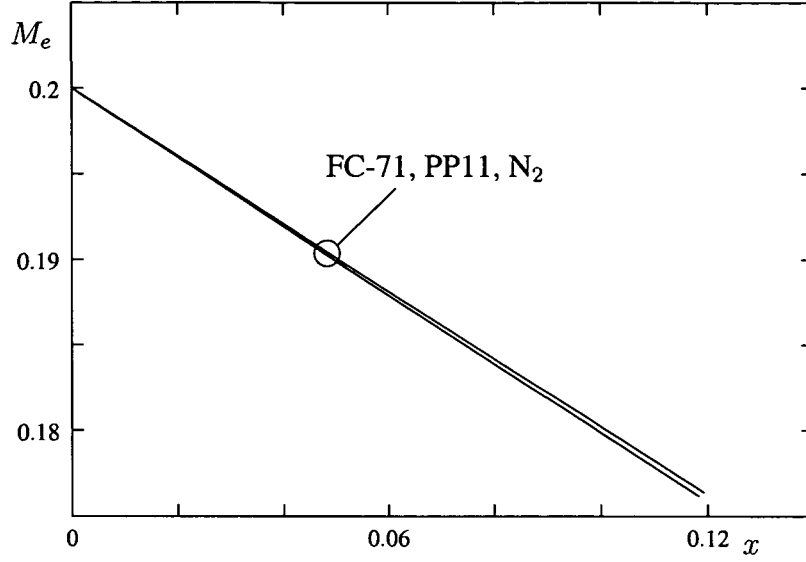


Figure 82: Mach number distribution at the boundary layer edge: $M_\infty = 0.2$, $\tilde{v}_\infty = 5.0\tilde{v}_c$, $\tilde{T}_\infty = 1.001\tilde{T}_c$.

2.5 Linearly accelerating subsonic boundary layer flow

We now turn to linearly accelerating subsonic boundary layer flows where the external velocity is described by the relationship

$$u_e = 1 + \zeta x, \quad \zeta = 1.$$

As in the previous section we choose the free stream Mach number, the temperature of the oncoming flow to be 0.2, $1.001\tilde{T}_c$, respectively and vary the specific volume \tilde{v}_∞ . Similar to linearly retarded subsonic boundary layer flows, it was found that the flow did not depend strongly on the thermodynamic state of the oncoming flow. Therefore, we show here results for the case $\tilde{v} = 5.0\tilde{v}_c$ only which are representative for all flows calculated. The velocity profiles at the leading edge for the three substances are similar to the Blasius similarity solution, Fig. 83. The temperature (Fig. 84, Fig. 85, Fig. 86), density (Fig. 87 Fig. 88, Fig. 89, Fig. 90) and entropy (Fig. 91, Fig. 92, Fig. 93) variations across the boundary are small for all three substances in comparison to the investigated cases of supersonic flows and somewhat larger than for the linearly retarded subsonic flow. The latter is due to the fact that the linearly accelerating external flow causes the wall shear stress (Fig. 94) to increase and, therefore, separation of the boundary layer is avoided and the calculations are instead terminated at the end of the plate. The distributions of the the friction coefficient (Fig. 94), displacement thickness (Fig. 95) and Mach number (Fig. 96) for N_2 , FC-71 and PP11 are found to differ only slightly.

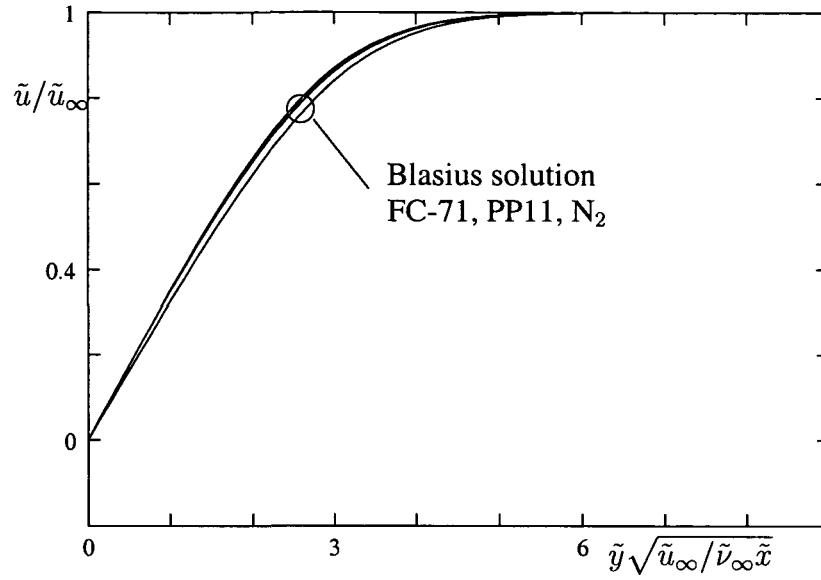


Figure 83: Velocity distributions at the leading edge of the plate $x = 0$: Blasius similarity solution, FC-71, PP11, N_2 , $M_\infty = 0.2$, $\tilde{v}_\infty = 5.0\tilde{v}_c$, $\tilde{T}_\infty = 1.001\tilde{T}_c$.

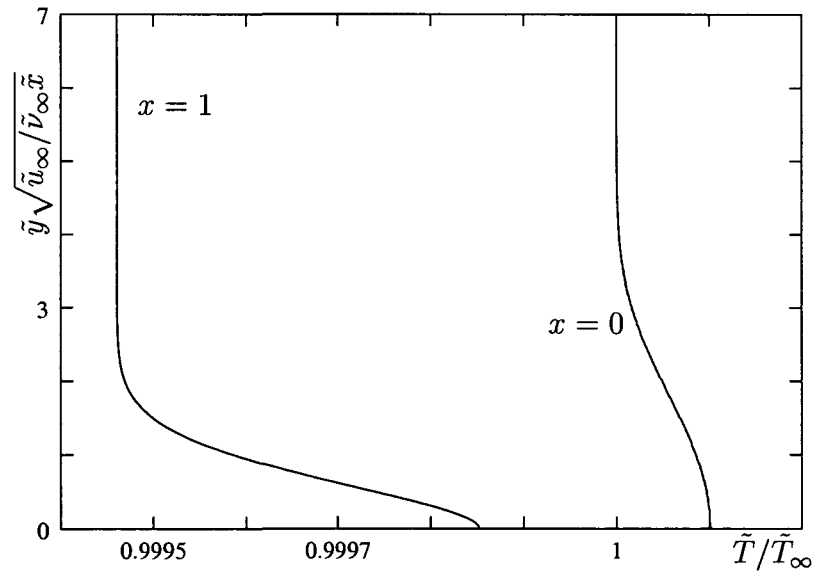


Figure 84: Temperature variation across the boundary layer at the leading edge of the plate $x = 0$ and at the end of the plate $x = 1$: FC-71, $M_\infty = 0.2$, $\tilde{v}_\infty = 5.0\tilde{v}_c$, $\tilde{T}_\infty = 1.001\tilde{T}_c$.

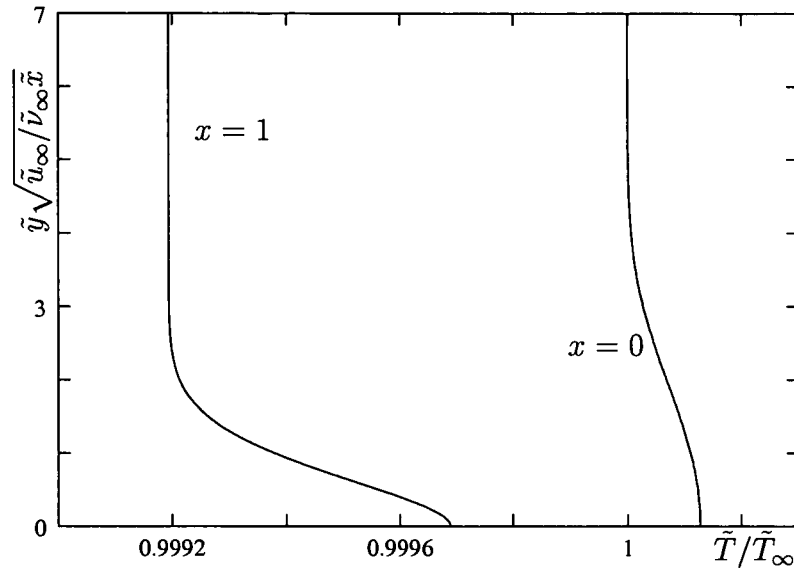


Figure 85: Temperature variation across the boundary layer at the leading edge of the plate $x = 0$ and at the end of the plate $x = 1$: PP11, $M_\infty = 0.2$, $\tilde{\nu}_\infty = 5.0\tilde{\nu}_c$, $\tilde{T}_\infty = 1.001\tilde{T}_c$.

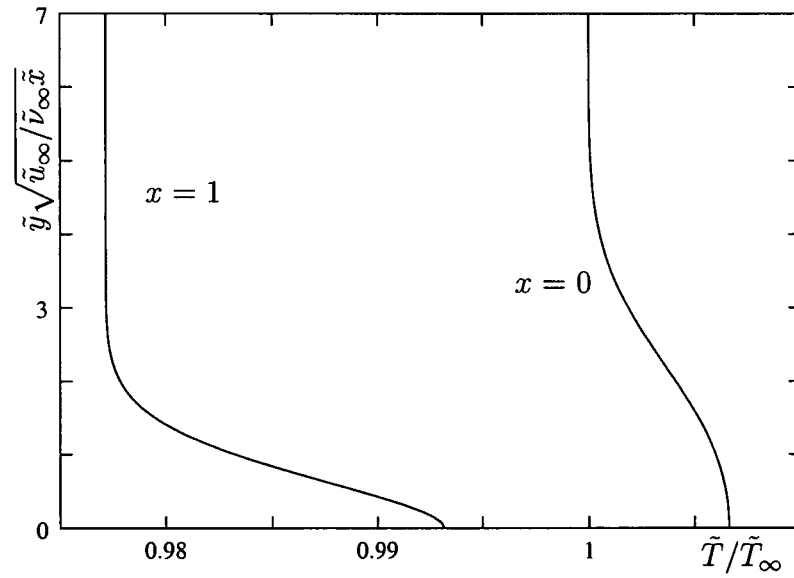


Figure 86: Temperature variation across the boundary layer at the leading edge of the plate $x = 0$ and at the end of the plate $x = 1$: N₂, $M_\infty = 0.2$, $\tilde{\nu}_\infty = 5.0\tilde{\nu}_c$, $\tilde{T}_\infty = 1.001\tilde{T}_c$.

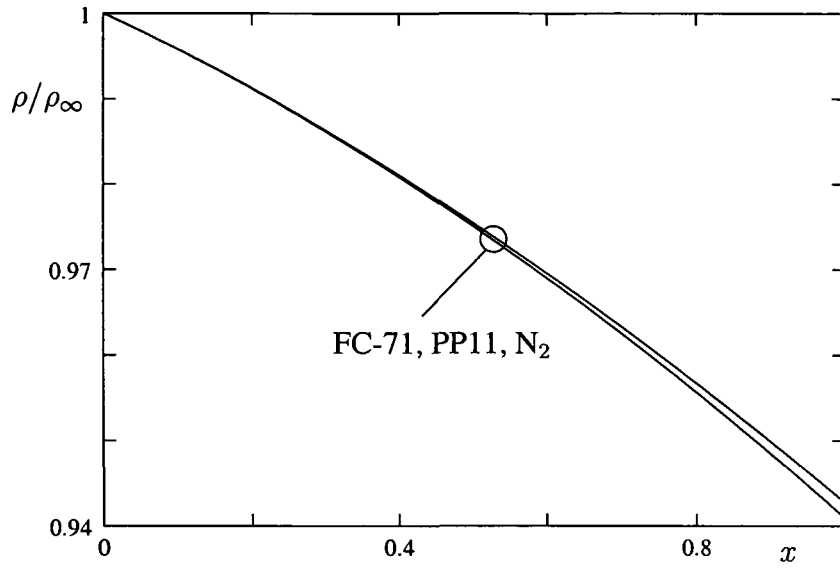


Figure 87: Density variation at the edge of the boundary layer: $M_\infty = 0.2$, $\tilde{v}_\infty = 5.0\tilde{v}_c$, $\tilde{T}_\infty = 1.001\tilde{T}_c$.

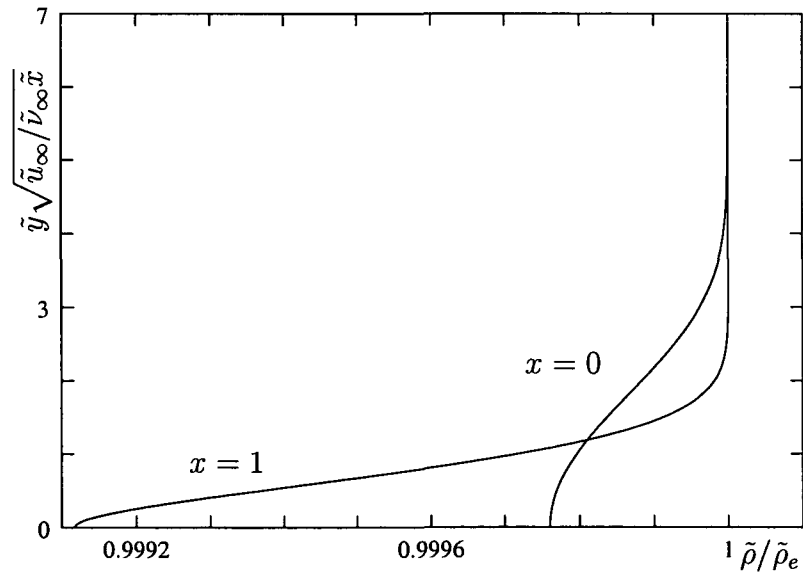


Figure 88: Density variation across the boundary layer at the leading edge of the plate $x = 0$ and at the end of the plate $x = 1$: FC-71, $M_\infty = 0.2$, $\tilde{v}_\infty = 5.0\tilde{v}_c$, $\tilde{T}_\infty = 1.001\tilde{T}_c$.

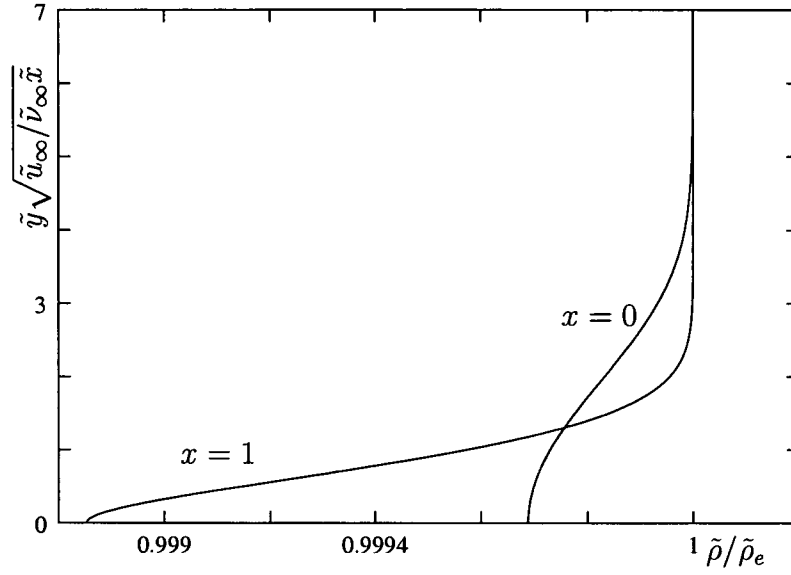


Figure 89: Density variation across the boundary layer at the leading edge of the plate $x = 0$ and at the end of the plate $x = 1$: PP11, $M_\infty = 0.2$, $\tilde{v}_\infty = 5.0\tilde{v}_c$, $\tilde{T}_\infty = 1.001\tilde{T}_c$.

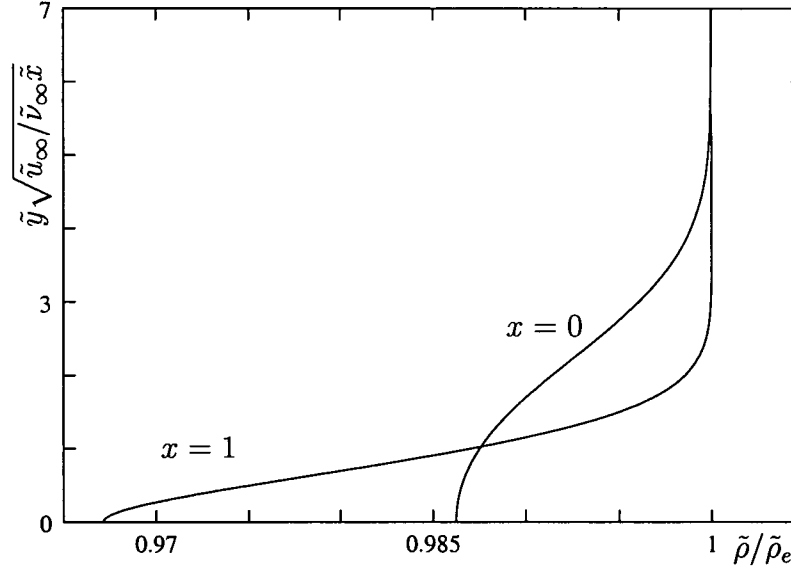


Figure 90: Density variation across the boundary layer at the leading edge of the plate $x = 0$ and at the end of the plate $x = 1$: N_2 , $M_\infty = 0.2$, $\tilde{v}_\infty = 5.0\tilde{v}_c$, $\tilde{T}_\infty = 1.001\tilde{T}_c$.

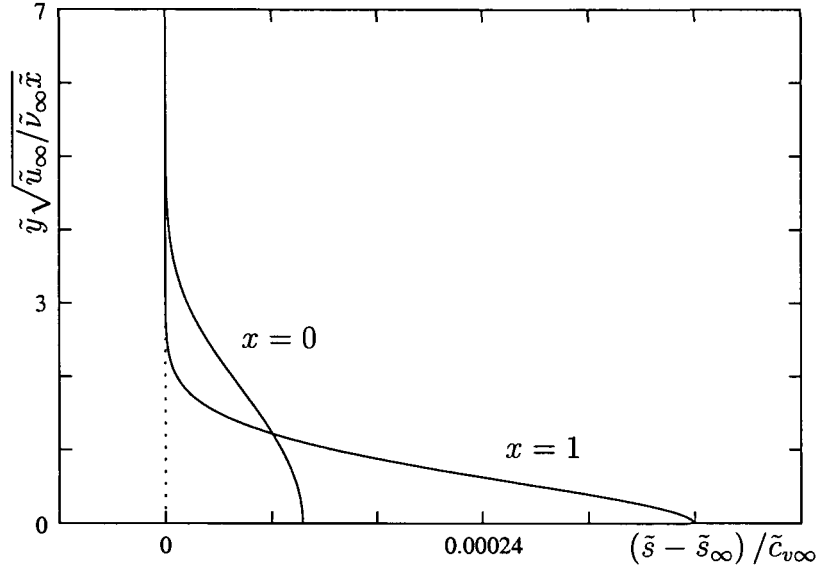


Figure 91: Entropy variation across the boundary layer at the leading edge of the plate $x = 0$ and at the end of the plate $x = 1$: FC-71, $M_\infty = 0.2$, $\tilde{v}_\infty = 5.0\tilde{v}_c$, $\tilde{T}_\infty = 1.001\tilde{T}_c$.

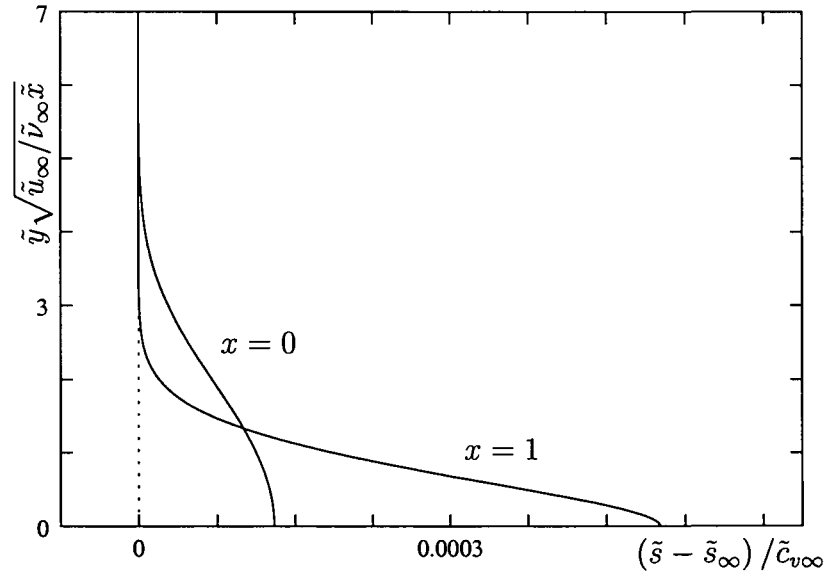


Figure 92: Entropy variation across the boundary layer at the leading edge of the plate $x = 0$ and at the end of the plate $x = 1$: PP11, $M_\infty = 0.2$, $\tilde{v}_\infty = 5.0\tilde{v}_c$, $\tilde{T}_\infty = 1.001\tilde{T}_c$.

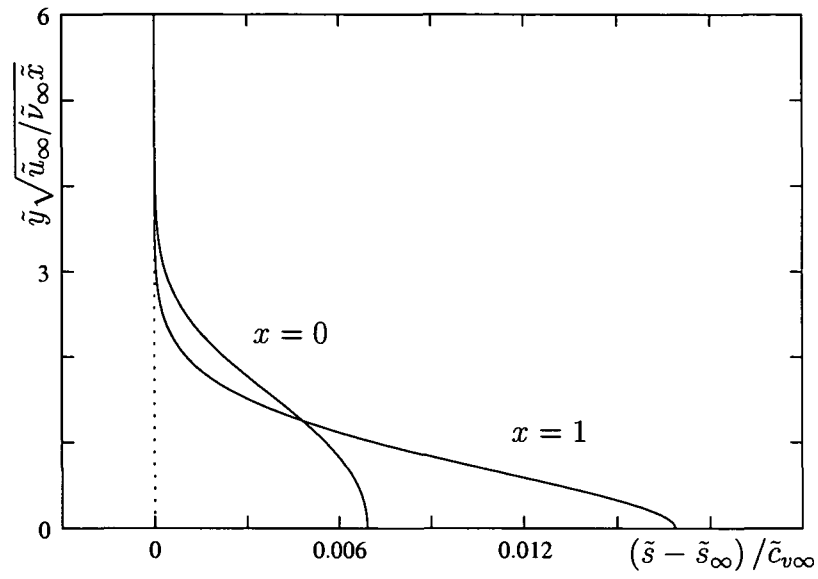


Figure 93: Entropy variation across the boundary layer at the leading edge of the plate $x = 0$ and at the end of the plate $x = 1$: N_2 , $M_\infty = 0.2$, $\tilde{\nu}_\infty = 5.0\tilde{\nu}_c$, $\tilde{T}_\infty = 1.001\tilde{T}_c$.

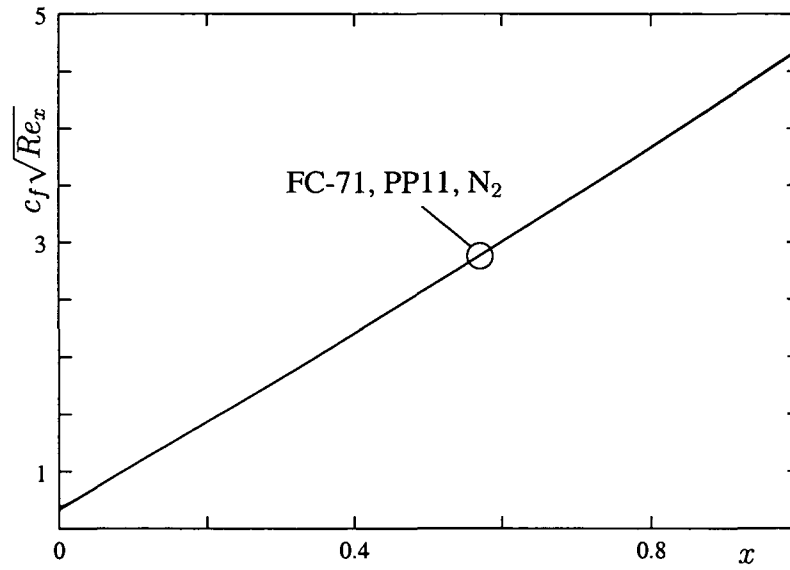


Figure 94: Distributions of the friction coefficient: $M_\infty = 0.2$, $\tilde{\nu}_\infty = 5.0\tilde{\nu}_c$, $\tilde{T}_\infty = 1.001\tilde{T}_c$.

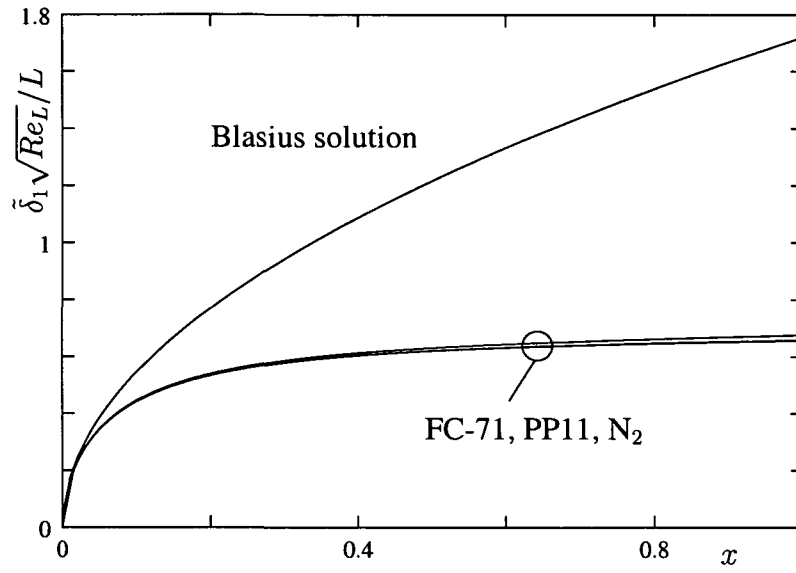


Figure 95: Distributions of the displacement thickness: $M_\infty = 0.2$, $\tilde{v}_\infty = 5.0\tilde{v}_c$, $\tilde{T}_\infty = 1.001\tilde{T}_c$.

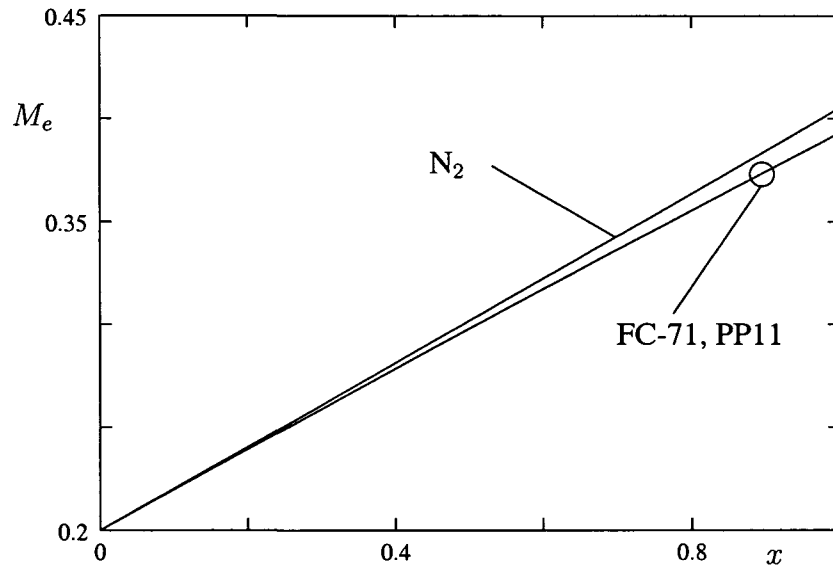


Figure 96: Mach number distribution at the boundary layer edge: $M_\infty = 0.2$, $\tilde{v}_\infty = 5.0\tilde{v}_c$, $\tilde{T}_\infty = 1.001\tilde{T}_c$.

3 Asymptotic theory of marginal separation in dense gases

Here we are considering the linearly retarded supersonic two-dimensional flow of viscous and compressible fluid on a flat plate. The numerical calculations of the boundary layer for the BZT fluid FC-71 in section 2.2 indicate that if the thermodynamic state of the free stream flow is correctly chosen, we obtain a marginal separation singularity (Figure 97). In the studies of marginal separation of an in-

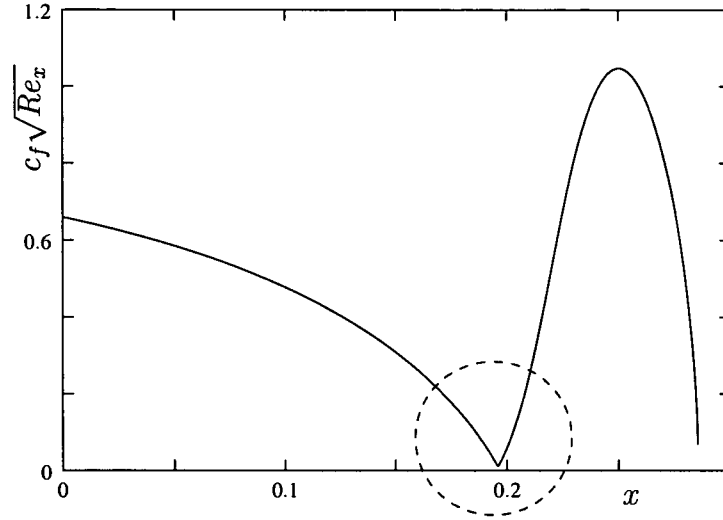


Figure 97: Marginal separation for the BZT-fluid FC-71 at $\rho_{\infty r} = 0.1996$ $T_{\infty r} = 1.001$ and $M_{\infty} = 2.0$. The region where the friction coefficient recovers is the region of interest in this section.

compressible flow past an airfoil [27], [28], [30] it was found that there exists a limiting solution of the boundary layer equations which can be extended through a point of vanishing wall shear. This solution is embedded in one parameter family of solutions which describes the transition from completely smooth wall shear distributions to wall shear distributions which terminate in a separation singularity depending on a certain control parameter k . In the previous mentioned investigations, k was the angle of attack and it was found that there exists a critical value of attack k_0 . If

$$\Delta k = k - k_0 \quad (3.1)$$

is smaller than zero we obtain the smooth solution whereas $\Delta k > 0$ yields the singularity. In the limit $\Delta k \rightarrow 0^+$ the strength of the singularity becomes arbitrarily small and if the interaction between the boundary layer and the external flow is

taken into account one obtains a smooth solution with a short region of negative wall shear stress. In this study, the place of angel of attack is taken by the free

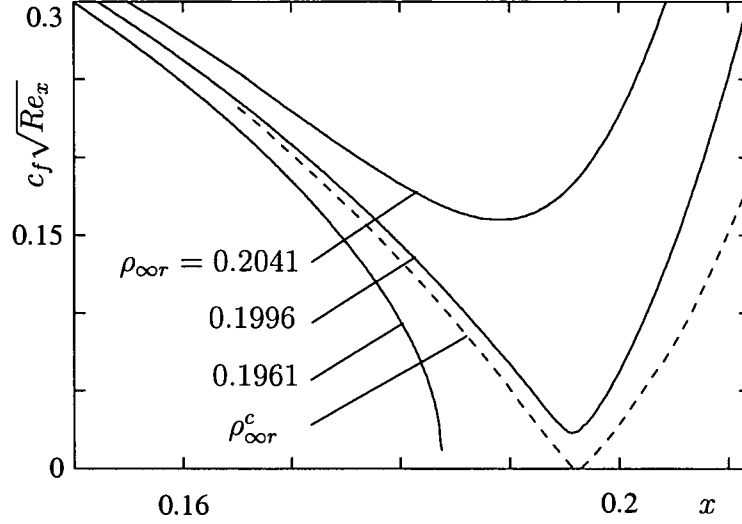


Figure 98: Numerical calculation of the boundary layer. Friction coefficient distribution for FC-71 at $T_{\infty r} = 1.001$ and $M_{\infty} = 2.0$.

stream density $\rho_{\infty r}$ non-dimensionalized with the thermodynamic critical density. Figure 98 displays three numerical calculations of the boundary layer for FC-71 at different free stream densities. The dashed line represents the case where $\Delta k = 0$ for which the marginal separation singularity arises and the wall shear stress vanishes in a single point. Denoting the value of $\rho_{\infty r}$ for this case $\rho_{\infty r}^c$, the numerical results indicate that if $\rho_{\infty r} < \rho_{\infty r}^c$ a Goldstein singularity forms [22] while the wall shear stress remains positive throughout if $\rho_{\infty r} > \rho_{\infty r}^c$. This suggests that in the present case the appropriate meaning of Δk is

$$\Delta k = \frac{\rho_{\infty r}^c - \rho_{\infty r}}{\rho_{\infty r}^c \rho_{\infty r}}.$$

In the following study of the marginal separation using asymptotic methods, it is convenient to use the notation

$$\Delta k = \epsilon k_1,$$

where $\epsilon \ll 1$ and $k_1 = O(1)$.

3.1 Thermodynamical considerations

We continue to consider the thermodynamical properties of BZT-fluids. Similar to the case of ideal gases [20]

$$\beta = O(T^{-1}), \quad Pr = O(1). \quad (3.2)$$

In contrast to ideal gases, however, where the Eckert number

$$Ec = \left(\frac{c_{p\infty}}{c_{v\infty}} - 1 \right) M_\infty^2 = O(M_\infty^2),$$

since the ratio of the specific heats is of the order one, we now have [20]

$$Ec = O(M_\infty^2 \frac{R}{c_{v\infty}}), \quad (3.3)$$

which is found by using e.g. the Van der Waals gas model, the definitions for specific enthalpy and speed of sound. BZT-fluids are characterised by large isochoric heat capacities non-dimensionalized with the universal gas constant R , typically of the order 10^2 according to [8] and [9], Table 4. Consequently, the Eckert num-

Fluid	$c_{v\infty}^c$	$\Gamma_{min}(T_c)$
$C_{12}F_{27}N$, FC-43, pf-tributylamine	93.0	-0.03
$C_{15}F_{33}N$, FC-70, pf-tripentylamine	118.7	-0.17
$C_{18}F_{39}N$, FC-71, pf-trihexylamine	145.0	-0.29
$C_{13}F_{22}$, PP10, pf-perhydrofluorene	78.4	-0.08
$C_{14}F_{24}$, PP11, pf-perhydrophenanthrene	97.3	-0.15
$C_{16}F_{26}$, PP24, pf-fluoranthene	112.0	-0.36

Table 4: $c_{v\infty}^c$ for representative negative Γ fluids. $\Gamma_{min}(T_c)$ denotes the minimum value of Γ on the critical isotherm [8].

ber will be small for even moderately large supersonic Mach numbers and we can write the energy equation (1.16) in the form

$$\rho c_p \left(u \frac{\partial T}{\partial x} + v \frac{\partial T}{\partial Y} \right) = \frac{1}{Pr} \frac{\partial}{\partial Y} \left(k \frac{\partial T}{\partial Y} \right) + O(Ec). \quad (3.4)$$

Together with the boundary conditions (1.17) we can, therefore, infer that

$$\frac{\partial T}{\partial x} \sim \frac{\partial T}{\partial Y} \sim \frac{\partial \rho}{\partial Y} = O(Ec), \quad (3.5)$$

i.e. the changes in temperature in the whole flow field are of the order Ec and so are the changes of density across the boundary layer. A numerical calculation with $Ec = 0$ is displayed in Figure 99.

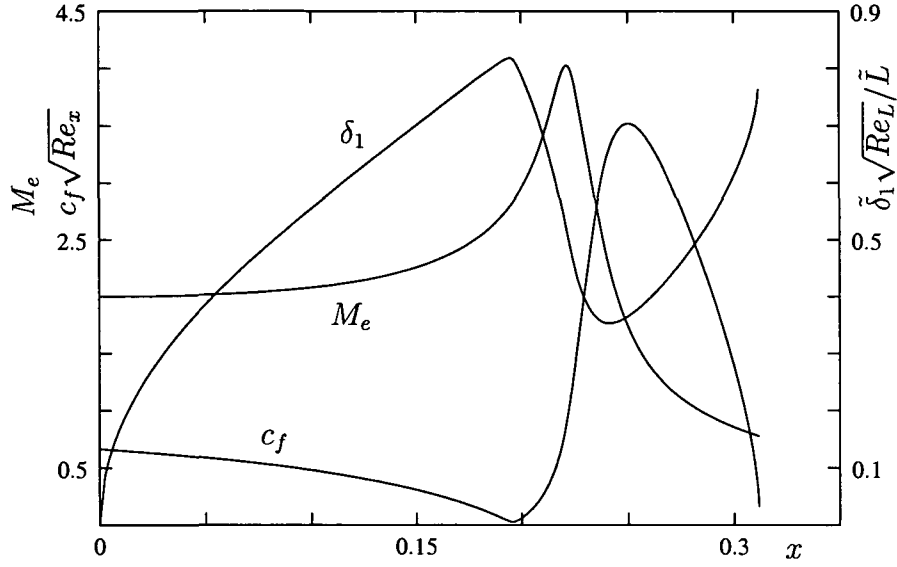


Figure 99: Numerical solution of the boundary layer equations for FC-71, $Ec = 0$, $T_{\infty r} = 1.001$, $\rho_{\infty r} = 0.17$ and $M_{\infty} = 2.0$.

3.2 Properties of a classical boundary layer near the point of vanishing wall shear stress

Introduction of the stream function

$$\frac{\partial \Psi}{\partial x} = -\rho V, \quad \frac{\partial \Psi}{\partial Y} = \rho u, \quad (3.6)$$

satisfies the continuity equation (1.13) and leads to the equation of motion in the x -direction (1.14) in the form

$$\begin{aligned} & \rho^2 \frac{\partial \Psi}{\partial Y} \frac{\partial^2 \Psi}{\partial x \partial Y} - \rho \frac{\partial \rho}{\partial x} \left(\frac{\partial \Psi}{\partial Y} \right)^2 - \rho^2 \frac{\partial \Psi}{\partial x} \frac{\partial^2 \Psi}{\partial Y^2} + \rho \frac{\partial \rho}{\partial Y} \frac{\partial \Psi}{\partial x} \frac{\partial \Psi}{\partial Y} \\ &= -\rho^3 \frac{dp}{dx} + \frac{\partial^3 \Psi}{\partial Y^3} \rho^2 \mu + \frac{\partial^2 \Psi}{\partial Y^2} \left(\rho^2 \frac{\partial \mu}{\partial Y} - 2\rho \frac{\partial \rho}{\partial Y} \right) \\ &+ \frac{\partial \Psi}{\partial Y} \left(2 \left(\frac{\partial \rho}{\partial Y} \right)^2 - \rho \frac{\partial \rho}{\partial Y} \frac{\partial \mu}{\partial Y} - \rho \frac{\partial^2 \rho}{\partial Y^2} \right) \end{aligned} \quad (3.7)$$

We now investigate the region where the wall shear stress has a local minimum (Figure 97) in more detail using asymptotic methods for $Ec = 0$ and in the limit $\Delta k \rightarrow 0^+$. The solution of the boundary layer equations is sought in the form

$$\Psi = \Psi_0(x, Y) + \Delta k \Psi_1(x, Y) + \dots, \quad (3.8)$$

$$\begin{aligned}
T &= T_0, \\
\rho &= \rho_0(x) + \Delta k \rho_1(x) + \cdots, \\
p &= p_0(x) + \Delta k p_1(x) + \cdots, \\
\mu &= \mu_0(x) + \Delta k \mu_1(x) + \cdots,
\end{aligned} \tag{3.9}$$

Inserting the expansions (3.8), (3.9) into the equation of motion (3.7) and collecting orders of Δk we obtain in first order

$$\rho_0 \frac{\partial \Psi_0}{\partial Y} \frac{\partial^2 \Psi_0}{\partial x \partial Y} - \frac{d\rho_0}{dx} \left(\frac{\partial \Psi_0}{\partial Y} \right)^2 - \rho_0 \frac{\partial \Psi_0}{\partial x} \frac{\partial^2 \Psi_0}{\partial Y^2} = -\rho_0^2 \frac{dp_0}{dx} + \frac{\partial^3 \Psi_0}{\partial Y^3} \rho_0 \mu_0, \tag{3.10}$$

and in second order

$$\begin{aligned}
& \frac{\partial \Psi_1}{\partial Y} \left(\rho_0^2 \frac{\partial^2 \Psi_0}{\partial x \partial Y} - 2\rho_0 \frac{d\rho_0}{dx} \frac{\partial \Psi_0}{\partial Y} \right) - \rho_0^2 \frac{\partial \Psi_1}{\partial x} \frac{\partial^2 \Psi_0}{\partial Y^2} \\
& + \rho_0^2 \frac{\partial^2 \Psi_1}{\partial x \partial Y} \frac{\partial \Psi_0}{\partial Y} - \rho_0^2 \frac{\partial^2 \Psi_1}{\partial Y^2} \frac{\partial \Psi_0}{\partial x} - \rho_0^2 \mu_0 \frac{\partial^3 \Psi_1}{\partial Y^3} \\
& + \rho_1 \left(2 \frac{d\rho_0}{dx} \left(\frac{\partial \Psi_0}{\partial Y} \right)^2 - \rho_0 \frac{\partial \Psi_0}{\partial Y} \frac{\partial^2 \Psi_0}{\partial x \partial Y} + \rho_0 \frac{\partial \Psi_0}{\partial x} \frac{\partial^2 \Psi_0}{\partial Y^2} \right) \\
& + \rho_1 \rho_0 \mu_0 \frac{\partial^3 \Psi_0}{\partial Y^3} - \rho_0 \left(\frac{\partial \Psi_0}{\partial Y} \right)^2 \frac{d\rho_1}{dx} - \rho_0^2 \frac{\partial^3 \Psi_0}{\partial Y^3} \mu_1 + \rho_0^3 \frac{dp_1}{dx} = 0
\end{aligned} \tag{3.11}$$

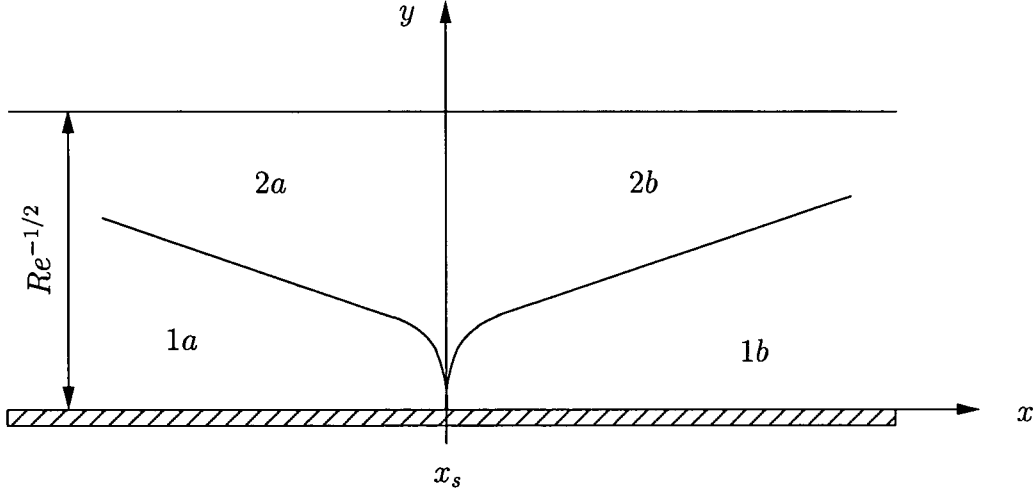


Figure 100: Asymptotic structure of the boundary layer close to the point of zero wall shear.

Following the work of Ruban [27] and Stewartson et al [30] the boundary layer region near the point of recovery is divided into a viscous wall region 1

and a predominantly inviscid outer region 2 as sketched in Figure 100. We first consider the viscous region 1a lying ahead of point of minimum wall shear and make a change of variables

$$s = x - x_s, \quad \eta = Y(-s)^{-1/4}, \quad (3.12)$$

where x_s is the point of minimum wall shear. In the limit $s \rightarrow 0^-$ the quantities $p_0, p_1, \rho_0, \rho_1, \mu_0, \mu_1$ in the equations (3.9) are expanded in the form of Taylor series

$$\begin{aligned} \frac{dp}{dx} &= p_{00} + sp_{01} + \cdots + \Delta k(p_{10} + sp_{11} + \cdots) + \cdots, \\ T &= T_0, \end{aligned} \quad (3.13)$$

$$\begin{aligned} \rho &= \rho_{00} + (-s)\rho_{01} + \cdots + \Delta k(\rho_{10} + (-s)\rho_{11} + \cdots) + \cdots, \\ \mu &= \mu_{00} + (-s)\mu_{01} + \cdots + \Delta k(\mu_{10} + (-s)\mu_{11} + \cdots) + \cdots, \end{aligned} \quad (3.14)$$

while $\Psi_0 = \Psi_{a0}$ is expanded as

$$\begin{aligned} \Psi_{a0} &= (-s)^\alpha f_{a00}(\eta) + (-s)^\beta f_{a01}(\eta) \\ &+ (-s)^\delta f_{a02}(\eta) + (-s)^{2\beta-\alpha} f_{a03}(\eta) + \cdots. \end{aligned} \quad (3.15)$$

It should be noted that -in the limiting case $Ec = 0$ considered here- the relations between the various coefficients in the expansions for the thermodynamical quantities (3.13), (3.14) are known from the equation of state and the equation of motion (Bernoulli equation) evaluated in the inviscid flow at the boundary layer edge. Further, the first term in the asymptotic expansion (3.15) is found by applying the no-slip condition (1.17) on the boundary layer equation in the x -direction (1.14). It follows that at any point on the surface

$$\frac{\rho}{\mu} \frac{dp}{dx} = \frac{\partial^3 \Psi}{\partial Y^3} \Big|_{Y=0}. \quad (3.16)$$

Applying the Goldstein similarity variables (3.12), the expansions for the thermodynamic quantities (3.13), (3.14) and integration then yields

$$\alpha = \frac{3}{4}, \quad f_{a00} = \frac{p_{00}\rho_{00}}{6\mu_{00}}\eta^3.$$

Substituting (3.13), (3.14), (3.15), into the equation of motion (3.10) and collecting terms of equal orders of s and taking into account the no-slip condition on the plate

$$\begin{aligned} f_{a01}(0) &= f_{a02}(0) = f_{a03}(0) = 0, \\ \frac{df_{a01}(0)}{d\eta} &= \frac{df_{a02}(0)}{d\eta} = \frac{df_{a03}(0)}{d\eta} = 0, \end{aligned} \quad (3.17)$$

we obtain ordinary differential equations for f_{a01} , f_{a02} and f_{a03} . At order $s^{\beta-3/4}$ we obtain the differential equation

$$\frac{d^3 f_{a01}(\eta)}{d\eta^3} - \frac{p_{00}\rho_{00}}{8\mu_{00}^2}\eta^3 \frac{d^2 f_{a01}(\eta)}{d\eta^2} + \frac{p_{00}\rho_{00}}{2\mu_{00}^2} \left(\frac{1}{4} + \beta\right) \eta^2 \frac{df_{a01}(\eta)}{d\eta} - \frac{p_{00}\rho_{00}}{\mu_{00}^2} \beta \eta f_{a01}(\eta) = 0.$$

Only one of the three linearly independent solutions found satisfies the boundary conditions (3.17)

$$f_{a01} = \frac{a_0}{2}\eta^2,$$

Here, a_0 is an arbitrary constant. Further, in order to determine the eigenvalue β it is necessary to consider the fourth term of the expansion (3.15) which satisfies the equation

$$\begin{aligned} \frac{d^3 f_{a03}(\eta)}{d\eta^3} - \frac{p_{00}\rho_{00}}{8\mu_{00}^2}\eta^3 \frac{d^2 f_{a03}(\eta)}{d\eta^2} + \frac{p_{00}\rho_{00}}{\mu_{00}^2} \left(\beta - \frac{1}{4}\right) \eta^2 \frac{df_{a03}(\eta)}{d\eta} \\ - \frac{p_{00}\rho_{00}}{\mu_{00}^2} \left(2\beta - \frac{3}{4}\right) \eta f_{a03}(\eta) = \frac{1}{4} (1 - 2\beta) a_0^2 \eta^2. \end{aligned}$$

The solution can be represented as a confluent hypergeometric function

$$f_{a03}(\eta) = \frac{a_0^2 \mu_{00}}{2p_{00}\rho_{00}}\eta + \frac{b_0}{2}\eta^2 + \eta^2 \int_0^\eta C_1 \eta^{-2} F\left(1 - 2\beta, \frac{5}{4}, \frac{p_{00}\rho_{00}}{32\mu_{00}^2}\eta^4\right) d\eta,$$

where C_1 , b_0 are arbitrary constants and

$$\begin{aligned} F\left(1 - 2\beta, \frac{5}{4}, \frac{p_{00}\rho_{00}}{32\mu_{00}^2}\eta^4\right) - 1 \\ = \sum_{k=1}^{\infty} \frac{(1 - 2\beta)(1 - 2\beta + 1) \cdots (1 - 2\beta + k - 1)}{\frac{5}{4} \left(\frac{5}{4} + 1\right) \cdots \left(\frac{5}{4} + k - 1\right) k!} \left(\frac{p_{00}\rho_{00}}{32\mu_{00}^2}\eta^4\right)^k, \end{aligned} \quad (3.18)$$

grows exponentially with η which will make matching with region 2a impossible unless we choose

$$\beta = \frac{m}{2}, \quad m = 1, 2, 3 \dots$$

for which the confluent hypergeometric function (3.18) reduces to a polynomial of degree m . In an asymptotic expansion such as (3.15) each term has to be of smaller order than the previous one and since the eigenvalue α is determined to $3/4$ already, (3.15) will only make sense if $\beta > 3/4$, i.e.

$$\beta = \frac{m}{2}, \quad m = 2, 3, 4 \dots$$

Choosing $m = 2$ yields the Goldstein singularity [15], [31]. So, the smallest possible eigenvalue is

$$m = 3 \quad (3.19)$$

which yields

$$\beta = \frac{3}{2},$$

After determining the constant C_1 from the no slip condition, we get

$$f_{a03} = \frac{b_0}{2}\eta^2 - \frac{a_0^2}{5!}\eta^5 + \frac{a_0^2 p_{00} \rho_{00}}{8! \mu_{00}^2} \eta^9.$$

We now turn to the third term of the expansion for Ψ_{a0} (3.15) which is related to the linear terms in the expansions for the pressure (3.13), density and viscosity (3.14). The only possible choice of the eigenvalue δ for which the solutions f_{a01} , f_{a03} are left unchanged is $7/4$. So, at order s^1 we obtain the differential equation for f_{a02} , i.e.

$$\begin{aligned} \frac{d^3 f_{a02}(\eta)}{d\eta^3} - \frac{p_{00} \rho_{00}}{8 \mu_{00}^2} \eta^3 \frac{d^2 f_{a02}(\eta)}{d\eta^2} + \frac{p_{00} \rho_{00}}{\mu_{00}^2} \eta^2 \frac{df_{a02}(\eta)}{d\eta} - \frac{7 p_{00} \rho_{00}}{\mu_{00}^2} \eta f_{a02}(\eta) \\ = \frac{p_{00}^2 \rho_{00} \rho_{01}}{4 \mu_{00}^3} \eta^4 + \frac{p_{00} \rho_{00}}{\mu_{00}} \left(\frac{p_{01}}{p_{00}} + \frac{\rho_{01}}{\rho_{00}} + \frac{\mu_{01}}{\mu_{00}} \right) \end{aligned}$$

which is satisfied by

$$f_{a02} = d_0 \eta^2 + \frac{\rho_{00} p_{00}}{6 \mu_{00}} \left(\frac{\rho_{01}}{\rho_{00}} + \frac{p_{01}}{p_{00}} - \frac{\mu_{01}}{\mu_{00}} \right) \eta^3 + \frac{2 \rho_{00}^2 p_{00}^2}{7! \mu_{00}^3} \left(2 \frac{\rho_{01}}{\rho_{00}} - \frac{p_{01}}{p_{00}} + \frac{\mu_{01}}{\mu_{00}} \right) \eta^7,$$

where d_0 is an arbitrary constant.

Summarising, the results obtained so far for region 1a are:

$$\begin{aligned} \Psi_{a0} &= (-s)^{3/4} f_{a00}(\eta) + (-s)^{3/2} f_{a01}(\eta) + (-s)^{7/4} f_{a02}(\eta) + (-s)^{9/4} f_{a03}(\eta) + \dots \\ f_{a00} &= \frac{p_{00} \rho_{00}}{6 \mu_{00}} \eta^3, \\ f_{a01} &= \frac{a_0}{2} \eta^2, \\ f_{a02} &= d_0 \eta^2 + \frac{\rho_{00} p_{00}}{6 \mu_{00}} \left(\frac{\rho_{01}}{\rho_{00}} + \frac{p_{01}}{p_{00}} - \frac{\mu_{01}}{\mu_{00}} \right) \eta^3 \\ &\quad + \frac{2 \rho_{00}^2 p_{00}^2}{7! \mu_{00}^3} \left(2 \frac{\rho_{01}}{\rho_{00}} - \frac{p_{01}}{p_{00}} + \frac{\mu_{01}}{\mu_{00}} \right) \eta^7, \\ f_{a03} &= \frac{b_0}{2} \eta^2 - \frac{a_0^2}{5!} \eta^5 + \frac{a_0^2 p_{00} \rho_{00}}{8! \mu_{00}^2} \eta^9. \end{aligned} \quad (3.20)$$

Next we examine region 2a where $Y = O(1)$. Rewriting the solution of region 1a (3.20) in the variables of region 2a, suggests the expansion

$$\Psi_{2a0} = f_{2a00}(Y) + (-s)f_{2a01}(Y) + \dots, s \rightarrow 0^-. \quad (3.21)$$

Substitution into (3.10) yields that $f_{2a00}(Y)$ remains arbitrary, i.e. cannot be obtained from local analysis and

$$f_{2a01} = \frac{df_{2a00}(Y)}{dY} \left[c_0 + \int_0^Y \left(\frac{p_{00}\rho_{00} - \frac{d^3 f_{2a00}(Y)}{dY^3} \mu_{00}}{\left(\frac{df_{2a00}(Y)}{dY} \right)^2} + \frac{\rho_{01}}{\rho_{00}} \right) dY \right] \quad (3.22)$$

where c_0 is an arbitrary constant. The behaviour of the function f_{2a00} for $Y \rightarrow 0$ and c_0 are determined by matching with the results (3.20) holding in region 1a. We obtain

$$\begin{aligned} f_{2a00} &= \frac{p_{00}\rho_{00}}{6\mu_{00}} Y^3 + \frac{2p_{00}^2\rho_{00}^2}{7!\mu_{00}^3} \left(2\frac{\rho_{01}}{\rho_{00}} - \frac{p_{01}}{p_{00}} + \frac{\mu_{01}}{\mu_{00}} \right) Y^7 \\ &+ \frac{p_{00}\rho_{00}a_0^2}{8!\mu_{00}^2} Y^9 + \dots, \quad Y \rightarrow 0, \\ f_{2a01} &= \frac{a_0}{2} Y^2 + \frac{p_{00}\rho_{00}}{6\mu_{00}} \left(\frac{\rho_{01}}{\rho_{00}} + \frac{p_{01}}{p_{00}} - \frac{\mu_{01}}{\mu_{00}} \right) Y^3 \\ &- \frac{a_0^2}{5!} Y^5 + \dots, \quad Y \rightarrow 0, \end{aligned} \quad (3.23)$$

Further we seek an extension of the solution beyond the point of zero wall shear stress. Starting in the region 1b we try the asymptotic expansion, [31]

$$\begin{aligned} \Psi_{b0} &= s^{3/4} f_{b00}(\xi) + s^{3/2} f_{b01}(\xi) + s^{7/4} f_{b02}(\xi) + s^{9/4} f_{b03}(\xi) + \dots, \\ \xi &= Y s^{-1/4} = O(1), \quad s \rightarrow 0^+. \end{aligned} \quad (3.24)$$

Imposing the no-slip condition on the surface of the plate

$$\begin{aligned} f_{b00}(0) &= f_{b01}(0) = f_{b02}(0) = f_{b03}(0) = 0, \\ \frac{df_{b00}(0)}{d\xi} &= \frac{df_{b01}(0)}{d\xi} = \frac{df_{b02}(0)}{d\xi} = \frac{df_{b03}(0)}{d\xi} = 0, \end{aligned}$$

we obtain

$$\begin{aligned}
f_{b00} &= \frac{p_{00}\rho_{00}}{6\mu_{00}}\xi^3, \\
f_{b01} &= \frac{a_0^*}{2}\xi^2, \\
f_{b02} &= d_0^*\xi^2 - \frac{p_{00}\rho_{00}}{6\mu_{00}}\left(\frac{\rho_{01}}{\rho_{00}} + \frac{p_{01}}{p_{00}} - \frac{\mu_{01}}{\mu_{00}}\right)\xi^3 \\
&\quad + \frac{2p_{00}^2\rho_{00}^2}{7!\mu_{00}^3}\left(2\frac{\rho_{01}}{\rho_{00}} - \frac{p_{01}}{p_{00}} + \frac{\mu_{01}}{\mu_{00}}\right)\xi^7, \\
f_{b03} &= \frac{b_0^*}{2}\xi^2 + \frac{a_0^{*2}}{5!}\xi^5 + \frac{a_0^{*2}p_{00}\rho_{00}}{8!\mu_{00}^2}\xi^9.
\end{aligned} \tag{3.25}$$

using arguments similar to those applied in the derivation of the solution for region 1a.

Finally, in region 2b where $Y = O(1)$ the solution is sought in the form

$$\Psi_{2b0} = f_{2b00}(Y) + sf_{2b01}(Y) + \dots, s \rightarrow 0^+, \tag{3.26}$$

which from (3.10) yields

$$f_{2b01} = \frac{df_{2b00}(Y)}{dY} \left[c_0^* + \int_0^Y \left(\frac{\frac{d^3 f_{2b00}(Y)}{dY^3} \mu_{00} - p_{00}\rho_{00}}{\left(\frac{df_{2b00}(Y)}{dY} \right)^2} - \frac{\rho_{01}}{\rho_{00}} \right) dY \right]. \tag{3.27}$$

After matching with the results (3.24) obtained in region 1b we get

$$\begin{aligned}
f_{2b00} &= f_{2a00} = \frac{p_{00}\rho_{00}}{6\mu_{00}}Y^3 + \frac{2\rho_{00}^2p_{00}^2}{7!\mu_{00}^3}\left(2\frac{\rho_{01}}{\rho_{00}} - \frac{p_{01}}{p_{00}} + \frac{\mu_{01}}{\mu_{00}}\right)Y^7 \\
&\quad + \frac{a_0^{*2}p_{00}\rho_{00}}{8!\mu_{00}^2}Y^9 + \dots, \quad Y \rightarrow 0, \\
f_{2b01} &= \frac{a_0^*}{2}Y^2 - \frac{p_{00}\rho_{00}}{6\mu_{00}}\left(\frac{\rho_{01}}{\rho_{00}} + \frac{p_{01}}{p_{00}} - \frac{\mu_{01}}{\mu_{00}}\right)Y^3 \\
&\quad + \frac{a_0^{*2}}{5!}Y^5 + \dots, \quad Y \rightarrow 0.
\end{aligned} \tag{3.28}$$

It now remains to match the solutions in region 1a (3.15) and in region 1b (3.24). Writing (3.24) in the variables of region 1a yields the relationship

$$a_0^{*2} = a_0^2. \tag{3.29}$$

which depends crucially on the choice of the eigenvalue (3.19). If we had chosen the first eigenvalue, $m = 2$, we would have obtained $a_0^{*2} = -a_0^2$ instead and as a consequence a real solution downstream of the point of zero friction is impossible to find unless $a_0 = 0$. The relation (3.29) gives us two possibilities to choose a_0^* . The first one, $a_0^* = a_0$, yields a discontinuity in the angle of inclination of the streamlines at the point $s = 0$ and thus represents the marginal separation singularity. The second possibility, $a_0^* = -a_0$, provides a smooth behaviour through the point of zero wall shear. The stream function is represented by

$$\begin{aligned}\Psi_{2a0} = \Psi_{2b0} = & f_{2a00}(Y) + s \frac{df_{2a00}(Y)}{dY} \int_0^Y \left(\frac{\frac{d^3 f_{2b00}(Y)}{dY^3} \mu_{00} - p_{00} \rho_{00}}{\left(\frac{df_{2b00}(Y)}{dY} \right)^2} - \frac{\rho_{01}}{\rho_{00}} \right) dY \\ & - s \frac{df_{2a00}(Y)}{dY} \frac{a_0 \mu_{00}}{p_{00} \rho_{00}} + \dots,\end{aligned}$$

which is valid in the vicinity of $s = 0$. In the limit $Y \rightarrow 0$ we obtain

$$\begin{aligned}\Psi_{2a0} = \Psi_{2b0} = & \frac{p_{00} \rho_{00}}{6 \mu_{00}} Y^3 + \frac{2 \rho_{00}^2 p_{00}^2}{7! \mu_{00}^3} \left(2 \frac{\rho_{01}}{\rho_{00}} - \frac{p_{01}}{p_{00}} + \frac{\mu_{01}}{\mu_{00}} \right) Y^7 \\ & + \frac{a_0^2 p_{00} \rho_{00}}{8! \mu_{00}^2} Y^9 + s \left[-\frac{a_0}{2} Y^2 \right. \\ & \left. - \frac{p_{00} \rho_{00}}{6 \mu_{00}} \left(\frac{\rho_{01}}{\rho_{00}} + \frac{p_{01}}{p_{00}} - \frac{\mu_{01}}{\mu_{00}} \right) Y^3 + \frac{a_0^2}{5!} Y^5 + \dots \right] + \dots.\end{aligned}\quad (3.30)$$

From (3.30) the skin friction is calculated, i.e.

$$\tau = \left. \frac{\partial^2 \Psi}{\partial Y^2} \right|_{Y=0} = -a_0 s + O(s^2).$$

We will now examine the case where Δk slightly differs from 0. Starting in region 1a, the solution for (3.11) is sought in the form

$$\Psi_{a1} = (-s)^\gamma f_{a10}(\eta) + (-s)^{\gamma+3/4} f_{a11}(\eta) + \dots \quad (3.31)$$

Substituting (3.31) into (3.11) and collecting orders of s yields

$$\begin{aligned}\gamma &= -1/2, \\ f_{a10} &= \frac{a_1}{2} \eta^2, \\ f_{a11} &= \frac{b_1}{2} \eta^2.\end{aligned}\quad (3.32)$$

This was obtained in the same manner as the first order solution Ψ_{a0} in region 1a and the eigenvalue $\gamma = -1/2$ is the first possible eigenvalue which eliminates the exponential growth of the confluent hypergeometrical function satisfying the differential equation for f_{a10} . On the other side of $s = 0$, i.e. region 1b, the solution is found in exactly the same way to be

$$\Psi_{b1} = s^{-1/2} \frac{a_1^*}{2} \xi^2 + s^{1/4} \frac{b_1^*}{2} \xi^2 + \dots \quad (3.33)$$

In region 2a where $Y = O(1)$ the solution is represented by the asymptotic expansion

$$\Psi_{2a1} = (-s)^{-1} f_{2a10}(Y) + (-s)^{-1/4} f_{2a11}(Y) + \dots, s \rightarrow 0^-, \quad (3.34)$$

which is found by writing the results of region 1a (3.31) in the variables of region 2a. Substituting (3.34) into the equation of motion of the second order (3.11) yields

$$\Psi_{2a1} = (-s)^{-1} \frac{a_1 \mu_{00}}{p_{00} \rho_{00}} \frac{df_{2a00}(Y)}{dY} + O((-s)^{-1/4}). \quad (3.35)$$

Similarly, the solution in region 2b is given by

$$\Psi_{2b1} = s^{-1} \frac{a_1^* \mu_{00}}{p_{00} \rho_{00}} \frac{df_{2a00}(Y)}{dY} + O(s^{-1/4}). \quad (3.36)$$

According to the definition of asymptotic expansions, each term has to be of smaller order than the previous one. This is not satisfied in (3.34) where the first term increases without bound as $s \rightarrow 0^-$. Therefore, we must examine the immediate neighbourhood of the point $s = 0$ separately on the basis of the full Navier-Stokes equations.

3.3 Local Interaction process

The first task to complete in the analysis close to the point $s = 0$ is to find the magnitude of the region where the pressure induced due to the displacement effect p_i becomes large enough to influence the flow in the first order. The theory of small perturbations for two-dimensional supersonic flows yields the Ackeret formula [1]

$$p_i - p \sim \frac{1}{\sqrt{M^2 - 1}} \frac{\tilde{v}}{\tilde{u}}. \quad (3.37)$$

Further, the angle of inclination Θ , describing the slope of the streamlines is defined as

$$\frac{\tilde{v}}{\tilde{u}} = \tan \Theta \sim \Theta. \quad (3.38)$$

Substituting the solution of region 1a (3.20) into (3.38) one obtains the estimate

$$\Theta \sim -Re^{-1/2}(-s)^{1/4} \left(\frac{\partial \Psi_{a0}}{\partial \eta} \right)^{-1} \left(\frac{\partial \Psi_{a0}}{\partial s} + \frac{1}{4}(-s)^{-1} \eta \frac{\partial \Psi_{a0}}{\partial \eta} \right). \quad (3.39)$$

Applying Taylor series expansions around $s = 0$ for the denominator in the expression (3.39) yields

$$\Theta = -Re^{-1/2} \left(\frac{a_0 \mu_{00}}{p_{00} \rho_{00}} \text{sign}(s) + O((-s)^{3/4}) \right). \quad (3.40)$$

We then plug the expressions (3.38), (3.40) into the Ackeret formula (3.37) and differentiate once in the x -direction, i.e.

$$\frac{dp_i}{dx} = O \left(\frac{Re^{-1/2}}{x - x_s} \right). \quad (3.41)$$

The relation (3.41) grows unbounded as $x \rightarrow x_s$ which indicates the need of an interaction region. Further, in order to affect the wall shear stress the induced pressure gradient has to be of the same order of magnitude as the fourth eigenfunction of the solution in the viscous region 1a (3.15), i.e.

$$\frac{\partial^3 \Psi_{a0}}{\partial Y^3} = \frac{p_{00} \rho_{00}}{\mu_{00}} + (-s)^{3/4} \frac{\partial^3 f_{a01}}{\partial Y^3} + (-s) \frac{\partial^3 f_{a02}}{\partial Y^3} + (-s)^{3/2} \frac{\partial^3 f_{a03}}{\partial Y^3} + \dots$$

The two quantities will be of comparable size if

$$|x - x_s| = O(Re^{-1/5}). \quad (3.42)$$

With the objective to construct uniform valid asymptotic solution, Δk is chosen to

$$\Delta k = O(|x - x_s|^2) = O(Re^{-2/5}). \quad (3.43)$$

Then, the first eigenfunction of Ψ_{a1} (3.32) becomes comparable in order of magnitude to the second eigenfunction of Ψ_{a0} (3.20) and the asymptotic breakdown in (3.34) is avoided.

We go back to the full Navier-Stokes equations (1.8), (1.9) where the streamfunction is defined as

$$\frac{\partial \psi}{\partial x} = -\rho v, \quad \frac{\partial \psi}{\partial y} = \rho u,$$

and adopt a new scaling in the x -direction according to (3.42)

$$s_* = Re^{1/5}(x - x_s). \quad (3.44)$$

Further, a term is added to the expansion for pressure of the order $Re^{-3/10}$ which accounts for the local interaction between the boundary layer and the external flow, i.e. accounts for the pressure response of the external flow caused by the rapidly changing boundary layer displacement thickness.

$$\frac{\partial p}{\partial x} = p_{00} + Re^{-1/5} s_* p_{01} + Re^{-3/10} \frac{dp_*}{ds_*} + \dots \quad (3.45)$$

Inserting (3.42) into (3.12) we immediately obtain the thickness of the lower

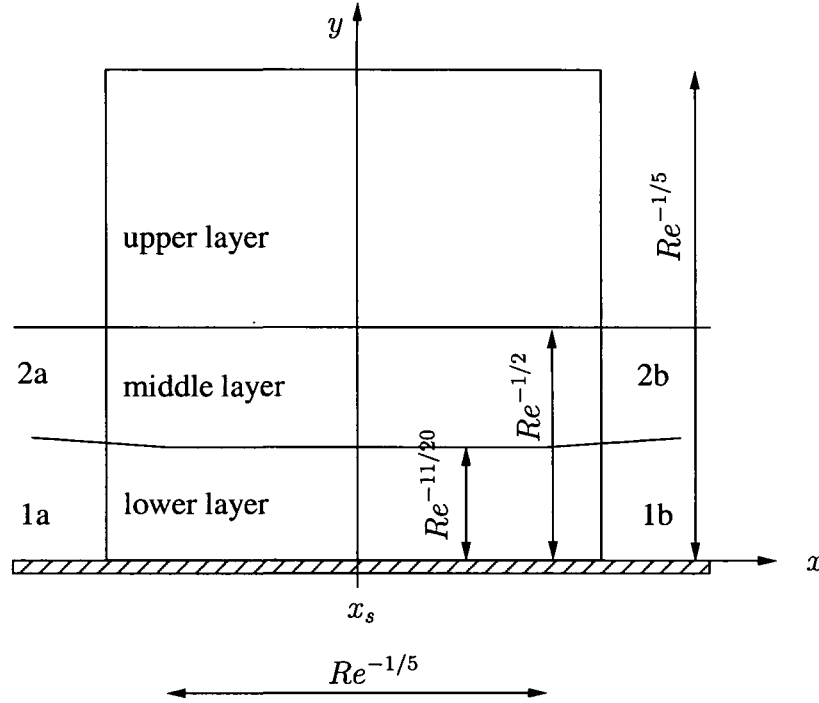


Figure 101: The triple deck structure in the interaction region.

layer in the interaction region (Figure 101). The lateral extent of the upper layer is found from potential theory which requires that the scaling in x -, and y -direction must be of the same order.

The analysis of the interaction region is commenced in the middle layer where the Navier-Stokes equations are investigated on the basis of the limit process

$$s_* = Re^{1/5}(x - x_s) = O(1), \quad Y = O(1), \quad Re \rightarrow \infty, \quad Ec = 0. \quad (3.46)$$

Writing the results of region 2a (3.23) in the variables of the middle layer (3.46) and considering (3.43) suggests that the streamfunction $\psi = \psi_2$ can be expanded as

$$\psi_2(s_*, Y) = Re^{-1/2} \psi_{20}(Y) + Re^{-7/10} \psi_{21}(s_*, Y) + \dots \quad (3.47)$$

Together with the thermodynamical expansions (3.14), (3.45) inserted in the first Navier-Stokes equation (1.8) we obtain expressions of different orders of Re . Collecting these yields a system of equations which are satisfied for

$$\begin{aligned}\psi_{20}(Y) &= f_{2a00}(Y), \\ \psi_{21}(s_*, Y) &= \frac{df_{2a00}(Y)}{dY} \frac{\mu_{00}}{p_{00}\rho_{00}} A_1(s_*) \\ &+ s_* \frac{df_{2a00}(Y)}{dY} \int_0^Y \left(\frac{\frac{d^3 f_{2a00}(Y)}{dY^3} \mu_{00} - p_{00}\rho_{00}}{\left(\frac{df_{2a00}(Y)}{dY}\right)^2} - \frac{\rho_{01}}{\rho_{00}} \right) dY\end{aligned}\quad (3.48)$$

where $A_1(s_*)$ is an arbitrary function. By matching (3.48) with the results holding in region 2a we obtain its behaviour far upstream

$$A_1(s_*) = a_0(-s_*) + a_1 k_1(-s_*)^{-1} + \dots, \text{ as } s_* \rightarrow -\infty.$$

Inserting (3.47), (3.14), (3.45) into the second Navier-Stokes equation (1.9) we get

$$\frac{\partial}{\partial Y} \left(\frac{\partial p_*}{\partial s_*} \right) = 0. \quad (3.49)$$

Next, we turn to the lower layer where the Navier-Stokes equations are analysed in the limit

$$s_* = Re^{1/5}(x - x_s) = O(1), \quad y_3 = Re^{11/20}y = O(1), \quad Re \rightarrow \infty, \quad Ec = \mathfrak{B}.50$$

Writing the results of region 1a (3.20), (3.32) in the variables of the lower layer (3.50) and considering (3.43) suggests that the streamfunction $\psi = \psi_3$ can be expanded as

$$\begin{aligned}\psi_3(s_*, y_3) &= Re^{-13/20}\psi_{30}(y_3) + Re^{-16/20}\psi_{31}(s_*, y_3) + \\ &Re^{-17/20}\psi_{32}(s_*, y_3) + Re^{-19/20}\psi_{33}(s_*, y_3) + \dots\end{aligned}\quad (3.51)$$

Together with the thermodynamical expansions (3.9), (3.45) in the first Navier-Stokes equation (1.8), one obtains for the first three terms

$$\psi_{30}(y_3) = \frac{p_{00}\rho_{00}}{6\mu_{00}} y_2^3, \quad (3.52)$$

$$\psi_{31}(s_*, y_3) = \frac{1}{2} A_1(s_*) y_3^2, \quad (3.53)$$

$$\begin{aligned}\psi_{32}(s_*, y_3) &= \frac{\rho_{00}p_{00}}{6\mu_{00}} \left(\frac{\rho_{01}}{\rho_{00}} + \frac{p_{01}}{p_{00}} - \frac{\mu_{01}}{\mu_{00}} \right) y_2^3(-s_*) \\ &+ \frac{2\rho_{00}^2 p_{00}^2}{7!\mu_{00}^3} \left(2\frac{\rho_{01}}{\rho_{00}} - \frac{p_{01}}{p_{00}} + \frac{\mu_{01}}{\mu_{00}} \right) y_3^7,\end{aligned}\quad (3.54)$$

where $A_1(s_*)$ is the arbitrary function entering (3.48). In order to determine it, it is necessary to examine the problem for ψ_{33}

$$\begin{aligned} \frac{\partial^3 \psi_{33}(s_*, y_3)}{\partial y_3^3} - \frac{p_{00}\rho_{00}}{2\mu_{00}^2} y_3^2 \frac{\partial^2 \psi_{33}(s_*, y_3)}{\partial y_3 \partial s_*} + \frac{p_{00}\rho_{00}}{\mu_{00}^2} y_3 \frac{\partial \psi_{33}(s_*, y_3)}{\partial s_*} \\ = \frac{\rho_{00}}{\mu_{00}} \frac{dp_*}{ds_*} + \frac{1}{2} y_3^2 A_1(s_*) \frac{dA_1(s_*)}{ds_*}, \end{aligned} \quad (3.55)$$

The boundary conditions require

$$\psi_{33}(s_*, 0) = \frac{\partial \psi_{33}(s_*, 0)}{\partial y_3} = 0.$$

Note that the boundary-value problem (3.55) is not closed, because of the term dp_*/ds_* . Before giving (3.55) more attention, we substitute the asymptotic expansions (3.51), (3.9), (3.45) into the second Navier-Stokes equation (1.9) and obtain

$$\frac{\partial}{\partial Y} \left(\frac{\partial p_*}{\partial s_*} \right) = 0.$$

To close the problem (3.55) we have to determine the pressure gradient dp_*/ds_* from the solution of the problem for the upper layer of potential flow. The solution in the middle layer (3.47), (3.48) yields the slope of the streamlines in region 2:

$$\Theta(s_*) = -Re^{-1/2} \frac{\mu_{00}}{p_{00}\rho_{00}} \frac{dA_1(s_*)}{ds_*}. \quad (3.56)$$

The relation (3.56) depends only on s_* and is, therefore, valid also at the bottom of region 1. Introducing the stretched streamline slope $\Theta_*(s_*) = Re^{1/2}\Theta(s_*)$ it can also be written in the form

$$\Theta_*(s_*) = \frac{\mu_{00}}{p_{00}\rho_{00}} \frac{dA_1(s_*)}{ds_*}. \quad (3.57)$$

In the upper layer the longitudinal and transverse variables of order unity will be

$$s_* = Re^{1/5}(x - x_s), \quad y_1 = Re^{1/5}y, \quad (3.58)$$

and appropriate expansions of the field quantities are

$$\begin{aligned} u &= u_{00} + \dots + Re^{-1/2}u_{01} + \dots, \\ v &= Re^{-1/2}v_{01} + \dots, \\ \rho &= \rho_{00} + \dots + Re^{-1/2}\rho_{01} + \dots, \\ T &= T_{00} + \dots + Re^{-1/2}T_{01} + \dots, \\ p &= p_{00} + \dots + Re^{-1/2}p_{01} + \dots, \end{aligned} \quad (3.59)$$

where $u_{00}, \rho_{00}, T_{00}, p_{00}$ and dots \dots denote the non-interactive part of the flow field.

Plugging (3.59) into the governing equations leads to equations for the disturbances induced by the local interaction process which are linearised with respect to the non-interactive flow quantities evaluated at $x = x_s, y_1 = 0$. Matching of the solutions to those holding inside the main deck region then yields the result - anticipated before - that $p_*(s_*)$ and $\Theta_*(s_*)$ satisfy the Ackeret relationship

$$p_*(s_*) = \frac{1}{\sqrt{M_{00}^2 - 1}} \Theta_*(s_*), \quad (3.60)$$

Combination of (3.60) and (3.57) finally yields the interaction equation:

$$\frac{dp_*}{ds_*} = \frac{u_{00}\mu_{00}}{p_{00}\sqrt{M_{00}^2 - 1}} \frac{d^2 A_1(s_*)}{ds_*^2}, \quad (3.61)$$

where M_{00} denotes the value of the Mach number at the point $x = x_s$. The relation (3.61) between the induced pressure and displacement effect closes the interaction problem (3.55). It is convenient to recast (3.55) into a form containing a single control parameter λ . To this end we write

$$\begin{aligned} \psi_{33}(s_*, y_3) &= \frac{a_0^2 p_{00} \rho_{00}}{8! \mu_{00}^2} y_3^9 + \frac{a_0^2}{5!} s_* y_3^5 + \frac{A_2(s_*)}{2} y_3^2 G(s_*, y_3) \\ &+ \left(\frac{\mu_{00} A_1^2(s_*)}{2 p_{00} \rho_{00}} - \frac{k_1 a_0 a_1 \mu_{00}}{p_{00} \rho_{00}} - \frac{a_0^2 \mu_{00}^2}{2 p_{00} \rho_{00}} s_*^2 \right) y_3, \end{aligned} \quad (3.62)$$

and introduce the affine transformations

$$\begin{aligned} G(s_2, y_2) &= \frac{u_{00}^{9/10} a_0^{11/10} \mu_{00}^{41/20} \rho_{00}^{1/10}}{p_{00}^{17/10} (M_0^2 - 1)^{9/20}} \hat{G}(\hat{X}, \hat{Y}) \\ y_3 &= \frac{u_{00}^{1/10} \mu_{00}^{9/20}}{a_0^{1/10} p_{00}^{3/10} \rho_{00}^{1/10} (M_0^2 - 1)^{1/20}} \hat{Y} \\ s_* &= \frac{u_{00}^{2/5} \rho_{00}^{3/5}}{a_0^{2/5} p_{00}^{1/5} \mu_{00}^{1/5} (M_0^2 - 1)^{1/5}} \hat{X} \\ A_1(s_*) &= \frac{u_{00}^{2/5} a_0^{3/5} \rho_{00}^{3/5} \mu_{00}^{3/10}}{p_{00}^{1/5} (M_0^2 - 1)^{1/5}} \hat{A}(\hat{X}). \end{aligned} \quad (3.63)$$

One then obtains

$$\begin{aligned} \frac{\partial^3 \hat{G}(\hat{X}, \hat{Y})}{\partial \hat{Y}^3} - \frac{\hat{Y}^2}{2} \frac{\partial^2 \hat{G}(\hat{X}, \hat{Y})}{\partial \hat{Y} \partial \hat{X}} + \hat{Y} \frac{\partial \hat{G}(\hat{X}, \hat{Y})}{\partial \hat{X}} &= -\frac{d^2 \hat{A}(\hat{X})}{d\hat{X}^2}, \\ \hat{G}(\hat{X}, 0) &= 0, \\ \frac{\partial \hat{G}(\hat{X}, 0)}{\partial \hat{Y}} &= -\frac{1}{2} \left(\hat{A}^2(\hat{X}) - \hat{X}^2 + 2\lambda \right), \end{aligned} \quad (3.64)$$

where the control parameter

$$\lambda = k_1 \frac{(-a_1) p_{00}^{2/5} (M_0^2 - 1)^{2/5}}{a_0^{1/5} u_{00}^{4/5} \rho_{00}^{6/5} \mu_{00}^{3/5}}. \quad (3.65)$$

characterises the deviation of the free stream density from its critical value. The general form of the problem (3.64) is treated in detail by Stewartson [29] (see also Hackmüller [16]). As shown there using Fourier transformation, an exponential growing solution as $\hat{Y} \rightarrow \infty$ can be avoided only if

$$\begin{aligned} \hat{A}^2(\hat{X}) + 2\lambda - \hat{X}^2 &= C \int_{-\infty}^{\hat{X}} \frac{d^2 \hat{A}(\xi)}{d\xi^2} (\hat{X} - \xi)^{-1/2} d\xi, \\ C &= \frac{\Gamma(3/4)}{2^{3/2} \Gamma(5/4)}, \end{aligned} \quad (3.66)$$

subjected to the asymptotic boundary conditions

$$\hat{A}^2(\hat{X}) + 2\lambda - \hat{X}^2 = \begin{cases} \frac{3}{2} C \pi \lambda (-\hat{X})^{-5/2} & \text{as } \hat{X} \rightarrow -\infty, \\ -4C \hat{X}^{-1/2} & \text{as } \hat{X} \rightarrow \infty. \end{cases} \quad (3.67)$$

Equation (3.66) for $\hat{A}(\hat{X})$ is commonly called the fundamental equation of marginal-separation theory. In contrast to the studies done by Ruban [28], Stewartson et al [30] where the induced pressure gradient depends on the Hilbert integral and, therefore, the right hand side of the fundamental equation is to be integrated from \hat{X} to ∞ , the integration limits in (3.66) ranges from $-\infty$ to \hat{X} .

Figure 102 displays four numerical solutions of the fundamental equation for different values of λ for which classical boundary layer theory fails due to the occurrence of a Goldstein singularity. The physical interpretation of $\hat{A}(\hat{X})$ is found by differentiating (3.51) twice,

$$\tau = \frac{\partial^2 \psi}{\partial y^2} \Big|_{y=0} = Re^{3/10} \frac{u_{00}^{2/5} a_0^{3/5} \rho_{00}^{3/5} \mu_{00}^{3/10}}{p_{00}^{1/5} (M_0^2 - 1)^{1/5}} \hat{A}(\hat{X}) + \dots, \quad (3.68)$$

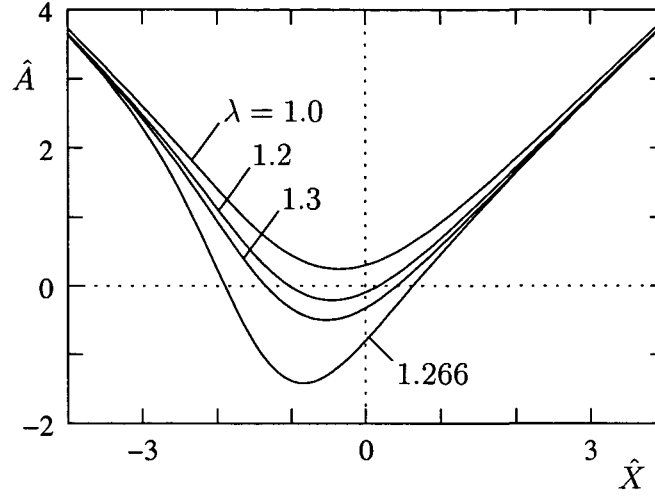


Figure 102: Numerical solution of $\hat{A}(\hat{X})$ for various values of the controlling parameter $\lambda \propto Re^{2/5} k_1$.

i.e. a measure of the wall shear stress. Therefore, the boundary layer remains attached for the smallest value of λ while a short region of reversed flow indicates the occurrence of marginal separation for the three other values of λ . Further, the solutions presented in Figure 102 are the mirror images of the solutions to those obtained in the studies from Ruban [28], Stewartson et al [30] with the exception that here, Δk is proportional to the free stream density deviation from its critical value whereas in [28], [30] Δk is proportional to the change in angle of attack. Figure 103 displays the difference between marginal separation theory and classical, i.e. hierarchical, boundary layer theory. The variations of the wall shear stress for the latter are found by setting the induced pressure gradient appearing in (3.55) to zero. Applying the affine transformations (3.63) then reduce the solvability condition to

$$\hat{A}(\hat{X}) = \sqrt{\hat{X}^2 - 2\lambda}.$$

The interaction between the boundary layer and the inviscid outer flow in the theory of marginal separation causes a slower progress in the development of the wall shear stress. For the case where $\lambda = 0$ and classical boundary layer theory experiences a marginal separation singularity, the interaction causes the wall shear stress to remain positive and continuous throughout the interaction region. An increase in λ causes the occurrence of a Goldstein singularity in the Prandtl boundary layer equations whereas the theory of marginal separation allows the formation of a small region with recirculating flow.

It should be noted that the smallest value of \hat{A} , in Figure 102, is not given for the largest number of λ which calls for a more convenient way to illustrate the

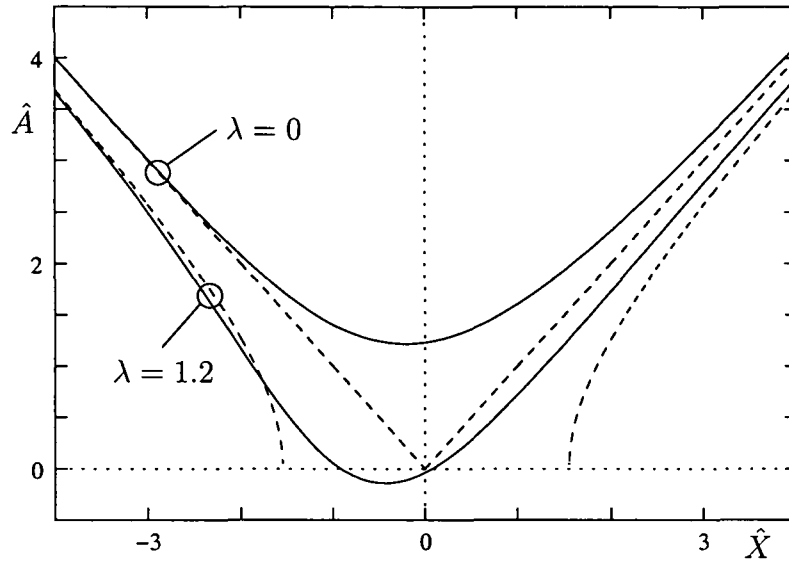


Figure 103: Comparison between marginal separation theory and classical boundary layer theory (dashed).

behaviour of \hat{A} . This is done in Figure 104, which often is referred to as the fundamental curve, where $\hat{A}(0)$ is plotted as a function of λ . As can be seen is the flow behaviour non-unique. Starting in the point Q and moving along the fundamental curve in the direction of the arrows the skin friction decreases with increasing λ . The flow is attached until $\lambda_s \approx 1.14$ is reached where separation occurs. Between λ_s and λ_c both our solutions indicate the existence of a local zone of reversed flow. For values of λ larger than $\lambda_c \approx 1.33$ the fundamental equation does not have a (real) solution. For $\lambda > \lambda_c$ it is appropriate to leave the limitation of steady flows and seek the solution to the unsteady problem. This transition from one class of flows to another is followed by a phenomena called short-bubble bursting [4].

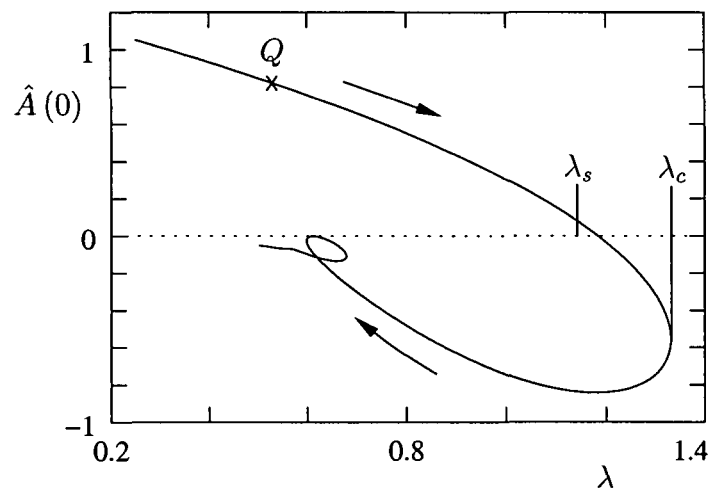


Figure 104: The fundamental curve showing non-uniqueness of flow.

4 Conclusions

Mechanical engineering is a broad field of science. In this PhD thesis the opportunity was given to combine thermodynamics, fluid mechanics and modern analytical and numerical mathematical methods to study the unusual behaviour of Bethe-Zel'dovich-Thompson fluids known as dense gases with complex molecular structures. Earlier work showed that BZT-fluids may behave opposite to the intuition gained from the theory of perfect gases. Specifically, this work was dedicated to flows past a flat plate where the ratio of convective terms to viscous terms tends to infinity ($Re \rightarrow \infty$), i.e. the viscous effects are confined to a thin boundary layer near the solid wall. Numerical calculations of the boundary layer showed that flows with subsonic free stream conditions did not exhibit any pronounced real gas effects, whereas the supersonic case for an accelerated/decelerated dense gas may cause the Mach number to decrease/increase and provoke the displacement body to expand/shrink despite the favourable/adverse pressure gradient. This unexpected behaviour arises from the distribution of the fundamental derivative which is associated with the curvature of the isentropes. In contrast to ideal gases, BZT-fluids may experience values of the fundamental derivative smaller than unity which in turn may lead to the non-monotonous behaviour of the Mach number mentioned above. This significantly affects the boundary layer evolution governed as the continuity equation evaluated at the boundary layer edge predicts that the normal velocity component in an accelerating/decelerating supersonic flow increases/decreases with growing distance to the wall and that this effect becomes more pronounced as the Mach number increases. An other observation resulting from the numerical calculations concerns the density and temperature variations across the boundary layer and along the plate. It was found that the changes in the transverse direction were very small. The same behaviour was observed for the temperature variations in the longitudinal direction whereas the changes in density were of the order unity along the plate. Inspection of the energy equation indeed indicates that the changes in temperature in the whole flow field are of the order Eckert number which for the kind of fluids considered here typically are of order 10^{-2} and so are the changes of density across the boundary layer.

If the free stream conditions of a BZT-fluid are chosen properly, the boundary layer equations exposed to a supersonic flow with adverse pressure gradient may experience a marginal separation singularity, i.e. the wall shear stress vanishes in one single point and immediately recovers. Using asymptotic methods near the point of zero wall shear stress and taking advantage of the specific thermodynamic properties of BZT-fluids regarding density and temperature it was possible to construct an one parameter family of solutions. These describe the transition from completely smooth wall shear distributions to wall shear distributions which terminate in a separation singularity depending on a certain control parameter which

is a measure of the density deviation from the critical value associated with the marginal separation singularity (say, $\Delta k = \rho_{crit} - \rho$). If Δk is smaller than zero we obtain the smooth solution whereas flows with $\Delta k > 0$ terminate in a singularity. In the limit $\Delta k \rightarrow 0^+$ the strength of the singularity becomes arbitrarily small and if the interaction between the boundary layer and the external flow is taken into account one obtains smooth solutions which, depending on the value of Δk , may exhibit a short region of negative wall shear stress. Despite the fact that the marginal separation investigated here is not caused by a specific form of the pressure distribution as in earlier work but rather is triggered by a novel mechanism, i.e. the non-monotonous Mach number distribution associated with a strictly adverse pressure gradient, the interaction equation governing the marginal separation is of classical form. Its numerical solutions yield the wall shear stress distributions which are the mirror images of the classical subsonic case due to other integration limits caused by the supersonic conditions considered here.

References

- [1] ACKERET J. Über Luftkräfte bei sehr großen Geschwindigkeiten insbesondere bei ebenen Strömungen. *Helvetica Physica Acta* 1 (1928), 301–322.
- [2] BATCHELOR G.K. *An introduction to fluid dynamics*. Cambridge University Press, 1970.
- [3] BETHE H.A. The theory of shock waves for an arbitrary equation of state. *Office Sci. Res. & Dev. Rep.* 545 (1942).
- [4] BRAUN S., AND KLUWICK A. Unsteady three-dimensional marginal separation caused by surface mounted obstacles and / or local suction. *under consideration for publication in J. Fluid Mech.*
- [5] BRAUN S., KLUWICK A., AND TRENKER M. Leading edge separation: a comparison between interaction theory and Navier-Stokes computations. *Proc. of the GAMM 02 Conference, Metz, ZAMM* 2 (2002), 312–313.
- [6] CHUNG T.H., AJLAN M., LEE L.L., AND STARLING K.E. Generalized multiparameter correlation for nonpolar and polar fluid transport properties. *Ind. Eng. Chem. Fund.* 27 (1988), 671–679.
- [7] CHUNG T.H., LEE L.L., AND STARLING K.E. Application of kinetic gas theories and multiparameter correlation for prediction of dilute gas viscosity and thermal conductivity. *Ind. Eng. Chem. Fund.* 23 (1984), 8–13.
- [8] CRAMER M.S. Negative nonlinearity in selected fluorocarbons. *Phys. Fluids* 11 (1989), 1894–1897.
- [9] CRAMER M.S. Nonclassical dynamics of classical gases. In *CISM courses and lectures no. 315: Nonlinear waves in real fluids*, Kluwick A., Ed. Springer verlag Wien - New York, 1991, pp. 91–145.
- [10] CRAMER M.S., AND BEST L.M. Steady, isentropic flows of dense gases. *Phys. Fluids A* 3 (1991), 219–226.
- [11] CRAMER M.S., AND CRICKENBERGER A.B. The dissipative structure of shock waves in dense gases. *J. Fluid Mech.* 223 (1991), 325–355.
- [12] CRAMER M.S., AND FRY R.N. Nozzle flows of dense gases. *Phys. Fluids A* 5 (1993), 1246–1259.

- [13] CRAMER M.S., AND PARK S.H. On the suppression of shock-induced separation in Bethe-Zel'dovich-Thompson fluids. *J. Fluid Mech.* 393 (1999), 1–21.
- [14] CRAMER M.S., AND WHITLOCK S.T. Similarity laws in dense gas flows. *ASME paper 03-FE-6* (1993).
- [15] GOLDSTEIN S. On laminar boundary-layer flow near a position of separation. *Quart. J. Mech. Appl. Math.* 1 (1948), 43–69.
- [16] HACKMÜLLER G. *Zwei und dreidimensionale marginale Ablösung von Strömungsgrenzschichten*. PhD, Vienna University of Technology, 1991.
- [17] HARTREE D.R. A solution of laminar boundary-layer equations for retarded flow. *Rep. Memor. Aero. Res. Coun. London No. 2426 (Spec. Vol I)* (1939).
- [18] HOWARTH L. On the solution of the laminar boundary layer equations. *Proc. Roy. Soc. London A* 164 (1938), 547–579.
- [19] KLUWICK A. Transonic nozzle flows of dense gases. *J. Fluid Mech.* 247 (1993), 661–688.
- [20] KLUWICK A. Interacting laminar boundary layers of dense gases. *Acta Mechanica Suppl.* 4 (1994), 335–349.
- [21] KLUWICK A., BRAUN S., AND GITTLER P. Transonic, laminar high Reynolds number flow in slender channels. *Proc. of the IUTAM Symp. Transsonicum IV, Göttingen (in press)*.
- [22] KLUWICK A., KINELL M, AND ZIEHER F. Linearly retarded laminar dense gas boundary layers over a flat plate. *in preparation*.
- [23] LAMBRAKIS K., AND THOMPSON P.A. Existence of real fluids with a negative fundamental derivate γ . *The Physic of Fluids* 15 (1972), 933–935.
- [24] LEES L. Laminar heat transfer over blunt-nosed bodies at hypersonic flight speeds. *J. Fluid Mech.* 247 (1993), 661–688.
- [25] MARTIN J.J., AND HOU Y.C. Development of an equation of state for gases. *AIChE J* 1 (1955), 142–151.
- [26] RIHANI D.N., AND DORAISWANY L.K. Estimation of heat capacity of organic compounds from group distribution. *Ind. Eng. Chem. Fund.* 4 (1965), 17–21.

- [27] RUBAN A.I. A singular solution of the boundary-layer equations which can be extended continuously through the point of zero surface friction. *Izv. Akad. Nauk SSSR: Mekh. Zhidk. Gaza* 6 (1981), 42–52.
- [28] RUBAN A.I. Asymptotic theory of short separation regions on the leading edge of a slender airfoil. *Izv. Akad. Nauk SSSR: Mekh. Zhidk. Gaza* 1 (1982), 42–51.
- [29] STEWARTSON K. Is the singularity at separation removable? *J. Fluid Mech.* 44 (1970), 347–364.
- [30] STEWARTSON K., SMITH F. T., AND KAUPS K. Marginal separation. *Stud. Appl. Math.* 67 (1982), 45–61.
- [31] SYCHEV V.V., RUBAN A.I., SYCHEV VIC.V., AND KOROLEV G.L. *Asymptotic theory of separated flow*. Cambridge University Press, 1998.
- [32] THOMPSON P.A. A fundamental derivate in gasdynamics. *The Physic of Fluids* 14 (1971), 1843–1849.
- [33] THOMPSON P.A., AND LAMBRAKIS K. Negative shock waves. *J. Fluid Mech.* 60 (1973), 187–208.
- [34] ZEL'DOVICH YA.B. On the possibility of rarefraction shock waves. *Zh. Eksp. Teor. Fiz.* 4 (1946), 363–364.
- [35] ZIEHER F. *Kompressible Grenzschichtströmungen bei Zuständen in der Nähe des kritischen Punktes*. Masters Thesis, Vienna University of Technology, 1993.

Appendix A

Thermodynamical properties

	N ₂	FC-71	PP11
molecular weight, \bar{M} [kg/mol]	$28.01 \cdot 10^{-3}$	0.971	0.624
critical temperature, T_c [K]	126.2	646.2	650.2
critical pressure, \tilde{p}_c [MPa]	3.390	0.9423	1.460
critical spec. volume, \tilde{v}_c [m ³ /kg]	$3.206 \cdot 10^{-3}$	$1.615 \cdot 10^{-3}$	$1.594 \cdot 10^{-3}$
boiling temperature, \tilde{T}_b , [K]	77.4	526.2	488.2
n	0.0	0.4273	0.5776
acentric factor, ω	0.039	0.97	0.78
dipolmoment, μ_r	0.0	0.0	0.0
idealgas isochoric heat capacity evaluated at the critical point $\tilde{c}_{v\infty}^c$, [J/kg K]	768.41	1241.6	1296.1

Table 5: Input parameters for shear viscosity, thermal conductivity and pressure.

Appendix B

Predictions for shear viscosity and thermal conductivity

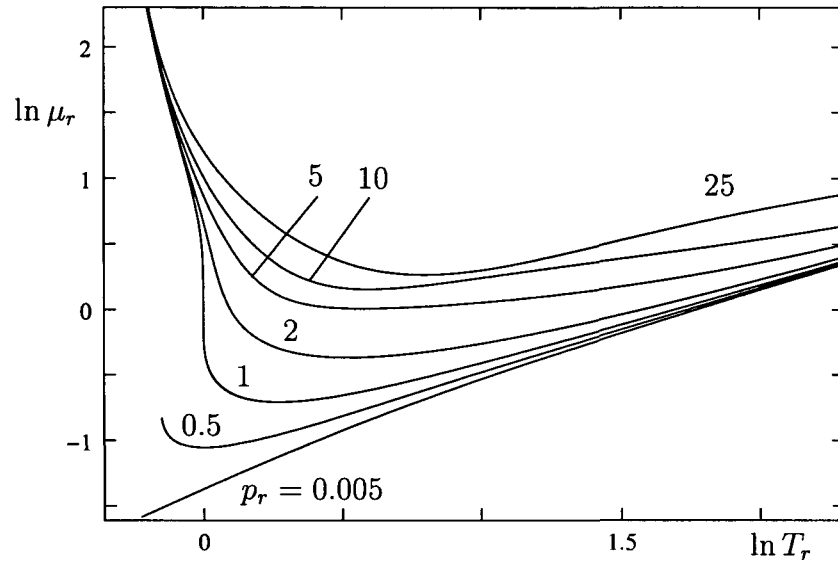


Figure 105: Predictions of the shear viscosity for FC-71 using the method from Chung et al. All quantities are non-dimensionalized with their values at the thermodynamic critical point.

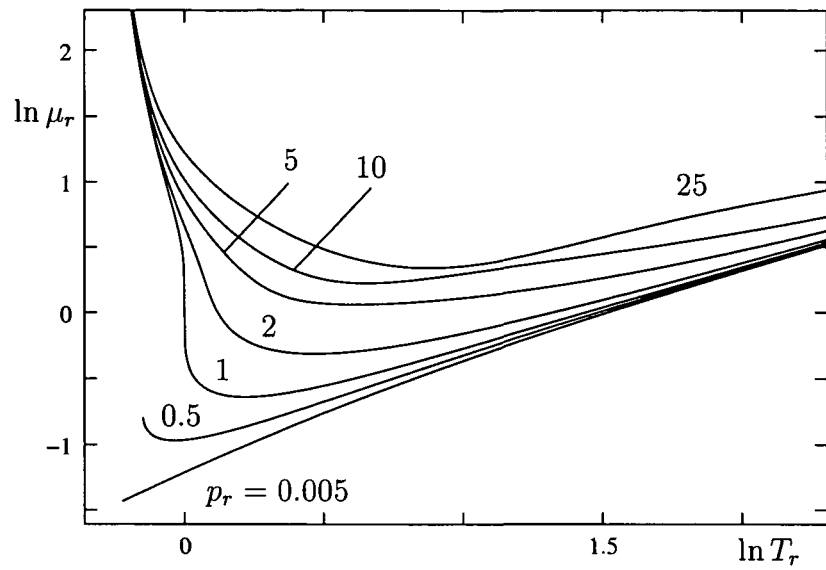


Figure 106: Predictions of the shear viscosity for PP11 using the method from Chung et al. All quantities are non-dimensionalized with their values at the thermodynamic critical point.

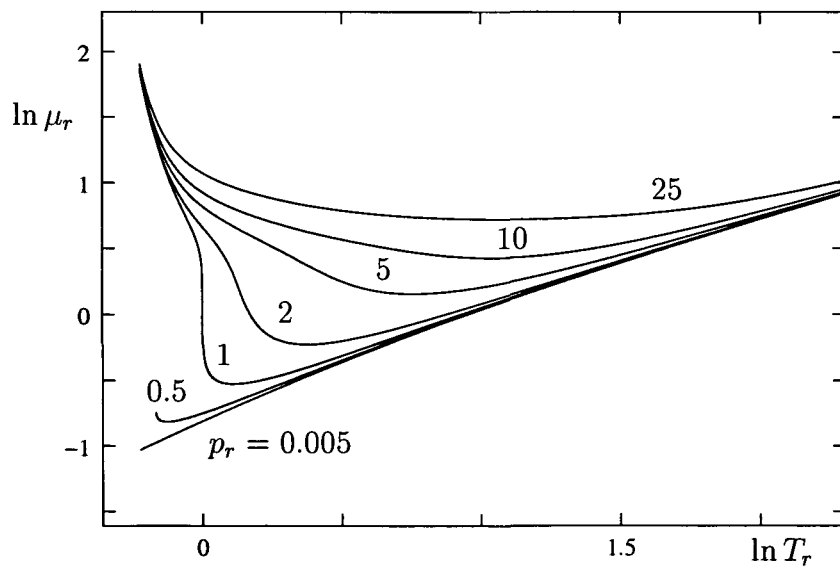


Figure 107: Predictions of the shear viscosity for N₂ using the method from Chung et al. All quantities are non-dimensionalized with their values at the thermodynamic critical point.

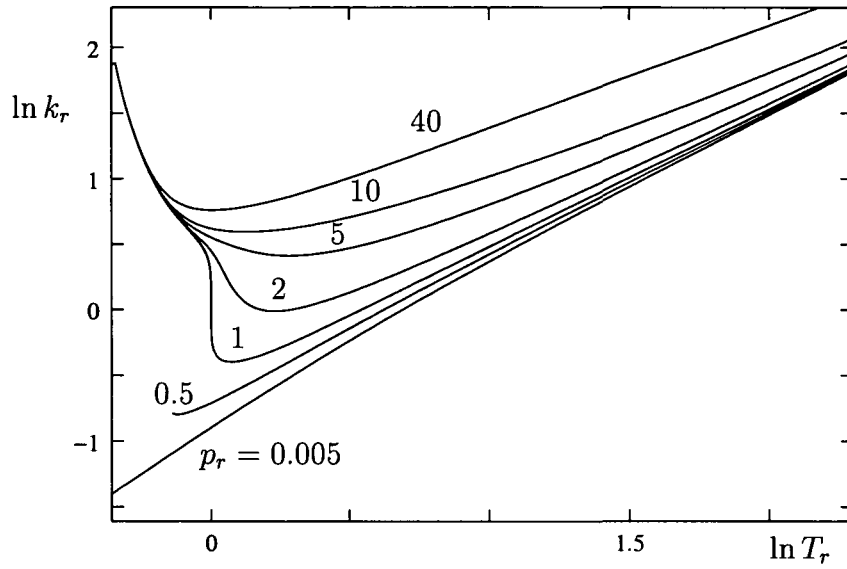


Figure 108: Predictions of the thermal conductivity for FC-71 using the method from Chung et al. All quantities are non-dimensionalized with their values at the thermodynamic critical point.

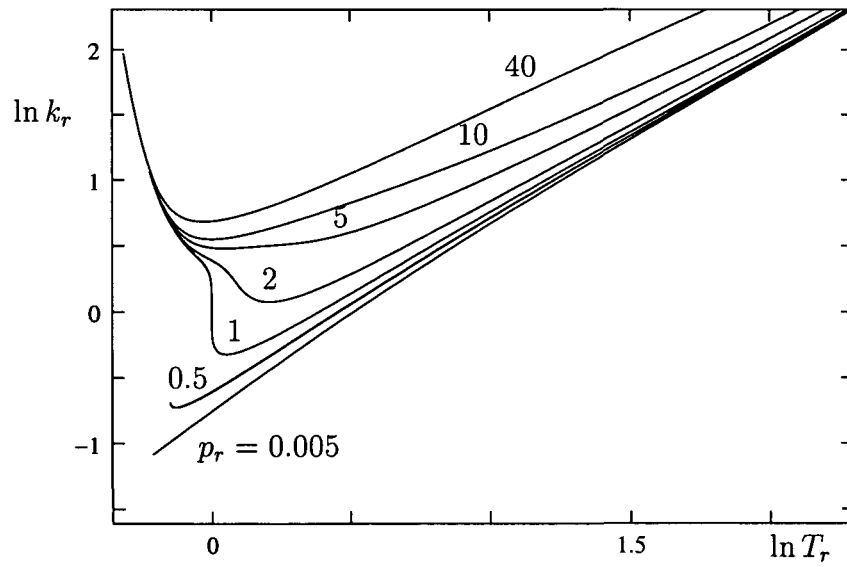


Figure 109: Predictions of the thermal conductivity for PP11 using the method from Chung et al. All quantities are non-dimensionalized with their values at the thermodynamic critical point.

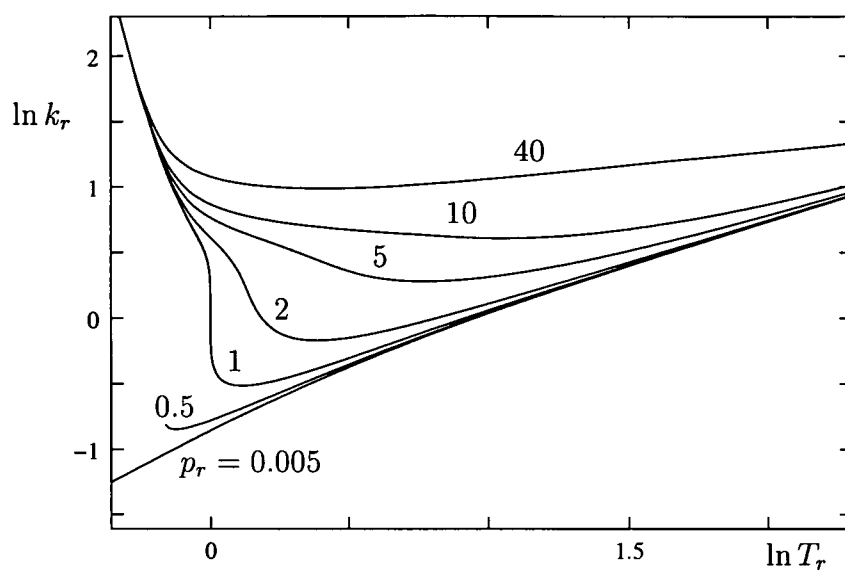


Figure 110: Predictions of the thermal conductivity for N_2 using the method from Chung et al. All quantities are non-dimensionalized with their values at the thermodynamic critical point.

Lebenslauf

Mats KINELL

Persönliche Daten

Geboren 06.04.1973 in Karlskoga, Schweden

Ausbildung

1980 - 1989 Grundschule
Sandviksskolan, Österleden

1989 - 1992 Gymnasium
Bergslagsskolan

1995 - 2000 Studium Maschinenbau
Luleå University of Technology

1992 - 1995 Präsenzdienst
KA1 Waxholm

2000 - 2003 Wissenschaftlicher Mitarbeiter
Institut für Strömungslehre und Wärmeübertragung
Technische Universität Wien